# QUADRATIC COUPLING BETWEEN A CLASSICAL NANOMECHANICAL OSCILLATOR AND A SINGLE SPIN

by

**Shonali Dhingra**

BSc, Delhi University, 2006

MSc, Delhi University, 2008

Submitted to the Graduate Faculty of

the Kenneth P. Dietrich School of Arts and Sciences in partial fulfillment

of the requirements for the degree of

**Doctor of Philosophy**

University of Pittsburgh

2015

UNIVERSITY OF PITTSBURGH

DIETRICH SCHOOL OF ARTS AND SCIENCES

DEPARTMENT OF PHYSICS AND ASTRONOMY

This dissertation was presented

by

Shonali Dhingra

It was defended on

April 13, 2015

and approved by

Brian D'Urso, Ph.D. (Condensed Matter Physics - Experiment)

Gurudev Dutt, Ph.D. (Condensed Matter Physics - Experiment)

Andrew Daley, Ph.D. (Condensed Matter Physics - Theory)

Adam Leibovich, Ph.D. (Particle Physics)

Daniel Cole, Ph.D. (Engineering)

Dissertation Director: Brian D'Urso, Ph.D. (Condensed Matter Physics - Experiment)

**QUADRATIC COUPLING BETWEEN A CLASSICAL NANOMECHANICAL OSCILLATOR AND A SINGLE SPIN**

Shonali Dhingra, PhD

University of Pittsburgh, 2015

Though the motions of macroscopic objects must ultimately be governed by quantum mechanics, the distinctive features of quantum mechanics can be hidden or washed out by thermal excitations and coupling to the environment. For the work of this thesis, we tried to develop a hybrid system consisting a classical and a quantum component, which can be used to probe the quantum nature of both these components. This hybrid system quadratically coupled a nanomechanical oscillator (NMO) with a single spin in presence of a uniform external magnetic field.

The NMO was fabricated out of single-layer graphene, grown using Chemical Vapor Deposition (CVD) and patterned using various lithography and etching techniques. The NMO was driven electrically and detected optically. The NMO's resonant frequencies, and their stabilities were studied.

The spin originated from a nitrogen vacancy (NV) center in a diamond nanocrystal which is positioned on the NMO. In presence of an external magnetic field, we show that the NV centers are excellent $\theta^2$ sensors. Their sensitivity is shown to increase much faster than linearly with the external magnetic field and diverges as the external field approaches an internally-defined limit.

Both these components of the hybrid system get coupled by physical placement of NV-containing diamond nanocrystals on top of NMO undergoing torsional mode of oscillation, in presence of an external magnetic field. The capability of the NV centers to detect the quadratic behavior of the oscillation angle of the NMO with excellent sensitivity, ensures

quantum non-demolition (QND) measurement of both components of the hybrid system. This enables a bridge between the quantum and classical worlds for a simple readout of the NV center spin and observation of the discrete states of the NMO. This system could become the building block for a wide range of quantum nanomechanical devices.

## TABLE OF CONTENTS

## LIST OF TABLES

## LIST OF FIGURES

## PREFACE

This is 'My Story' and my 'Acknowledgments'. These two pages of the thesis were the first ones I wrote; in an uncanny way, this section was the easiest one to write, while being the one that mattered the most.

I was born and brought-up in New Delhi, India. I did my undergrad (B.Sc.) and masters (M.Sc.) in Physics from one of the most-prestigious colleges for sciences in India, St. Stephens College, Delhi University. I came to the US with quite a solid idea of what I wanted to do for a thesis project, at least I thought so - I just didn't know how to do it, or even where to start. But as is almost always the case, I did not end up doing what I thought I would. I actually did something that I enjoyed and learned from much more than I could have hoped for.

The protagonist of 'My Story' is of course me, but my adviser, Dr. Brian D'Urso, is a very close second. So, it should not be a surprise that the first person I'd like to thank in the 'Acknowledgments' section here is Dr. D'Urso. I have always given a lot of importance to my teachers - I can remember at least one teacher standing at every important milestone of my life. And at this most important milestone so far, getting a Ph.D., that teacher is Dr. D'Urso. I thought I knew a lot about 'Research' when I joined the graduate program at Pitt - I soon realized that wasn't quite true. And from there, almost all that I have learned about it has been from Dr. D'Urso. His unfaltering perseverance in attempting to find different ways to solve problems and in coming up with unending 'Crazy Ideas' - have been the beacons of this winding Ph.D. road for me. I can foresee myself always referring back to these years and thinking - 'How would have Dr. D'Urso dealt with this problem?'. I can only hope some of his 'research-wisdom' has rubbed off on me, which I'm sure will be one of my greatest strengths for whatever endeavors I take up in life. And alongside being a

great adviser, he has been a good friend, with whom I've talked about gardening and mental depression and almost everything in between. We've drank quite a few bottles of beer and wine, and eaten a lot of cookies and cakes, together. I have yelled at him, argued with him and even cried in front of him. He has been the largest constant of these past 7 years of my Ph.D.

These years in grad school have been one phase of life, but there was life before it and there will be life after it. Irrespective of what I went through during this phase, before it or will go through after it, the biggest constant of my life was/is/will be the presence of my family - My parents, husband and brother. I would like to thank them for everything - for even just being there - and share with them the credit for any and every achievement of my life.

I would also like to take a few lines here to thank a buncha people who made this Ph.D. phase of my life a bit livelier (or at times, even livable). Hands-down, the first one here has to be Nandy - my arch-enemy from undergrad, my beer-buddy during my grad years, and (hopefully) a friend for life. The next in-line is Xie Li - the count of the number of ice-cream scoops and pizza slices I have eaten with her would surely catch-up with the number of days in these 7 years! I would also like to thank my lab mates, Elliot Jenner and Jen-Feng Hsu, for absorbing all my causticity and not burping it back out. And even though this might not be conventional, I would like to thank few of the administrative staff members in the Physics department, who made survival in grad school a bit easier, such as Laura, Jim, Michele, Bob, Tom, Ken, Josh, Greg, Lori, Cindy Cercone and all the others who were working back-stage. And well, special mention of Leyla is needed, who actually made life easier in a way that it seemed to be getting harder (lol)!!

And now for this last paragraph I would like to let everyone know that the work done for any graduate thesis does not happen in the orderly manner in which it is presented in the thesis. And this thesis is no different. This was the second largest constant of these past 7 years - the seemingly Brownian motion of research - except that it was not quite Brownian, but rather 'Frog in a well' motion. And at all points fingers were kept crossed to hope that it doesn't become its retrograde version. And the fact that I was able to write this thesis proves that it didn't. QED (except that it wasn't).

# 1.0 INTRODUCTION

*"Anyone who is not shocked by quantum theory has not understood it"* - Neils Bohr

All physicists, at one point or another, believe that they understand Quantum Physics, with all its nuances. This belief might not serve any purpose other than refueling their own egos. This thesis is a small step for the author, using the same means, to the same end!

## 1.1 CLASSICAL AND QUANTUM WORLDS

Until the mid-19th century, the quantum world eluded scientists, and classical theories ruled the roost. As our knowledge of phenomena on the microscopic scale became more precise, classical theories ran into more and more difficulties and contradictions. By the early 20th century, due to the results of various experiments, scientists started questioning the universality of the classical theories. This led to the conclusion that classical theories are an approximation, used to describe macroscopic objects, of a more accurate quantum theory. Scientists started believing the physical world at the microscopic level cannot be described by classical physics, and quantum theories ought to replace the existing classical ones [1, 2].

Another way to state the same belief is that the classical and quantum worlds coexist; that they are the two sides of the same coin. The reign of one might diminish the prevailment of the other, but to understand any phenomenon or system, one has to take into consideration both these sides. A small proof of this thought-philosophy was what directed this thesis. One goal of this thesis was to use a classical oscillator, such as a nanomechanical oscillator (NMO), and show quantum attributes in it.

A thing to be noted is that systems such as NMOs cannot technically be considered truly microscopic, as they may be made up of 100,000 to billions of atoms, but they cannot be considered macroscopic either, as they might not always obey classical physics. Systems at this scale are considered mesoscopic [3, 4].

## 1.2 NANOMECHANICAL OSCILLATORS (NMO)

Mechanical systems have been at the forefront of quantum studies, since the inception of quantum theories [5, 6].

A classical one-dimensional mechanical oscillator is a particle constrained to move long an axis and subject to a restoring force proportional to a point located on that axis [1]. By the law of conservation of energy, the equations of motion of such a particle, with mass $m$, can be derived using the Hamiltonian $(p^2 + m^2\omega^2 q^2)/2m$, with $p$ as its momentum, $q$ as its position coordinate and $\omega$ as its angular frequency. These equations of motion are found to oscillatory, thus naming such a particle - Harmonic Oscillator. We see myriad examples of such a particle at the macroscopic scale in our day-to-day life, such as a simple pendulum and a mass on a spring.

Irrespective of the scale of the system, or whether classical or quantum laws are applicable to it, the laws of conservation of momentum and energy remain rigorously verified [1]. Thus, an NMO, which is a mechanical oscillator at the nano-scale, also has the same Hamiltonian as described for the classical particle above. Using the laws of quantum mechanics, as is appropriate for such an NMO, we can see that this quantum mechanical system has quantized energy levels given by $H = \hbar\omega\left(\hat{n} + \frac{1}{2}\right)$, where $\hat{n} = 0, 1, 2, \ldots, \infty$.

An NMO is a part of a much bigger class of electrical and mechanical systems at the micro and nano-scale: microelectromechanical and nanoelectromechanical system (MEMS and NEMS). Broadly speaking, MEMS and NEMS include all machines, sensors, computers and electronics that are on the micro/nanoscale [3]. Irrespective of scale, all electromechanical systems comprise of a mechanical element and a transducer.

The mechanical element is usually an element that responds to tiny forces or perturbations, by either deflecting or oscillating. The transducer in these systems converts mechanical energy from the mechanical element into electrical or optical signal or vice versa. However, in some systems, there might not be any conversion of energy and the signal from the system might simply be the readout of the characteristics of the mechanical element [3]. This latter subset of NEMS are termed NMOs, in specific.

Some properties of the NMO systems which render them useful for various applications

and measurements in the quantum world include their small size, mass, moment of inertia and spring constant. Such properties ensure the NMOs have a high fundamental frequency of oscillation ($\omega$), making them useful for microwave applications. Their small size limits their interaction with their environment, thus making them have high quality factors (Q-factor). Such properties make these oscillators very sensitive to small changes in mass, pressure, temperature and other such changes in their environment. Due to these advantages, the NMOs have been extensively researched to be used as a force sensor to measure static and time-varying forces of small amplitudes [3, 7, 8]. They have also been used as mass sensors with very high resolution [9, 10].

Such NEMS/NMO devices have not only been used in a wide range of sensing applications, but they have also been getting used for characterizing quantum properties of a mechanical oscillator [5]. A lot of effort is being put into trying to cool down the NMOs to their quantum ground state, to enable further quantum control. The inherent challenge for all such efforts is, as a first step, to decrease the temperature ($T$) of the mechanical oscillator so that $T < (\hbar\omega)/k_B$, where $\omega$ is its oscillation frequency. One such successful effort was conventional environmental cooling of oscillators with mechanical oscillation mode near 6 GHz to temperatures below $\sim$ 100 mK [11]. But such low temperatures are hard to attain and use for practical applications, thus enabling the search for other methods for the same purpose. Use of radiation pressure forces was proposed as one such method [12] and variants of the same have been successfully demonstrated as viable methods, such as laser cooling [13] and sideband cooling [14]. Some such methods achieved this feat at temperatures as high as 20 K [13].

A few examples of NEMS/NMO devices used for applications and characterizations, out of thousands of such devices fabricated and used around-the world, are shown below.

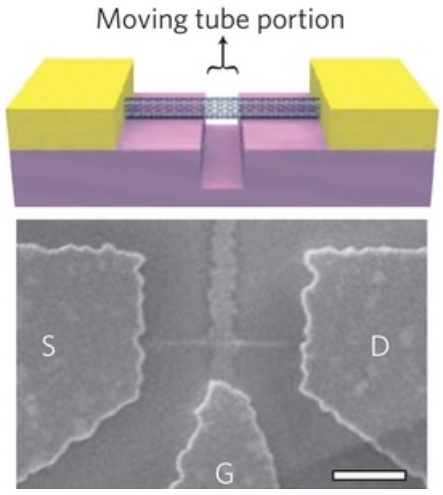


(a)

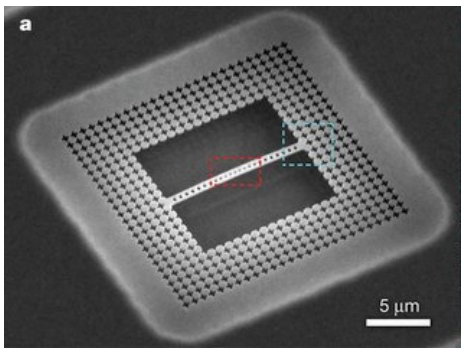


(b)

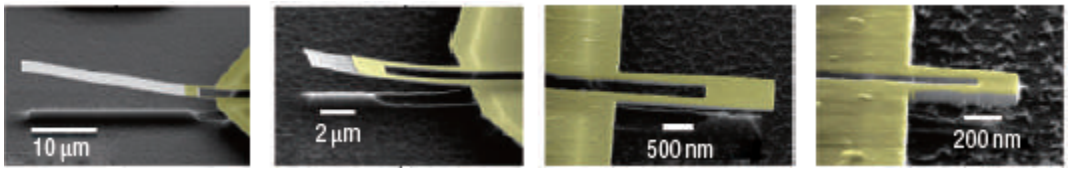


(c)

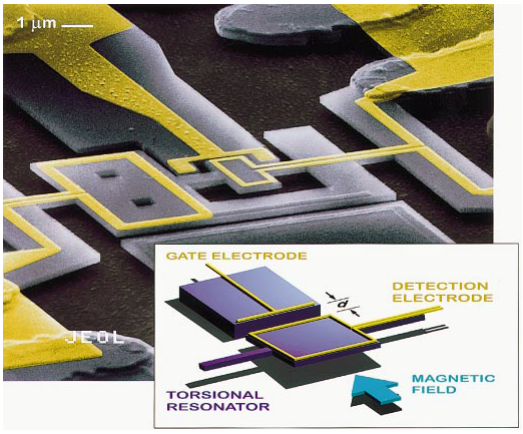


(d)

Figure 1: Examples of NEMS/NMO devices fabricated and used for various applications (a)Schematic and SEM image of a carbon nanotube device used for mass-sensing with yoctogram resolution (scale bar, 300 nm) [10], (b)Silicon nanobeam device shown here was successfully cooled down into its quantum ground state using laser cooling [14], (c)SEM image of silicon carbide (SiC) nanocantilevers of various different sizes which were used as nanoscale force and mass sensors for very high-frequency applications [15] and (d)An electron micrograph and a schematic of a torsional mechanical resonator used as a charge detector [16].

## 1.3 HYBRID SYSTEMS

One of the biggest challenge in the world of NEMS/NMO is to find a reliable technique to readout the state of the oscillator. This technique should be compatible with the quantum properties of the NMO and should not disturb/hinder these properties in any way. For this purpose, quantum hybrid systems are proposed and fabricated, which combine the mechanical oscillator with another quantum system. This system can be used in conjunction with the NMO to aid in its actuation, readout, characterization or implementation of an application. In general, the term hybrid can be used to describe a system that couples one or more elements from different fields such solid-state physics, atomic, molecular and optical (AMO) physics, electronics etc [17, 5]. The development and advancements of these hybrid systems has thus become an interdisciplinary field.

Following are some examples of hybrid systems, where another element has been coupled with a mechanical element, that have been successfully realized around the world. The applications and/or advantages of these systems are also mentioned [18, 5]. The devices used in these examples are shown in Fig. 2 below.

- One of the first hybrid mechanical system was a silicon (Si) cantilever with a magnetic tip coupled to a quantum spin system. The mechanical system was thus used to detect the presence of a single electron spin [8].
- A micromechanical bulk dilatational resonator was coupled with a superconducting quantum bit (qubit) at dilution refrigerator temperatures. This system was used to demonstrate that the resonator had been cooled down to its quantum ground state [11].
- A SiC nanowire (the NMO) was successfully coupled to a single spin quantum-system - nitrogen vacancy (NV) center in diamond (explained in general in Section 1.4 and in detail in Chapter 2), in presence of a strong magnetic field gradient. Such a system has the potential of highlighting quantum behavior of the mechanical system at higher temperatures with extended coherence times [19].
- A hybrid optomechanical system was realized by coupling ultracold atoms to a micromechanical membrane. Such systems show that atoms, similar to qubits, could be used for sympathetic cooling of the NMO to its quantum ground state [20].

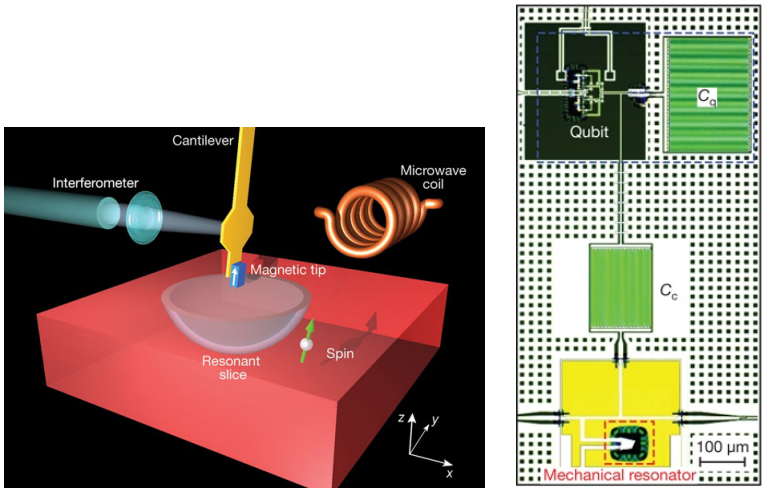


(a) (b)

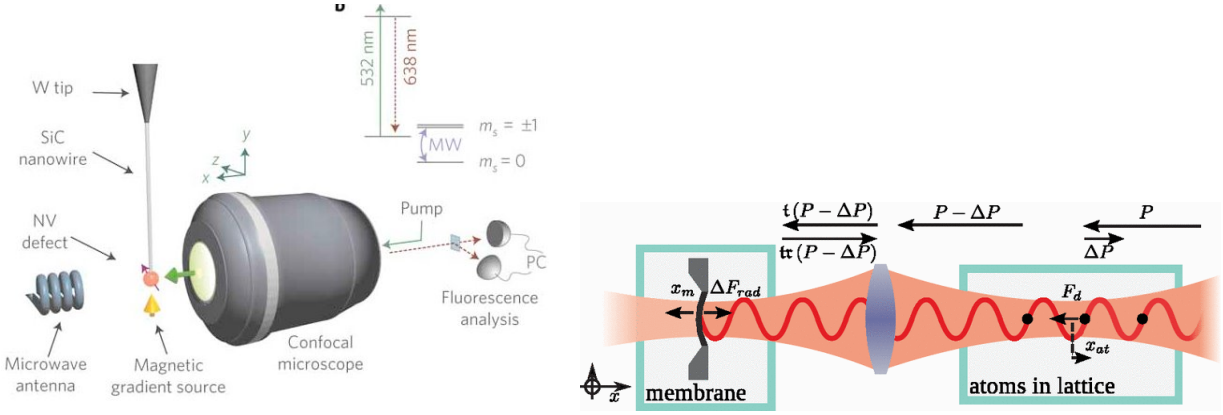


(c) (d)

Figure 2: A few examples of hybrid mechanical systems (a)Schematic of a Si cantilever hybrid system used to detect the presence of a single electron spin [8], (b)A high-frequency mechanical resonator was coupled to a superconducting qubit at temperatures below ∼100 mK to readout the resonator's quantum ground state [11], (c)A nanowire as NMO was successfully coupled with a single-spin quantum system, the NV center. Such a system has the potential of exhibiting quantum behavior in the NMO at high temperatures with extended coherence times [19] and (d)Ultracold atoms coupled to an NMO, as in this hybrid system, could be used to cool the NMO down to its quantum ground state [20].

I will now describe quantum spin systems in detail, specifically, NV centers, as we employ

them, alongside an NMO, to build a hybrid system, described in Section 1.5

## 1.4 SPIN SYSTEMS

Quantum mechanical systems, such as optical photon, atomic systems, charged ions and solid-state spin systems, are getting a lot of attention lately due to their potential use in applications involving quantum information, such as Quantum Computation, Quantum Cryptography, Quantum Teleportation etc [21]. A quantum system, such as needed for the above applications, should have two accessible states, like a classical system, but should be able to exist in any superposition of those two states for a long time [22], unlike a classical system. Such a quantum system has come to be known as a qubit (quantum bit), in opposition to a bit (classical systems used for classical computing). Due to the inherent nature of quantum systems, this puts opposing constraints on qubits - "A quantum computer has to be well isolated in order to retain its quantum properties, but at the same time its qubits have to be accessible so that the can be manipulated to perform a computation and to read out the results" [23].

A spin system is a particle (such as an electron or photon), or an ensemble of particles (such as the nucleus of an atom or a charged ion), which have quantized spin states, either integer or half-integer. Out of all the quantum systems available for applications involving quantum information, solid-state spin systems allow maximum number of quantum operations (ratio of decoherence time to operation times) [23], and simplest fabrication and characterization experiments [24]. Due to such advantages, quantum spin systems are being extensively used as a component of hybrid systems, as mentioned in Section 1.3.

### 1.4.1 Nitrogen Vacancy center

One such spin system being characterized and used a lot lately is a naturally occurring defect in diamonds, the nitrogen-vacancy (NV) center, which can also be artificially created in diamond by irridiation and annealing [25]. It consists of a substitutional nitrogen atom with

an adjacent carbon vacancy [26]. The electronic ground state of this defect has been studied extensively and has been shown to form a spin triplet (S=1) state [27, 25], with remarkably long spin depolarization ($T_1 \sim 4$ s at 4 K) [28] and decoherence times ($T_2 \sim 2$ ms at 300 K) [29]. Further, the defect state can be optically spin-polarized and measured by combining confocal microscopy techniques with spin-state dependent optical fluorescence [30, 25]. The ground state exhibits a zero-field splitting of 2.87 GHz (2.88 GHz at low temperatures) which defines the $\hat{z}$ axis of the electron spin. An additional magnetic field can be applied to split the $m_s = \pm 1$ sublevels, which allows for fast coherently driven spin transitions using microwave fields [31, 32]. Experiments have shown that the electron spin of the NV center is an excellent sensor of the local magnetic environment, with the ability to measure and even manipulate proximal nuclear spins [33, 34, 35]. This sensitivity was used recently to demonstrate nanoscale magnetic sensing and magnetic imaging with NV centers [36, 37].

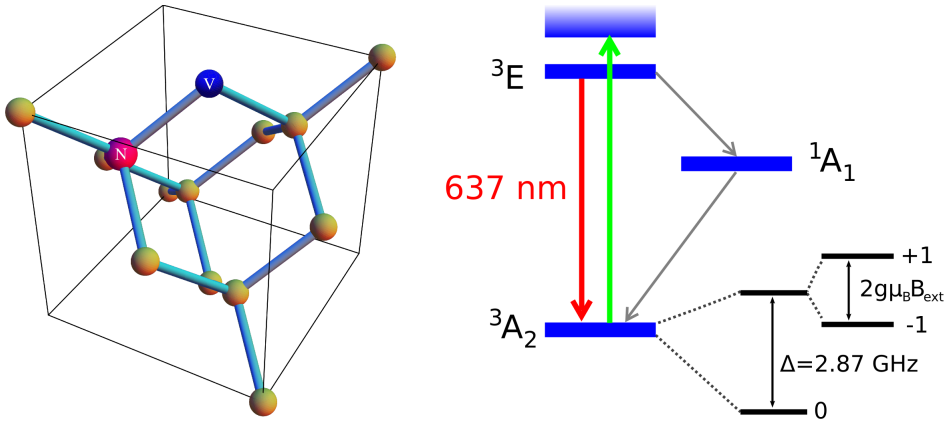


Figure 3: Schematic of an NV center in a diamond crystal, and its electronic ground state energy levels.

## 1.5 OUR HYBRID SYSTEM

The work done for this thesis was motivated by the fabrication and characterization of a hybrid system consisting of two parts: an NMO, which is a classical harmonic oscillator, and a quantum spin system. Our NMO was fabricated using a thin film, in the form of a

doubly-clamped beam. The other part of the hybrid system was NV centers. To achieve the hybrid system, nanodiamonds, with naturally containing NV centers, were physically placed on the NMO, which was driven in a way to excite its torsional modes. The coupling between the two components occurred in presence of an external magnetic field. A schematic of our hybrid system is shown in Fig. 4.

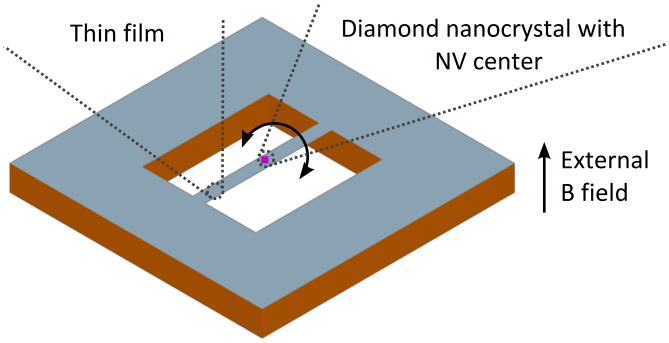


Figure 4: A schematic of our hybrid system - a doubly clamped NMO coupled to a quantum system, in presence of an external magnetic field. This can be used to make a QND measurement of both components, using the other as the probe.

We tried to achieve the following objectives using this hybrid system, for the purpose of this thesis:

- We proposed to be able to observe quantum behavior in the classical NMO by coupling it to a quantum system.
- The coupling between these two systems gives us the capability of making quantum non-demolition (QND) measurement [38, 7] of both the systems. As will be seen in Chapter 2, the interaction Hamiltonian between the NMO and the NV center commutes with the Hamiltonian of each system separately. This ensures that the measurement in both directions, i.e. using NMO as the probe to measure the state of the NV, and vice versa, is QND. This lets us make repeated time measurements of the system in a way that one such measurement does not alter the result of the next one.
- Coupling between an electronic spin system and an NMO have been proposed and used before, but with either a complex measurement scheme [39], or with very weak cou-

pling [8]. Our system, on the other hand, works with a very simple measurement scheme and could potentially lead to very strong coupling between the two systems.

- To observe the quantum behavior of the NMO using this hybrid system, we did not intend to cool it down to its quantum ground state. Instead, using the spin system as the probe, we should have been able to monitor quantized energy jumps in the NMO, which is its quantum signature.
- On the other hand, using the NMO as the probe, we should have been able to readout the NV center spin state. Usually optical techniques are used to readout the spin state of an NV center, which could prove to be a difficult task due to weak emission of individual centers, thus inciting research to circumvent this problem [40, 41].

A layout of the thesis, outlining the placement of chapters with details on each of the part of the hybrid system mentioned above, is given in Section 1.6.

## 1.6 THESIS OVERVIEW

As described in the above sections, all the work for this thesis largely deals with the fabrication and characterization of our hybrid system.

**Chapter 1** here gives a brief introduction to the difference between classical and quantum phenomena, from the perspective of a mechanical system. I then give an overview of the concept and previous work done in the field nanomechanical oscillator (NMO), spin systems, such as nitrogen-vacancy (NV) center, and hybrid systems where one of the coupled system is an NMO. I also introduce the hybrid system developed in our lab, which couples an NMO and an NV center.

**Chapter 2** theoretically analyzes our hybrid system, and theoretically describes the interaction between the two components of this system. The work presented in this chapter, alongside some descriptions included in Chapter 1, was published in [42].

**Chapter 3** describes in detail the fabrication of the thin film(s) used for the NMO component of the hybrid system. This chapter includes the work presented in [43]. The

work presented in this chapter was also used for collaborative research presented in [44, 45, 46, 47, 48].

**Chapter 4** describes the various steps undertaken and processes used to fabricate the hybrid system (devices) from the thin films. One section of this chapter will be presented in a future publication [49].

**Chapter 5** gives details of the home-designed and home-built cryostat used to house the devices during their characterization.

**Chapter 6** describes the techniques, methodology and instruments used to drive and detect the NMO motion, and to excite and detect the NV centers.

In **Chapter 7**, I describe the various detected characteristics of the NMO. This chapter also describes the issues faced with the same, because of which the probing of the NMO to readout the NV centers was unsuccessful.

**Chapter 8** describes our efforts in using NV centers as the probe to readout the NMO's quantum characteristics. The work done in this chapter experimentally verified that the NV centers follow the theory presented in Chapter 2, and are capable of being great sensors for QND measurements. The work done for this chapter will be presented in a future publication [50].

At last, **Chapter 9** summarizes the work done for this thesis, gives plausible applications of this work, and outlines the opportunities of further research needed/possible with regards to this thesis project.

The appendices at the end are used to supply more experimental details of the work directly or indirectly related to this thesis.

# 2.0 THEORY

We have two parts to our hybrid system as mentioned in section 1.5: the NanoMechanical Oscillator and the Nitrogen Vacancy centers. We studied the expected theoretical behavior of our hybrid system [42], before venturing into its experimental realization.

## 2.1 NMO

We use the standard harmonic oscillator Hamiltonian for the NMO contribution:

$$H_{NMO} = \hbar\omega_m \left(\hat{n} + \frac{1}{2}\right). \tag{2.1}$$

The frequency $\omega_m$ is the classical oscillation frequency, which can be calculated from the dispersion relation of torsional waves on a graphene ribbon [51], giving

$$\omega_m = \frac{\pi}{L}\sqrt{\frac{2Yt^3}{3\rho w^2(1+\nu)}}, \tag{2.2}$$

where $\nu$ is the Poisson ratio, $Y$ is the Young's modulus, $L$ is the length, $w$ is the width, $t$ is the thickness, and $\rho$ is the mass density of the NMO ribbon material.

For the same geometry, the frequency of the bending mode is given by [51]:

$$\omega_b = \left(\frac{\pi^2}{L^2} + \frac{\pi^2}{w^2}\right)\sqrt{\frac{Yt^3}{12\rho(1-\nu^2)}}. \tag{2.3}$$

Using the above equations 2.2 and 2.3 we can estimate the resonant oscillation frequency of nano-mechanical oscillators made out of different thin film materials such as aluminum oxide and graphene. The table below summarizes the expected resonant frequencies of NMOs of specific dimensions made of these two thin films, in bending and torsional modes.

| Film | Auminum Oxide | | Graphene | |
|---|---|---|---|---|
| Length | 2 $\mu$m | | | |
| Width | 1 $\mu$m | | | |
| Thickness | 4 nm | | 0.88 Å | |
| Mode | Torsional | Bending | Torsional | Bending |
| Resonant Frequency (MHz) | 7.3 | 22.8 | 0.36 | 1.08 |

Table 1: Comparison of expected resonant frequencies of torsional and bending modes of bridge devices fabricated using aluminum oxide and graphene

For the above theoretical estimates of the resonant frequencies of the graphene bridges, physical and elastic parameters used are as mentioned in [51]. For aluminum oxide bridges, these parameters are mentioned in http://accuratus.com/alumox.html, for 99.5% pure films. Experimentally detected resonant frequencies are usually a mix of the above-mentioned torsional and bending modes, maybe even including other such modes.

## 2.2 NITROGEN VACANCY (NV) CENTERS

We use the usual Hamiltonian for the NV center (for convenience, we analyze the system assuming the NV center $\hat{z}$ axis is perpendicular to the substrate when the NMO is not twisted) [30, 52]:

$$H_{NV} = \hbar\Delta S_z^2 + g\mu_B \left(\vec{S} \cdot \vec{B}_{ext}\right), \tag{2.4}$$

where $\Delta$ is the zero-field splitting which defines the $\hat{z}$ axis of the NV, $g \approx 2$ is the electron g-factor in the NV center, $\mu_B$ is the Bohr magneton, and $\vec{S}$ is the electronic spin of the NV center. $\vec{B}_{ext}$ is the external magnetic field which results in coupling between the NMO and NV center.

## 2.3 OUR HYBRID SYSTEM

To understand our Hybrid System we started by trying to write the quantum mechanical Hamiltonian for the system, with terms for the nanomechanical oscillator and NV center added together:

$$H = H_{NMO} + H_{NV}. \tag{2.5}$$

Although the applied magnetic field remains fixed in a certain direction, $\vec{S} \cdot \vec{B}_{ext}$ in Eq. 2.4 depends on the NMO angle $\theta$ since the angle of the NV $\hat{z}$ axis relative to $\vec{B}_{ext}$ depends on $\theta$. For an external field which is in the $\hat{z}$ direction when $\theta = 0$, we have

$$H_{NV} = \hbar\Delta S_z^2 + g\mu_B B_{ext} \left(S_y \sin\theta + S_z \cos\theta\right). \tag{2.6}$$

We defined $B_{zfs} = \hbar\Delta/g\mu_B \sim 0.1025$ T as the magnitude of the effective internal magnetic field which results in the zero field splitting $\Delta$, and analyzed the NMO-NV interaction by finding the eigenvalues of $H_{NV}$ with $\theta$ as a parameter. For small NMO oscillation angle $\theta$, we can expand the eigenvalues as:

$$\lambda_i(\theta) = \hbar\omega_i + \frac{1}{2}\kappa_i\theta^2 + O(\theta^4), \tag{2.7}$$

where $i = -1$, 0, or $+1$ is a label which is equivalent to the NV center $m_s$ when $\theta = 0$.

Some results of these calculations are shown in the figure below:

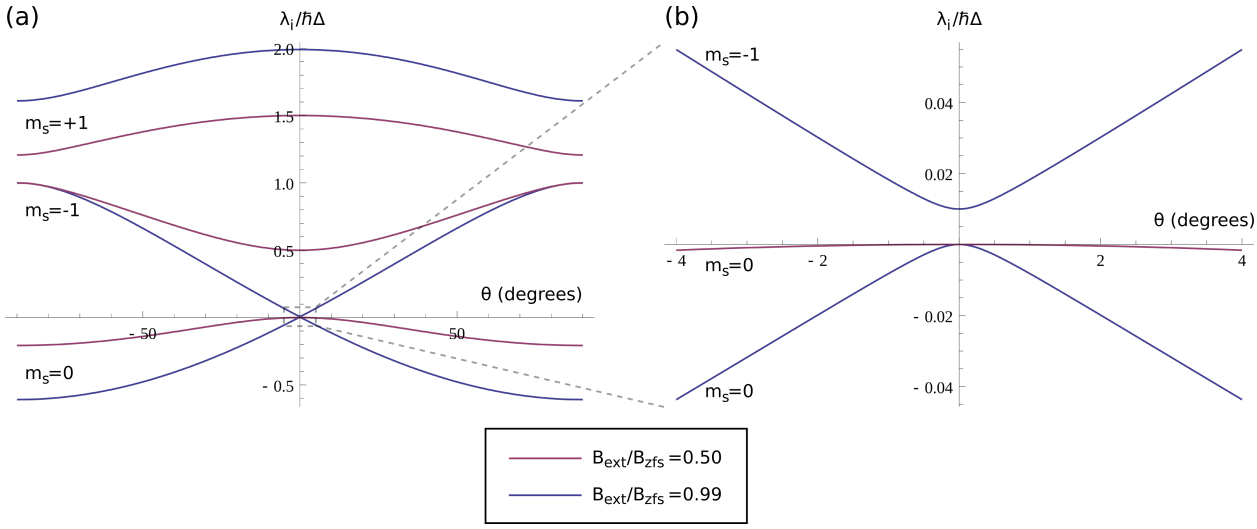


Figure 5: Plots of variation in spin state energies with NMO angle $\theta$ with two different external field magnitudes (a) Variation over full range of angles and (b) Smaller range near $\theta = 0$ showing $\theta^2$ dependence of energy gap.

We further analyze the sharp nonlinear dependence of the energy gap between the $|0\rangle$ and $|-1\rangle$ spin states around $\theta = 0$, which is the result of an avoided level crossing between these states when $B_{ext}$ approaches $B_{zfs}$. For QND measurements, we seek a large $\theta^2$ dependence of the energy eigenvalues.

In the $\theta$-independent term in $\lambda_i(\theta)$, $\omega_i$ is simply the result of combining the zero field splitting with the static external field at $\theta = 0$:

$$\omega_{\pm 1} = \Delta \left(1 \pm B_{ext}/B_{zfs}\right), \tag{2.8}$$

$$\omega_0 = 0. \tag{2.9}$$

The $\theta^2$ coefficient in $\lambda_i(\theta)$, $\kappa_i$, is an NV-state-dependent effective spring constant associated with the NMO-NV interaction, leading to state-dependent frequency shift in the NMO oscillation frequency. For the three NV spin states we consider, $\kappa_i$ is:

$$\kappa_{\pm 1} = -\hbar\Delta \frac{B_{ext}}{B_{ext} \pm B_{zfs}}, \tag{2.10}$$

$$\kappa_0 = \hbar\Delta \frac{2B_{ext}^2}{B_{ext}^2 - B_{zfs}^2}. \tag{2.11}$$

Treating the NMO, which actually has a distributed moment of inertia and torsional spring constant, as a localized torsion pendulum located at the center of the diamond NV center with effective moment of inertia $I_{eff}$ (equal to half of the total moment of inertia), we calculate the frequency shift $\delta_i$ due to the small change in spring constant $\kappa_i$ to be

$$\delta_i \approx \frac{\kappa_i}{2I_{eff}\omega_m}. \tag{2.12}$$

So, we find the frequency shifts to be

$$\delta_{\pm 1} = -\frac{\hbar\Delta}{2I_{eff}\omega_m}\frac{B_{ext}}{B_{ext}\pm B_{zfs}}, \tag{2.13}$$

$$\delta_0 = \frac{\hbar\Delta}{2I_{eff}\omega_m}\frac{2B_{ext}^2}{B_{ext}^2-B_{zfs}^2}. \tag{2.14}$$

We can simplify the system Hamiltonian by expanding $\theta^2$ in the interaction term of $H_{NV}$ in creation and annihilation operators and dropping rotating terms (because $\omega_m \approx 10$ MHz $\ll \omega_i \approx 1$ GHz), giving

$$H = \hbar\omega_m\left(\hat{n}+\frac{1}{2}\right) + \sum_{i=-1}^{+1}\hbar\omega_i|i\rangle\langle i| + \sum_{i=-1}^{+1}\hbar\delta_i\left(\hat{n}+\frac{1}{2}\right)|i\rangle\langle i|. \tag{2.15}$$

The sum involving $\delta_i$ represents the measurement (interaction), and it commutes with the rest of the Hamiltonian as is needed for a QND measurement.

Experimentally, the effect of $\delta_i$ on the NMO frequency may only be detectable when the NV spin state changes. The observable shifts, considering only transitions which can be driven directly, are then:

$$\delta_{0\pm} = \delta_{\pm 1} - \delta_0 = \frac{\hbar\Delta}{2I_{eff}\omega_m}\frac{B_{ext}\left(3B_{ext}\mp B_{zfs}\right)}{B_{zfs}^2 - B_{ext}^2}. \tag{2.16}$$

In the strong interaction limit where $B_{ext}$ approaches $B_{zfs}$, we obtain

$$\delta_{0-} \approx 2\delta_{0+} \approx \frac{\hbar\Delta}{I_{eff}\omega_m}\frac{1}{1-B_{ext}/B_{zfs}}. \tag{2.17}$$

The result of the interaction is that a change in the spin state (e.g. from $|0\rangle$ to $|-1\rangle$) appears as a change of the NMO frequency $\Delta\omega_m = \delta_{0-}$. Similarly, a change in the NMO number state (e.g. by $\Delta n = 1$) results in a change of the spin transition frequency $\Delta(\omega_{-1}-\omega_0) = \delta_{0-}$. Note that the measurement is QND in both directions. Since $\delta_{0-}$ is approximately a factor of

2 larger than $\delta_{0+}$, we will focus on detecting transitions between the $|0\rangle$ and $|-1\rangle$ spin states. The experimental value of $\delta_{0-}$ will depend strongly on the details of the system geometry. The table below summarizes the expected coupling strengths with $B_{ext} = 0.99B_{zfs}$ and 25 nm radius diamond nanocrystals on NMOs of specific dimensions made of the two thin films.

| Film | Auminum Oxide | | Graphene | |
|---|---|---|---|---|
| Length | 2 $\mu$m | | | |
| Width | 1 $\mu$m | | | |
| Thickness | 4 nm | | 0.88 Å | |
| Mode | Torsional | Bending | Torsional | Bending |
| Coupling Strength (Hz) | 0.5 | 0.16 | 212 | 70.4 |

Table 2: Comparison of expected coupling strengths with torsional and bending modes of bridge devices fabricated using aluminum oxide and graphene

For a graphene ribbon of width = 200 nm, length = 2 $\mu$m, we estimate $\omega_m \approx 2\pi \times 2$ MHz using the material constants from [51]. Adding a diamond nanocrystal with diameter = 50 nm and an applied external field $B_{ext} = 0.95B_{zfs}$, we obtain $\delta_{0-} \approx 2\pi \times 1$ kHz, which could increase to $\delta_{0-} \approx 2\pi \times 4.7$ kHz with $B_{ext} = 0.99B_{zfs}$, which should be easily detectable.

We can measure the spin state of the NV center by driving the NMO to a classical state and measuring the oscillation frequency. Since this is a QND measurement, it could be performed continuously, allowing us to observe discrete jumps in the NMO frequency as the NV center spin state changes. For a high-fidelity measurement of the NV spin state, we need to resolve the shift of $\delta_{0-}$ associated with a spin state change quickly compared to the lifetime of the spin state. With the proposed values of $\delta_{0-} \approx 2\pi \times 1$ kHz, we anticipate being able to resolve the shift quickly compared to any of these times. So, this experiment could be successful over a wide range of temperatures, and either thermally or microwave-driven spin transitions should be observable.

The interaction term of the Hamiltonian shifts the NMO frequency depending on the NV spin state, and similarly shifts the NV spin transition frequency depending on the NMO

number state. In principle, the NMO number state could be read off continuously by making a continuous measurement of the NV center frequency.

# 3.0 FILM FABRICATION

As described in Chapter 1, one of the first parts that went into the fabrication of devices, was the fabrication of the NMO. The right choice of material was very critical for fabricating the NMO. Our first choice was graphene as the material, due to its low mass and moment of inertia, and thus large coupling strengths $\delta_i$, as described in Chapter 2. But due to the thinness of graphene ($\simeq$0.3 nm), it is extremely fragile, which caused problems in our fabrication and detection steps. Therefore, we started working with aluminum oxide, in parallel with graphene, as it was a much more robust material. We successfully fabricated NMOs out of aluminum oxide, the growth of which is described in this chapter and further processes will be described in Chapter 4. As time progressed and we got better with the fabrication techniques, we were able to successfully fabricate NMOs out of graphene as well, again growth of which is described here and the rest in Chapter 4.

## 3.1 DIAMOND TURNING

The first step in most of our fabrication processes is Single Point Diamond Turning (SPDT). This ultra-precision machining technique yields nanometer-scale surface roughness in copper [53]. The machining accuracy of SPDT results from an air-bearing spindle, hydraulically levitated slides, feedback from optical readout of the slide positions and precision-shaped single-crystal diamond cutting tools. SPDT is a simple process, similar to cutting on a conventional lathe. It is scalable to large diameter discs ($\sim$2000 mm) [54], and can be used to produce $\sim$100 mm diameter discs with a overall flatness of $\sim$100 nm [55]. Feed rates for finish cuts on copper with SPDT are typically 5 mm/min. Furthermore, this process does not leave any impurities embedded in the diamond-turned surface. Due to these attractive features, SPDT has been researched as an alternative technique for preparing silicon wafers [56].

The model number of the diamond turning machine in our lab is Nanotech 250UPL (ultra-precision lathe) from Moore Precision Tools.

We used SPDT during device fabrication for the following purposes:

- We flattened both faces of the aluminum discs that were used to grow an aluminum oxide film for NMO fabrication.

- We flattened both faces of the copper discs that were used to grow graphene.
- We also used the diamond turning machine to flatten and put grooves in the substrates that were used to suspend the fabricated NMOs. For the details on this refer to Chapter 4

## 3.2 ALUMINUM OXIDE GROWTH

- We started with 1mm thick, 1" in diameter, 99.999% pure aluminum discs.
- These discs were then annealed at 500°C in air, for 8 hours.
- The discs were then diamond-turned, as the flatness of the surface mattered for the next step of anodization.
- The surface of these discs was then electrolytically anodized in presence of tartaric acid and ammonium hydroxide, to form ∼6-9 nm thick aluminum oxide [57]. This anodization was carried out in the home-made fixture described in Section 4.3.2 and shown in Fig. 18.
- The samples were checked under an ellipsometer, before and after anodization, to measure the thickness of the grown film and to account for any native oxide.

Further details of the growth and thickness measurement process will be given in Jen's future thesis [58].

## 3.3 GRAPHENE GROWTH

Interest in isolating or fabricating single to few-layer graphene films is driven by its extraordinary electronic [59], thermal [60], mechanical [61] and optical properties [62]. Despite the challenges associated with the production of graphene, it finds extensive use in a variety of applications ranging from chemical sensors [63] to transistor fabrication [64, 65]. Processes such as mechanical [66] and chemical [67] exfoliation, epitaxial growth on silicon carbide (SiC) [68], and catalyzed growth on transition metal substrates using chemical vapor deposition (CVD) [69] have been employed to produce graphene films. Each such method has its advantages and difficulties. Of these processes, mechanical exfoliation produces graphene

that is structurally superior to all others, but gives the least control over the size, location and thickness of the film. Epitaxial graphene grown on SiC is found to be flat and smooth, with a root-mean square (RMS) roughness of $\leq 0.05$ Å [70], but has been found to have mechanical and electrical drawbacks, such as the presence of a buffer layer under the graphene layer, and inherent charge non-neutrality [71]. CVD growth of graphene on metal substrates, such as nickel and copper [72, 73, 74, 75, 76, 64, 77], is presently the most commonly used technique for producing large-area graphene films. We have developed novel copper substrates with greatly improved flatness and large copper domains for CVD of graphene.

CVD growth of graphene on copper is one of the most promising approaches due to its tendency to self-limit at a single layer of graphene [72], due to low carbon solubility in copper, and its scalability [78]. After years of improvements in CVD growth conditions, $25 - 125$ $\mu$m thick copper foil is still the most commonly used substrate for CVD graphene growth [69, 79, 80], despite the impact of its surface roughness and polycrystalline structure on the grown graphene [81, 82].

Aside from the intrinsic wrinkles on graphene due to thermal fluctuations [83, 84], roughness on a wide range of length scales can get added to graphene grown on copper during the growth or transfer process, e.g. due to the initial roughness of the copper substrates used for CVD growth. Furthermore, the ratio of single-layer and multi-layer graphene areas seems to depend on the roughness of the underlying copper foil [85]. Problems with roughness of the copper foil can be addressed by electrochemical polishing, which can reduce the roughness of the foil from several hundred nanometers by a factor of 10 to 30 before CVD growth [85]. Copper can also be polished mechanically before graphene growth, but the polishing process leaves impurities, such as alumina particles, in the foil. These impurities can act as nucleation sites for multi-layer graphene [86]. Graphene films can be forced flat after growth by transfer onto a flat surface [87].

There are conflicting reports about the dependence of the graphene domain orientation and size on the domains of the underlying copper [88, 89, 90], but larger copper domains at least provide an opportunity for larger areas of consistent graphene growth. The maximum reported copper domain size of 25 $\mu$m thick copper foils used for graphene growth is $\sim$ 1 cm [91].

Alternative copper substrates have been employed for graphene growth, such as epitaxially sputtered single-crystal copper films with roughness $\sim 1$ nm [92] or evaporated copper films [93]. A strong dependence of the graphene growth on the underlying copper structure is observed on either film. CVD processes on such thin film substrates often use copper enclosures to balance evaporation of the thin copper films at graphene growth temperatures [92]. A more extreme approach to mitigate the effects of copper structure is to grow graphene on molten copper with a tungsten or molybdenum support to prevent dewetting of the copper [94].

We developed a method of preparing ultra-flat copper and using it as a substrate for growing graphene by CVD. Compared to electro-chemically polished copper foil, this process results in 50 times smoother graphene on copper and at least 5 times larger copper domains. This method uses CVD growth conditions commonly utilized for copper foil without any special modifications, and is fully scalable to wafer-size graphene growth. For the CVD process we used a Split Hinged Tube Furnace (Lindberg/Blue M: HTF55347), with a quartz tube (Technical Glass: Fused Quartz Tubing, 50 mm ID, 55 mm OD, 4 feet long). We realized that the temperature inside the furnace was not the same as the temperature measured by the furnace controller.[1] The following table gives a conversion chart between the temperature measured on the tube furnace controller and the temperature measured on an external thermocouple inserted into the furnace, but outside the tube (this is considered as the actual temperature). The intermediate or lower temperatures can be interpolated or extrapolated, respectively. In the procedures below, only the actual temperatures are mentioned (and in some places the controller temperatures are mentioned in parenthesis). Over the years, there have been a few inconsistencies in the comparison between these two temperatures (as seen in the first column of the table below, and AP processes outlined below), which might have been due to the difference in placement of the external thermocouple, or other physical changes, such as placement of ceramic insulation around the tube etc. The way around this is to perform such a calibration once every year or so, or after making major changes to the tube or the furnace.

[1] This was realized in Feb-March, 2013 - Thus, any processes done before that time were performed trusting the furnace temperature.

| Controller Temperature (°C) | Actual Temperature (°C) |
|---|---|
| 941-948-953 | 1000 |
| 983 | 1035 |
| 998 | 1050 |
| 1033 | 1085 |

Table 3: Comparison between the temperature measured on the tube furnace controller and on an external thermocouple (this is considered as the actual temperature)

To make ultra-flat copper substrates, we started with a 30 cm long oxygen-free electronic (OFE) grade ultra-pure (99.99%) copper rod, 25.4 mm in diameter (McMaster part: 8965K191). To relieve stress and enlarge the copper grain structure, we annealed a 20 cm long piece of this rod in an atmosphere of hydrogen ($H_2$) flowing at 16 sccm (pressure of $\sim$ 150 mTorr) at 1000°C for 24 hours.[2] We then cut $\simeq$ 1.6 mm thick disc-shaped slices out of this rod by conventional machining, on a lathe in the machine shop. Since the substrates were sliced from a bulk copper rod, the graphene growth surface of the substrates had minimal contamination or damage from the original manufacturing process of the rod.

Initially, both faces of the copper discs were cut flat to an RMS roughness of $\approx$ 2 nm by SPDT, with a 1.5 mm radius single-crystal diamond tool, A photograph of one such disc getting cut by SPDT is shown in Figure 6.

[2]The 24 hour annealing step was added in Aug, 2012, before which we annealed them for 2-12 hours.

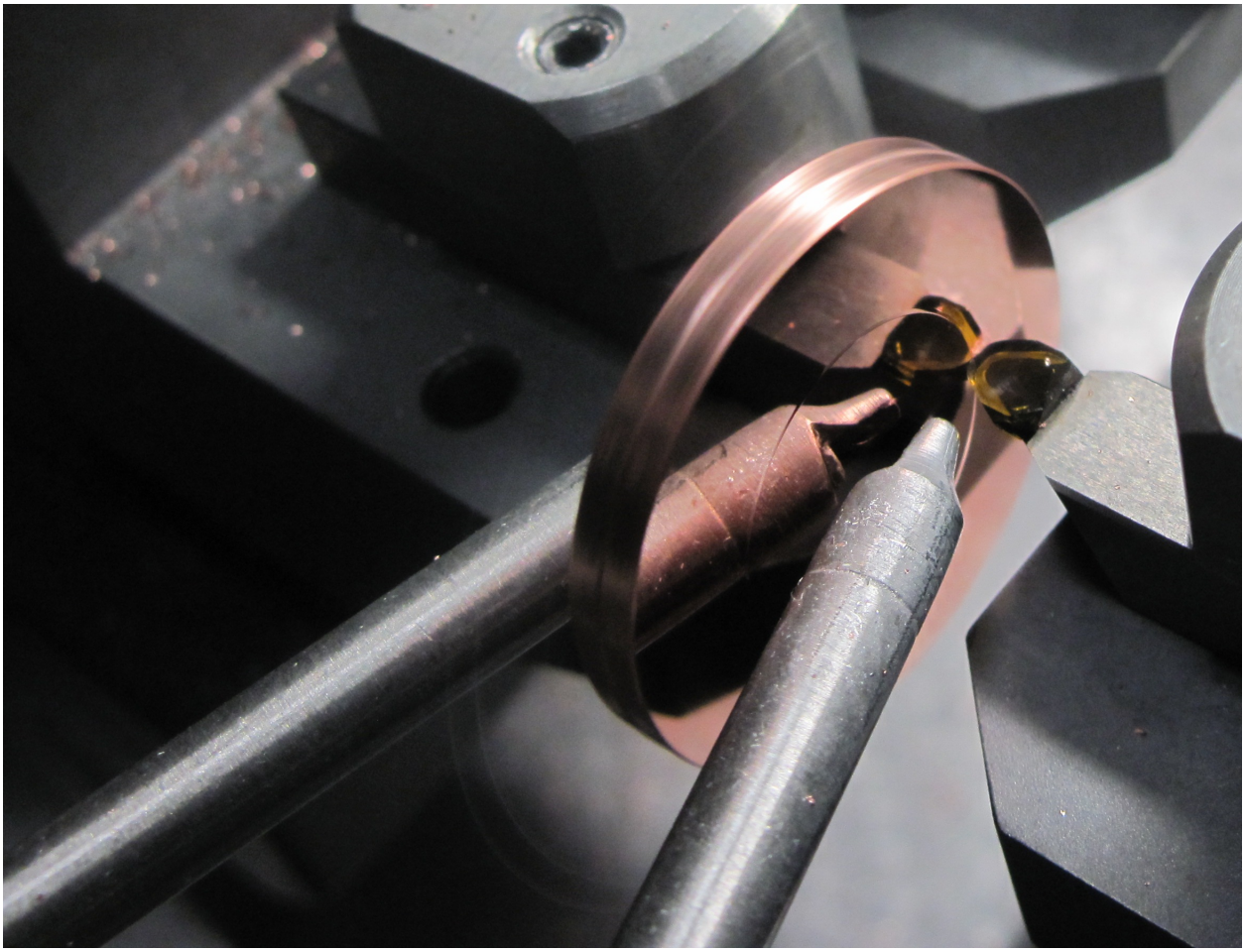

Figure 6: Photograph of a copper disc being cut by SPDT on an ultra-precision lathe.

After SPDT, there may still be significant stress in the copper from the initial machining. To relieve the stress, the discs were again annealed for 8 hours under the same conditions as the initial annealing of the rod. After this re-annealing, some surface deformation is typically visible. The discs were then re-diamond-turned, after which they were ready to be used as substrates for graphene growth. This final SPDT step introduces little new stress compared to conventional machining [53]. The procedure of the fabrication of thick ultra-flat substrates is illustrated in Figure 7.

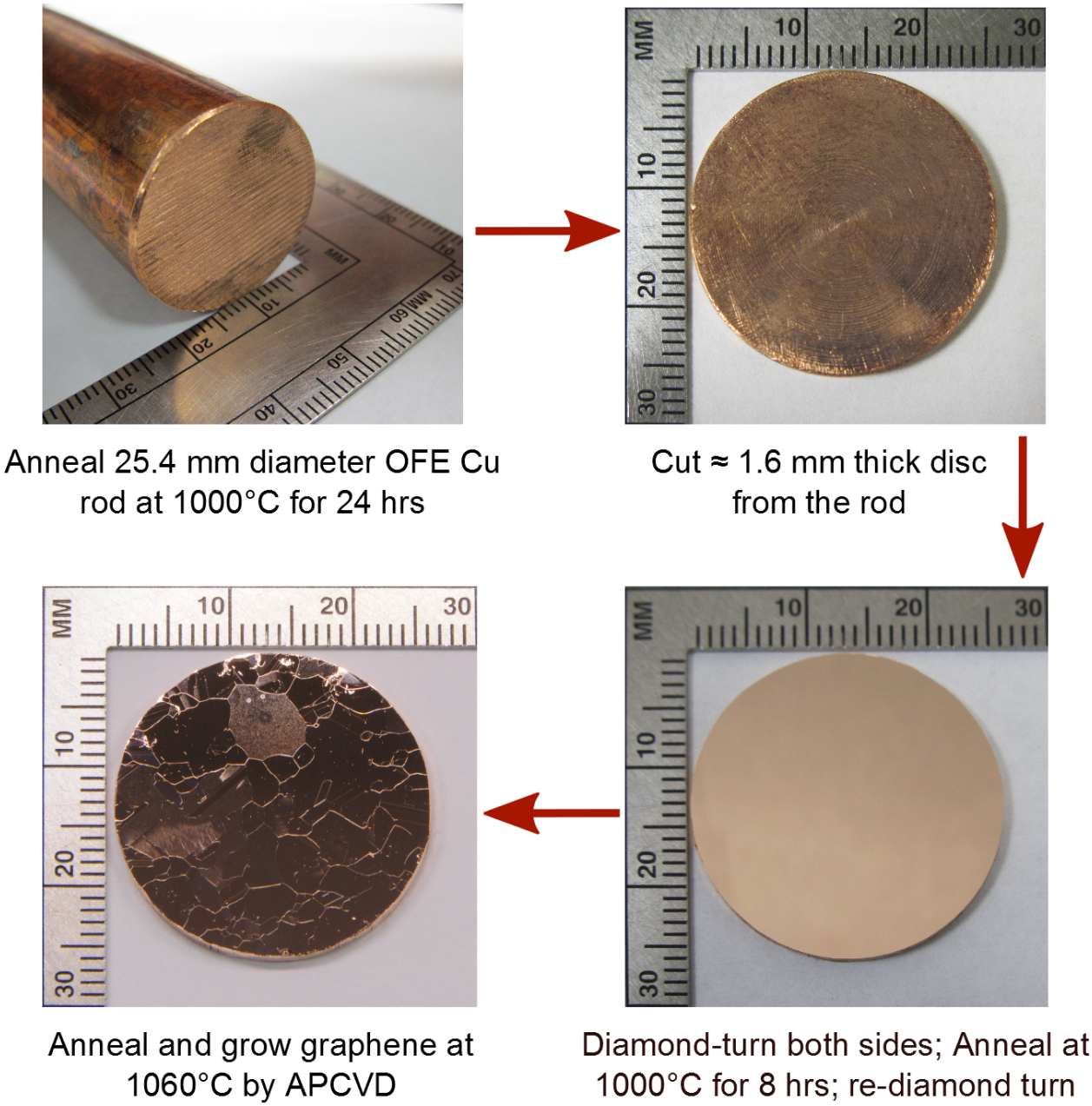


Figure 7: Process for preparation of graphene grown on thick diamond-turned copper substrates.

The initial flatness of the copper substrate may be inconsequential if it is destroyed during the graphene growth. To study the change in roughness, we employed two different methods of growing graphene on these substrates: Atmospheric Pressure CVD (APCVD)

and Low Pressure CVD (LPCVD).

### 3.3.1 Low Pressure Procedure

The annealing temperature of OFE copper is known to be between 375-650°C, and the melting point of OFE copper is expected to be ∼1085°C.

**Previous Attempts:**[3]

**3.3.1.1 LP Annealing** For LP annealing of the copper samples, we used to:

1. pump down the samples - the pressure used to get down to ∼ 5-15 mTorr.
2. vent the furnace with 100 sccm of nitrogen ($N_2$) - the pressure used to go up to ∼ 560 mTorr. After turning the $N_2$ off, the pressure used to come back down to ∼ 5-10 mTorr.
3. then put 8 sccm of hydrogen ($H_2$) on. The pressure used to rise up to ∼ 90 mTorr.
4. ramp up the temperature to 1000°C, without any programming on the furnace controller, and let it sit there for 2 hours. Over the years this annealing time was varied from 2-8 hours.
5. physically turn off the switch on the furnace to let it cool down, after the stipulated time.
6. leave it for cool down overnight with hydrogen still flowing. (Initially during the cool down, I used to vent the furnace with $N_2$ while the temperature was ∼350°C. This used to leave the surface of the discs rough and with some black spots. I stopped doing this after the first couple times.)

**3.3.1.2 LP Graphene Growth** We started the LPCVD of graphene by following the procedure mentioned in paper [72], trying to keep the gas flow rate ratios, temperatures and procedure times the same as mentioned in the above paper. The ratio of flow rates of methane ($CH_4$) to $H_2$ as used in this paper was kept at 17.5, with growth temperature at 1000°C and growth time as 30 minutes. We used to:

1. pump down the samples - the pressure used to get down to ∼ 5-15 mTorr.

[3] We used to use Dr. Choyke's old tube furnace and tube for the first year

2. vent the furnace with 100 sccm of nitrogen ($N_2$) - the pressure used to go up to $\sim$ 560 mTorr. After turning the $N_2$ off, the pressure used to come back down to $\sim$ 5-10 mTorr.
3. flow hydrogen ($H_2$). The pressure used to rise up, as mentioned in Table 4.
4. ramp up the temperature to 1000°C, without any programming on the furnace controller.
5. wait for 30 minutes to let the samples equilibrate after the furnace reached 1000°C, and then flow $CH_4$. This rose the pressure, as mentioned in Table 4.
6. let the graphene grow under these conditions for 30 minutes.
7. turn off the furnace switch and let it cool down till $\sim$ 650-750°C, before putting the $CH_4$ off and leaving it overnight to cool down to room temperature with $H_2$ flowing.

Following are the growth parameters and results obtained for some early LPCVD graphene growth tries.

| S.N. | $H_2$ flow rate (sccm) | Pressure (mTorr) | $CH_4$ flow rate (sccm) | Pressure (mTorr) | Observation (using Raman Microscope) |
|---|---|---|---|---|---|
| 1 | 4 | 40-50 | 70 | 680-750 | Seemed to give bi/multi-layer |
| 2 | 8 | 80-90 | 70 | 680-750 | Seemed to give bi/multi-layer |
| 3 | 16 | 130-140 | 70 | 800-850 | Gave the best single-layer graphene |
| 4 | 8 | 70-80 | 35 | 400-450 | Seemed to give multi-layer |

Table 4: Some of the earlier graphene growth attempts - growth parameters and results

These tries helped us in fixing our $H_2$ and $CH_4$ flow rates to 16 sccm and 70 sccm, respectively, with 30 minutes as the growth time (time for which the $CH_4$ was flowing at 1000°C). [4]

[4]Methane-based initial graphene growth tries were conducted between Jan-March, 2010.

For the fabrication of the NMOs, another idea that we wanted to try was to make **Corrugated Graphene**, such as shown in [95]. We were hoping that such rippling/corrugations would decrease the stiffness of the NMO, lowering its resonant frequency and thus increasing the interaction with the NV, as can be seen using equation Eq. (2.17). A schematic of a corrugated graphene bridge device is shown in the figure below.

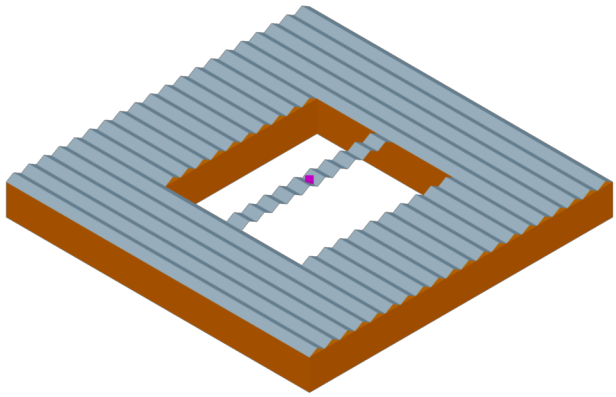

Figure 8: A schematic of a corrugated graphene bridge device that we tried to fabricate using $C_2H_2$ as the carbon source

We tried to do this by making 500 nm - 10 $\mu$m deep grooves on our copper substrate, using a 90° point tool on the diamond-turning machine. Unfortunately, grooves shallower than 5 $\mu$m could not survive the graphene growth cycles, and grooves larger than that were quite useless as the longest dimension of the NMOs would be smaller than that. We tried shorter growth cycles as well, where we'd push the sample into the furnace only after it has reached 1000°C, start $CH_4$ as soon as the sample temperature equilibrated, and leave the $CH_4$ for minimum time needed to grow graphene. This gave us the same negative result too. Our speculation was that at temperatures as high as 1000°C, copper on the surface moves around a lot and quite fast, thus making hard for the grooves to hold their shape. We experimentally realized that the grooves on the copper surface were able to survive temperatures as high as 900°C. We tried to take advantage of this by trying to grow graphene using **acetylene ($C_2H_2$) as the carbon source**, as was known that graphene with acetylene can be grown at

lower temperatures [96]. We did a few growth tries using $C_2H_2$, while changing the annealing temperature, growth temperature, gas flow rates etc. All such tries with acetylene as the carbon source produced graphene with a very prominent D peak, which usually signifies that the graphene is defective in some way or another. Because of this reason, we dropped the idea of growing graphene using acetylene, and with it the idea of corrugated graphene.[5]

Some time later, we learned how to **program the tube furnace controller**, so that we could ramp it up at a controlled rate and did not have to physically turn it off for it to start cooling down. We also realized, with the help of an external thermo-couple again, that the furnace would shoot up to ∼1015°C, before coming back down to 1000°C. To circumvent this problem we then ramped up the temperature at a slower rate as it approached 1000° C.[6]

**Latest Method**: After all of these attempts, following is the latest LPCVD procedure we were using before switching to AP Annealing and CVD in Feb, 2013.

The samples are heated to 950°C at a rate of 10°C/min and then to 1000°C at a rate of 2°C/min, in an atmosphere of 16 sccm of $H_2$ (pressure ∼ 150 mTorr). For LP annealing the samples were left under these conditions for 1 hour. For LPCVD of graphene, the samples were left in $H_2$ for 30 minutes and then 70 sccm of methane $CH_4$ was added to the tube (pressure of ∼ 700 mTorr), for another 30 minutes. After this time, the furnace was turned off and allowed to cool down with both $CH_4$ and $H_2$ still flowing. The $CH_4$ was turned off when the furnace temperature reached ∼ 650 °C. The samples were left to cool overnight in the presence of $H_2$.

### 3.3.2 Atmospheric Pressure Procedure

After using LPCVD as the primary growth technique for over 3 years, we switched to APCVD growth of graphene around February, 2013 (some of the initial testing of parameters for the following AP procedures was done by Jen [58]).[7] This switch in techniques was motivated by works that reported growth of dendritic domains with LPCVD and symmetric hexagonal domains with APCVD [79, 97]. For the purposes of AP procedures, we stopped using pure

[5] Acetylene-based graphene growth tries were conducted between June-Aug, 2010.
[6] These changes were made around April-May, 2012.
[7] The presently used recipes got finalized around April, 2013.

$H_2$ and pure $CH_4$ gases. Instead, we started using gas mixtures: 2.5 vol % $H_2$, balance Argon (Ar) and 0.1 vol % $CH_4$, balance Argon (Ar).

**3.3.2.1 AP Annealing** By the time we started performing APCVD of graphene, we had started annealing the cut discs for 8 hours. Following is the latest AP annealing procedure followed, until the end of my time in the lab. We used to:

1. pump down the samples - the pressure would get down to $\sim$ 5-15 mTorr. To pump the system down, we used to put a quick-disconnect cap, with a clamp, on the exhaust line, the purpose of which is explained below.
2. flowed 70 sccm of $H_2$/Ar mixture. The pressure would rise up to $\sim$ 280 mTorr.
3. then remove the clamp on the exhaust, and the cap would hold due to low pressure in the tube. We'd then close off the valve that connected the vacuum pump to the system, with the gas mixture still flowing. This then started filling the system with the gas mixture and pressure started building up in it. The pressure used to rise up to $\sim$ 97-100 Torr, at which point the cap on the exhaust line would fall off.
4. start a program on the furnace controller, that ramped-up the furnace to 1000°C (as seen on an external thermocouple - which was actually 941°C on the furnace controller), and would let it sit there for 8 hours.
5. then let the program in the controller cool down the furnace to room temperature, and we would close off the gas mixture after the system had sufficiently cooled down, which would usually be overnight.

**3.3.2.2 AP Growth** Following is the latest AP growth procedure followed, until the end of my time in the lab. We used to:

1. pump down the samples - the pressure used to get down to $\sim$ 5-15 mTorr. To pump the system down, we used to put a quick-disconnect cap, with a clamp, on the exhaust line, the purpose of which is explained below.
2. then flow 186 sccm of $H_2$/Ar mixture (Maximum allowed flow rate on each MKS Mass-Flo Controller is 100 sccm. Therefore, the above flow rate of 186 sccm was achieved by

flowing 93 sccm each through two controllers). The pressure used to rise up to $\sim$ 560-570 mTorr.

3. then remove the clamp on the exhaust, and the cap would hold due to low pressure in the tube. We'd then close off the valve that connected the vacuum pump to the system, with the gas mixture still flowing. This then started filling the system with the gas mixture and pressure started building up in it. The pressure used to rise up to $\sim$ 97-100 Torr, at which point the cap on the exhaust line would fall off.

4. then start a program on the furnace controller that ramped-up the tube to growth temperature. This temperature ramp-up was done in 3 steps, to prevent overshooting of temperature, as the AP Growth was done quite close to the melting point of copper. The temperature was ramped-up to $\sim$1000°C (953°C on furnace controller) at a rate of 10°C/min; it was then taken up to $\sim$1035°C (983°C on furnace controller) at a rate of 2°C/min; finally it was ramped up to $\sim$1050°C (998°C on furnace controller) at a rate of 1°C/min. The furnace then stayed at this temperature for 2.5 hours.

5. after letting the samples sit at this temperature for 1 hour, flow 14 sccm of $CH_4$/Ar mixture into the tube, and this growth environment stayed as such for the remaining 1.5 hours. The pressure on the vacuum gauge read 86-88 mTorr during this time.

6. after this annealing time, let the program in the controller cool down the furnace to room temperature. $CH_4$/Ar gas mixture was turned off after the furnace cooled down to $\sim$650°C. $H_2$/Ar was allowed to flow overnight and was closed off after the system had gotten sufficiently close to room temperature (usually below 50°C).

Graphene grown on these substrates was characterized using a Raman microscope and a Scanning Electron Microscope (SEM). As can be seen in Fig. 9, the Raman spectra of graphene on all three substrates show that they mostly have single-layer graphene [98, 99, 100]. SEM characterization of graphene on a thick substrate with intentionally incomplete APCVD graphene growth shows a graphene domain with size near 70 $\mu$m (Fig. 9), which is the typical largest domain size obtained on these substrates.

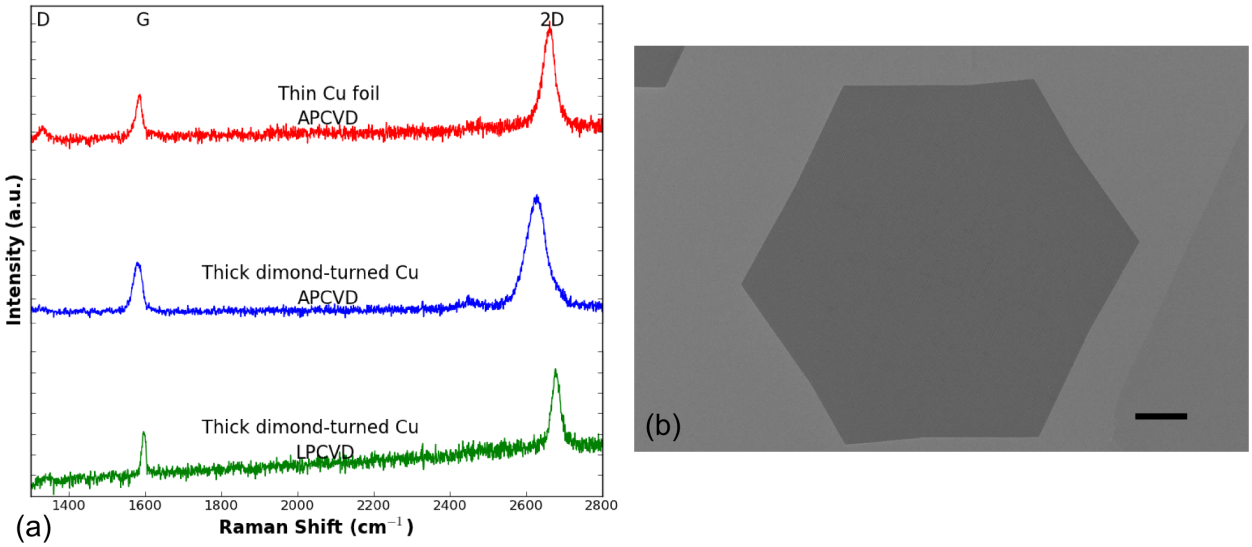


Figure 9: Characterization of graphene grown on thick ultra-flat copper discs. (a) Raman spectroscopy with 633 nm laser shows that all three substrates mostly have single-layer graphene. (Background, as measured on diamond-turned copper, was subtracted out.) (b) SEM image of a hexagonal $\simeq 70$ $\mu$m graphene domain grown by APCVD on ultra-flat copper (scale bar is 10 $\mu$m).

**3.3.2.3 AP large-domain graphene growth** Using the AP growth procedure described above we used to obtain 70-100 $\mu$m big hexagonal single-layer graphene domains. At times a few such hexagonal domains used to have a wrinkly patch at the center, which under the Raman microscope were confirmed to be bi/multi-layer graphene patches. To try to make some NMOs with bi/multi-layer graphene, I tweaked some of the growth parameters to achieve larger areas with bi/multi-layer graphene instead of just the centers of the hexagons. In the process of doing so a serendipity happened (in November, 2013) – We obtained $\sim 1$ mm big single-layer hexagonal domains! We could not trace out exactly how this happened in this accidental run, but this proved that we could obtain such large domains in our setup, and it thus steered us in the direction of this wild goose chase!

In trying to further experiment in this direction, and with the help of other published works [91], we realized that oxygen plays a very important role in graphene nucleation on

the copper substrate. We thus started growing graphene on oxidized copper discs, using the procedure outlined below, and the biggest domains we got from this procedure were $\sim$ 2.5-3 mm.

**LP Oxidation**: For the growth of large-domain graphene, we oxidize the growth substrate, before growth, with 10 sccm of $O_2$ at low pressures (the pressure goes up to $\sim$110 mTorr with the oxygen flowing), at 150°C for 1 hour.

We then use these oxidized growth substrates, at times alongside a usual un-oxidized substrate for comparison, to grow the large-domains of graphene. These oxidized substrates reduce the nucleation density of graphene, thus leaving more space for a single domain to grow in, if all other conditions are favorable.

Following is the procedure we would then follow for the **growth of large-domain graphene**. We used to:

1. pump down the samples - the pressure used to get down to $\sim$ 5-15 mTorr. To pump the system down, put a quick-disconnect cap, with a clamp, on the exhaust line, the purpose of which is explained below.
2. then flow 181.4 sccm of pure Ar gas (Maximum allowed flow rate on each MKS Mass-Flo Controller is 100 sccm. Therefore, the above flow rate of 181.4 sccm was achieved by flowing 90.7 sccm each through two controllers). The pressure used to rise up to $\sim$ 530 mTorr.
3. then remove the clamp on the exhaust, and the cap would hold due to low pressure in the tube. We used to then close off the valve that connected the vacuum pump to the system, with the Ar gas still flowing. This used to then start filling the system with the gas mixture and pressure started building up in it. The pressure used to rise up to $\sim$ 28-30 Torr, at which point the cap on the exhaust line used to fall off.
4. then start a program on the furnace controller that ramped-up the tube to growth temperature. This temperature ramp-up was done in 3 steps, to prevent overshooting of temperature, as the AP Growth was done quite close to the melting point of copper. The temperature was ramped-up to $\sim$1000°C (953°C on furnace controller) at a rate of 10°C/min; it was then taken up to $\sim$1035°C (983°C on furnace controller) at a rate of

2°C/min; finally it was ramped up to ∼1050°C (998°C on furnace controller) at a rate of 1°C/min. The furnace was programmed to stay at this temperature for 4.5 hours.

5. then start flowing 4.7 sccm of pure $H_2$ as soon as the furnace reached its maximum temperature of ∼1050°C (998°C on furnace controller).

6. after letting the samples sit under these conditions for 0.5 hour, flow 30 sccm of $CH_4$/Ar mixture into the tube, and this growth environment stayed as such for the remaining 4 hours. The pressure on the vacuum gauge read 75-77 Torr during this time.

7. after this growth time, let the program in the controller cool down the furnace to room temperature. $CH_4$/Ar gas mixture was turned off after the furnace cooled down to ∼650°C. $H_2$ and Ar were allowed to flow overnight and was closed off after the system had gotten sufficiently close to room temperature (usually below 50°C).

**Results and Observations:** Using this method, the graphene domain size increased from 70 $\mu$m to 3 mm. The domains got big enough to be seen by naked eye. To visualize the domains after growth, we heated the samples in air at 300°C for 5 minutes. This would oxidize the copper not covered with graphene, leaving graphene as shiny-looking spots. At this point, I was measuring the width of the hexagons, using a ruler, to estimate the domain size and growth rate.

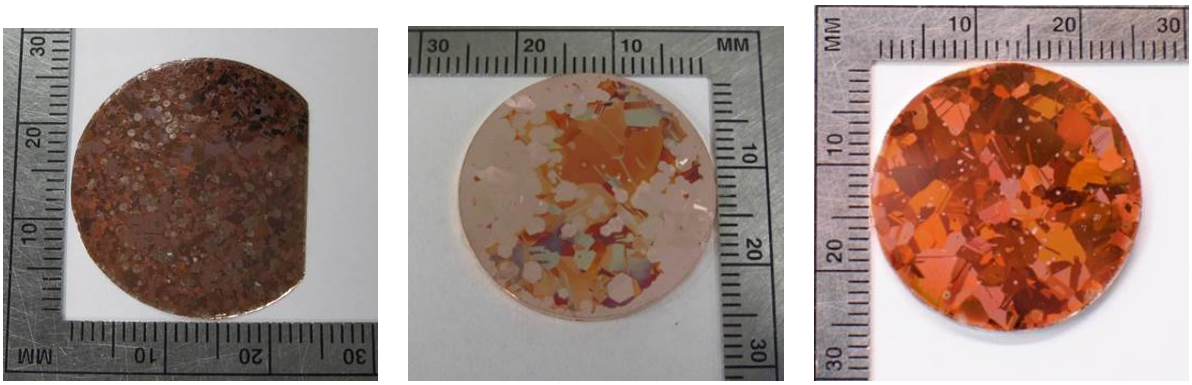

(a) (b) (c)

Figure 10: Results obtained using the AP large-domain growth technique (a)The domains grew large enough to be visible with naked eye; their contrast was increased by baking the samples in air, (b)We achieved 1-3 mm graphene domains using this technique and (c)Using oxidation techniques we also achieved a low nucleation density of graphene on the sample.

#### 3.3.2.4 AP Progressive Growth

**Introduction:** There have been quite a few recent advances in growing large-domain graphene using Chemical Vapor Deposition (CVD) on metals such as copper (Cu) [101]. Substrate polishing and annealing [102], and presence and absence of hydrogen [79, 103] and oxygen [91, 104, 82] have been found to play an important role in growing large single-crystal graphene. Large domains of graphene (70 $\mu$m - 1cm) have been successfully grown by controlling such parameters, far short of wafer-scale single-domain graphene. Instead of simply tuning the growth conditions, it appears that a more dramatic change in the process is needed to enable better control over the growth, including decreasing the nucleation density [82].

**Our Method:** We have developed a method to grow large-area, single-domain graphene by controlling the growth through a sharp gradient in the CVD gas concentrations over a copper substrate. Since the graphene growth process involves a competition between carbon from methane adding to the graphene film and hydrogen etching back the graphene, the

ratio of the methane and hydrogen concentrations can be used to control the growth rate (from growth to etching) and morphology (from dendritic to hexagonal). Furthermore, oxygen in the copper or on the copper surface can suppress nucleation of new graphene domains, block graphene growth, or even remove graphene. Our approach is to create a spatial gradient in the gas concentration such that growth is favorable in one region of the sample and unfavorable in another region. This spatial gradient is then moved across the substrate to gradually expand the region favorable for growth to cover the whole substrate. Ideally, the graphene growth is nucleated at a single point at one edge of the substrate, and the single resulting graphene domain spreads across the entire substrate as the region favorable for growth expands. Graphene growth is not re-nucleated elsewhere on the sample because almost the entire region which is not favorable to nucleation and growth is covered by graphene. This is a two-dimensional analog of the Czochralski process used for growing silicon boules, with the liquid interface replaced by the gas gradient. It may also be beneficial to create a third region, by a second gradient in the gas concentrations, where growth once again becomes unfavorable but graphene on the surface is not removed. This region would protect areas where graphene has already grown from etching or further growth into multilayer graphene.

**Experimental Details:** To grow the large single-crystal graphene, we start with large-domain ultra-flat copper substrates [43]. A 100 $\mu$m deep dimple is made in these discs, $\approx$ 10.7 mm in radius, and a 1/16 inch hole is drilled in them, $\approx$ 2 mm from the edge. These discs are then oxidized at low pressures ($\sim$ 100 mTorr), with 10 sccm of oxygen at 150°C, as described under LP Oxidation above.

Each sample on which graphene is to be grown is paired with a spacer of exactly the same thickness for reasons explained later. These spacers are also diamond-turned, but not necessarily annealed or oxidized. The sample and its corresponding spacer are loaded onto the sample holder with a quartz glass slide covering a fraction of the sample. a layout of the samples loaded in the sample holder and a scheme of the process is shown in the figure below

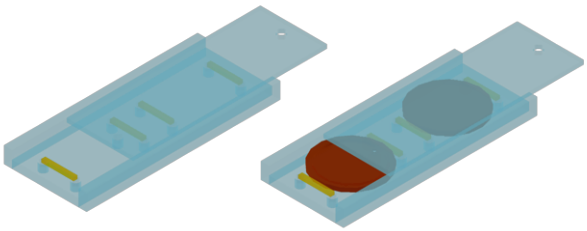

(a)

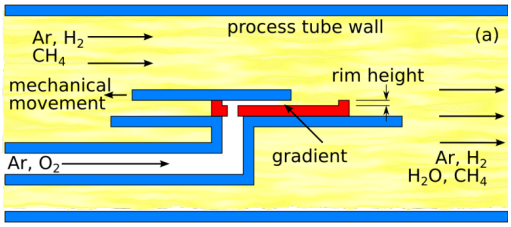


(b)

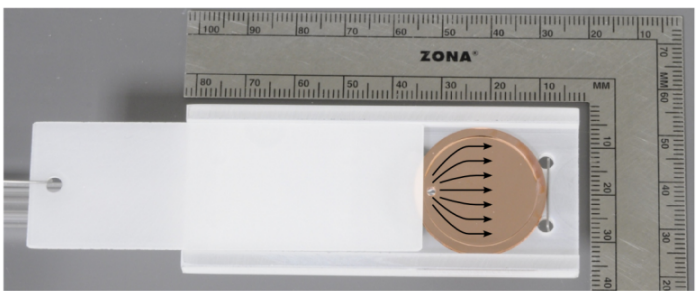


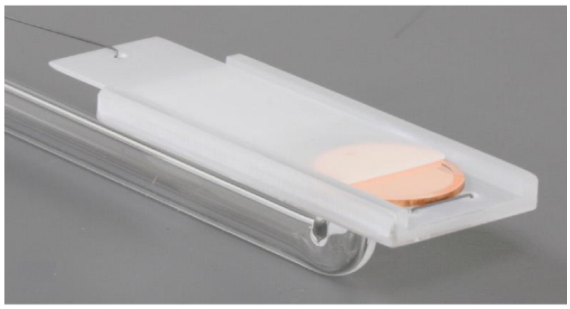

(c)

Figure 11: Progressive Growth setup for the growth of Large-domain graphene(a)Layout of the experimental setup with the discs on the sample holder, (b)Overall scheme of the method with gas flows and (c)Picture of the sample holder with a dimpled disc used for progressive growth of graphene. The black arrows signify the direction of flow of gases.

- We make sure that the hole in the sample lines up with the hole in the sample holder.
- A tungsten wire is attached to the covering glass slide in order to pull/push this slide over the sample.
- The sample holder is loaded into the tube furnace, and the tube is pumped down to ∼10 mTorr.
- The tube is then filled with 181.4 sccm of pure Argon gas. A fraction of the Ar is passed from the hole in the sample holder, and thus flows between the top of the sample and the glass slide. The rest of the Ar fills up the whole volume of the tube.
- The sample is then heated up to 1050°C, and is left at this temperature for 12.5-15.5 hours.

- When the sample reaches this highest temperature, we start flowing 4.7 sccm of pure hydrogen through the tube.

- After half hour of letting the hydrogen gas flow, we then flow 30 sccm of 0.1% $CH_4$/Ar mixture for 12-15 hours, and this is the time during which graphene grows on the surface of copper.

- We also pull back the quartz glass slide mentioned above during the whole time that the hydrogen and $CH_4$/Ar mixture is flowing. As mentioned above, the spacer paired with each sample is kept behind the sample, to provide a surface for the glass slide to smoothly slide on.

- After the graphene growth the furnace is left to cool down. $CH_4$/Ar mixture is turned off when the temperature get down to $\sim 650°C$.

- The tube furnace top is cracked open after this point, to let it cool down faster.

**Observations:** After the growth the samples are heated in air at 300°C for 5 minutes. This oxidizes the areas of the substrate which is not covered with graphene, helping in vizualizing the graphene domains. We are also trying to collaborate with other groups to visualize these domains better, using Low-energy electron microscopy (LEEM) and Low-energy electron diffraction (LEED).

Using this above method, we were able to increase our domain size from 2-3 mm to $\sim$5 mm.

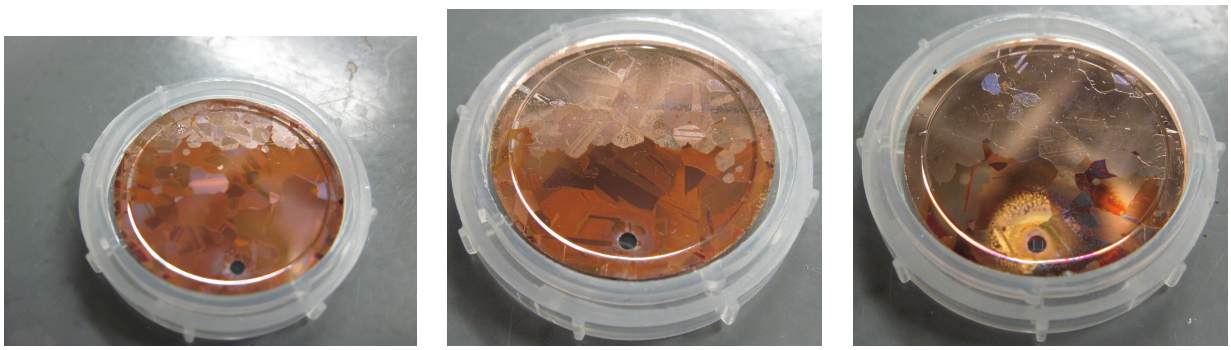

(a) (b) (c)

Figure 12: Results obtained using the AP progressive growth technique - We can control the graphene domain size by controlling the flow of oxygen getting to the sample

**Future Directions:** Lately we made a big breakthrough in this method using double-dimpled discs. This was initially done by making a 100 $\mu$m deep dimple on both sides of the sample. Eventually, due to diamond-turning issues, this was done by sitting the dimpled discs onto a glass slide with a pocket for the samples, to enable counter-flow of glasses. This was done to protect the bottom face of the samples from any graphene growth. The layout for this scheme and some preliminary results are shown in the figure below. As can be seen in these pictures, this scheme has further reduced the nucleation density (we obtained almost 2 sites/0.75 square inch), and increased the domain size (we have achieved $\sim$4-5 mm wide domains). We expect this technique to be useful in growing arbitrarily large domains.

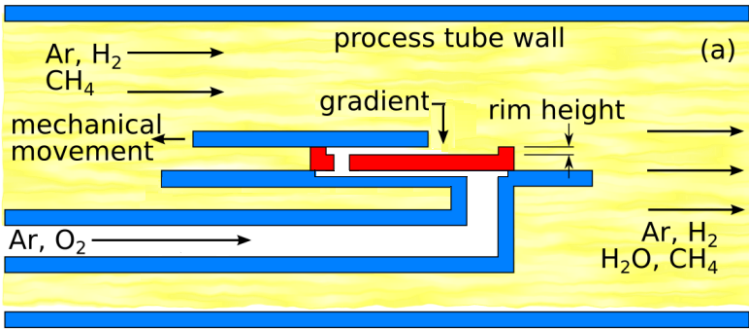


(a)

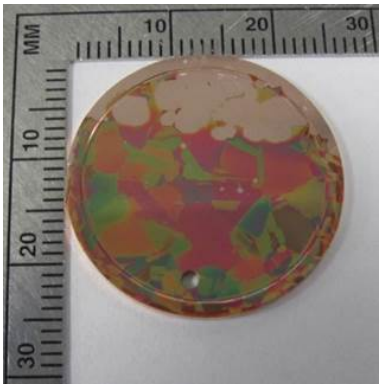


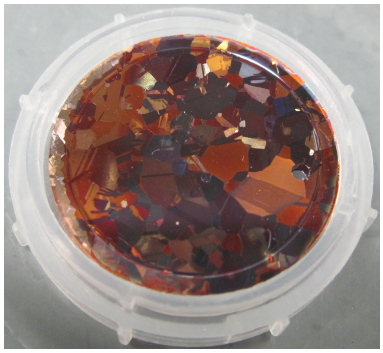

(b) (c)

Figure 13: Results obtained using the AP progressive growth technique, using double dimple: (a)Scheme of the experimental setup, (b)We have obtained 4-5 mm domains using this scheme and (b)We were able to further reduce the nucleation density.

# 4.0 DEVICE FABRICATION

After the growth of the films as described in Chapter 3, a variety of steps had to be undertaken to fabricate suspended devices using these films. These steps are described in the following sections.

## 4.1 FILM TRANSFER

Either of the film, after growth, required to be transferred from the substrates over which it was grown onto another substrate, either before or after device patterning. The technique used for such transfers was similar for both aluminum oxide and graphene, as described below:

- The film was spin-coated with a 2-3 $\mu$m thick layer of photoresist or 270 $\pm$ 10 nm thick layer of Poly (methyl methacrylate) (PMMA) (in anisole solvent) to aid in the transfer of the film later.
- The aluminum or copper disc was then put on a vacuum chuck, coated face down, on the diamond turning machine, and the disc was thinned down to $\sim$ 50-100$\mu$m.
- The rest of the aluminum was then etched away in a 20:10:5:2 $H_2O$ + HCl (36.5 - 38%) + (1M) $CuSO_4$ + $H_2O_2$ (30%)solution; the rest of the copper was etched off in a saturated Ferric Chloride ($FeCl_3$) or 1 M Ammonium persulfate (APS) solution.
- The left-over coated film was then transferred from the etching solution into water, to clean away any remaining reaction products, and it was then transferred onto the desired substrates, with the photoresist/PMMA side up.
- The sample was left to dry overnight, after which the photoresist/PMMA is removed with acetone/oxygen plasma cleaning.

## 4.2 LITHOGRAPHY AND ETCHING

We processed both graphene and aluminum oxide films in our lab making devices ranging from 0.5$\mu$m to 20$\mu$m in one direction and 5$\mu$m to 8$\mu$m in the other direction. Lithography

and etching was used to define these devices on the films. We performed photolithography (PLT) on our samples for this purpose, the details of which is given in Appendix B.

### 4.2.1 Failed and dropped attempts

1. We started by making these devices photo lithographically, and using wet chemical etching steps to etch away the metal under and around them.

   **Disadvantages:** This process gave us quite a few problems such as: the device edges were either contaminated with etchants, or were never straight; the devices had deposits on them, presumably reaction products of the chemical etching steps; the yield rate was very low etc.

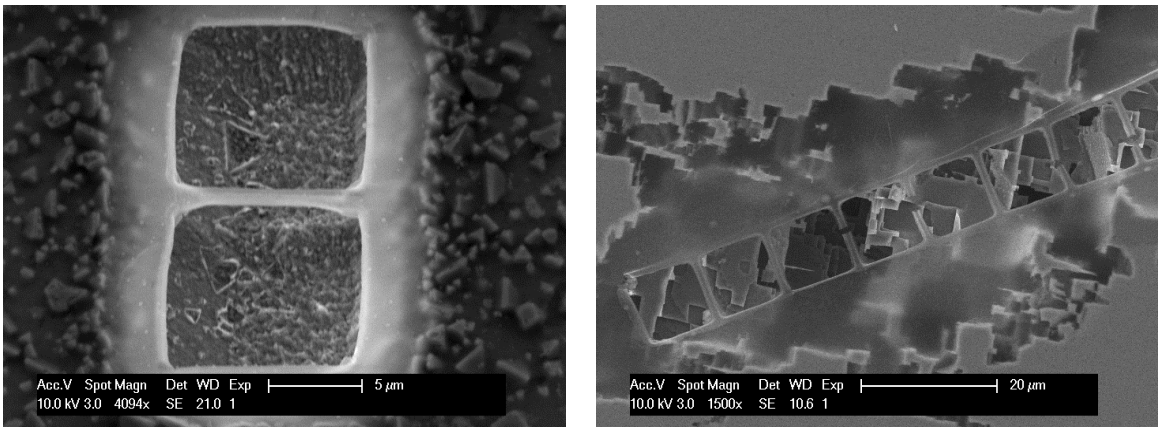


Figure 14: Devices made with photo lithograhy and wet chemical etching (a)Graphene devices after chemical etching steps and (b)Aluminum Oxide devices after chemical etching steps

2. Another method that was tried was to transfer the films, without patterning, onto the pre-processed grooved substrates and then pattern devices on these films using a **Focused Ion Beam (FIB)**.

   **Disadvantages:** Using FIB to fabricate devices posed quite a few disadvantages: ion beam is known to damage and cause defects in graphene; it gave a yield of about 1 usable device in an hour; It was expensive, as were using the FIB in the Nanoscale Fabrication

and Characterization Facility (NFCF), which costed us $55/hour etc.

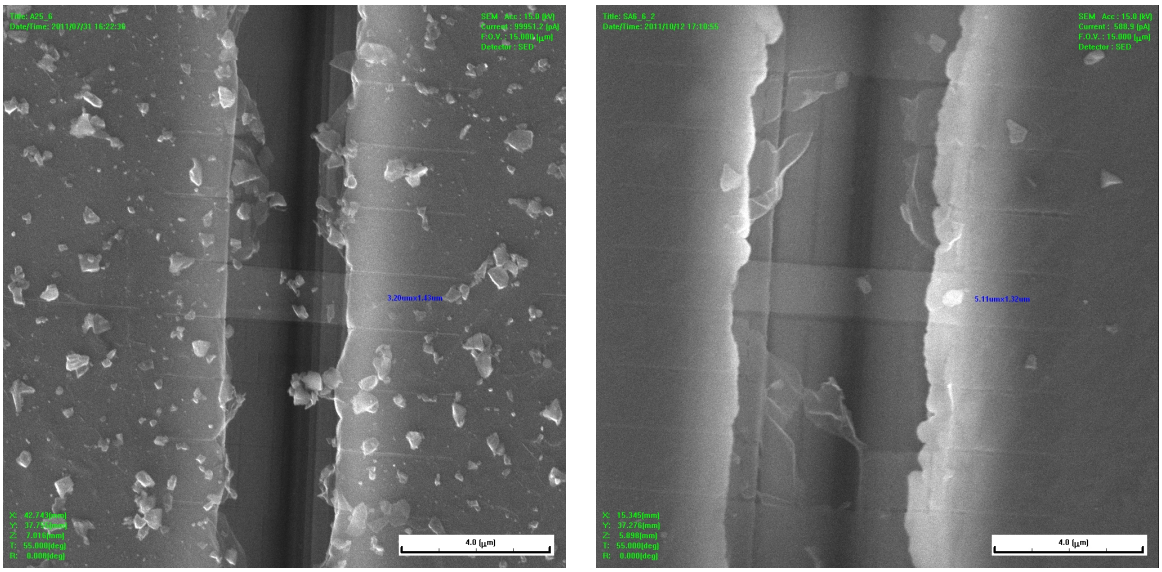

Figure 15: Devices made with transfer and FIBing of films: (a)Graphene and (b)Aluminum Oxide

3. We tried making these devices lithographically on one substrate, and then transferring them to another pre-processed grooved substrate, to avoid any etching steps. The lithography of devices for this method was done in form of spiral, to maximize the yield rate of devices. This was our longest-standing method. Following are the failures (the reasons for failure are also listed) we went through, before landing on our present procedure:
   - Patterning devices in a spiral fashion and contacting a general area of the film (see Chapter 6 meant that if one part of the spiral got broken even at one point, it rendered devices on the whole spiral useless.
   - We tried patterning devices on graphene with photo-lithography, using a negative photo-resist as a mask before transfer. That method did not work well, because photo-resist was leaving a lot of residue on graphene.
   - We then tried spinning Poly (methyl methacrylate) (PMMA) on graphene, followed by photo-resist, to prevent direct contact between photo-resist and graphene. We found that with this method the photo-resist and PMMA solvents were mixing with

each other and causing additional residue problems.

- We then tried using an **Intermediate Layer** between PMMA and photo-resist to prevent this mixing of solvents, patterning the photo-resist and then taking this pattern into graphene through all the layers.
  - The first such intermediate layer we tried was sputtered Chromium (Cr). Due to difference in thermal expansions of all the layers, Cr cracked after baking photo-resist during photo-lithography.
  - Another such layer that we tried was sputtered graphite. This went a little further ahead than Cr, and we were able to transfer patterns into graphene and transfer it onto our substrates. On a little further investigation, we realized that our transferred graphene film was covered with a very thin and robust conductive film of some sort. We suspect, though we did not analyze this carefully, that this was a diamond-like carbon film, which got left after etching away the graphite, and we could not find a way to get rid of this.
  - We then tried sputtering titanium (Ti) as the intermediate layer. This we thought worked well for us for a while, before we realized that Ti etching with dilute hydrofloric acid (HF) or buffered HF (BHF) was a very uncontrollable process and left some Ti in undesired spots, which left graphene in between the devices un-etched. Because of this getting crisp-edged devices became a somewhat chance process.
  - Our last try in this series was sputtering copper (Cu) onto as this intermediate layer. We suspect that our sputtered Cu was porous, due to lack of enough energy in the sputtering process. Due to this porosity the solvent in the photo-resist got mixed up with PMMA and ended up cracking the Cu layer.
- Somewhere in between all the above we also tried replacing PMMA with polycarbonate (PC), directly followed by photo-resist, as graphene transfers with PC are known to leave almost no residue [105]. This did not work for us as photo-resist spinning on PC de-laminated PC. We suspect this was happening due to the intermixing of the photo-resist solvent with PC.
- We also tried sputtering Ti directly on graphene followed by photo-resist. Our idea was doing transfers with Ti, and leaving some Ti on graphene to act as contact pads

for making electrical connections to graphene. This again did not work due to stress in the sputtered Ti film, and during transfers graphene ended curling and bunching up around any Ti left on the film.

Some of the devices obtained with these methods are shown below:

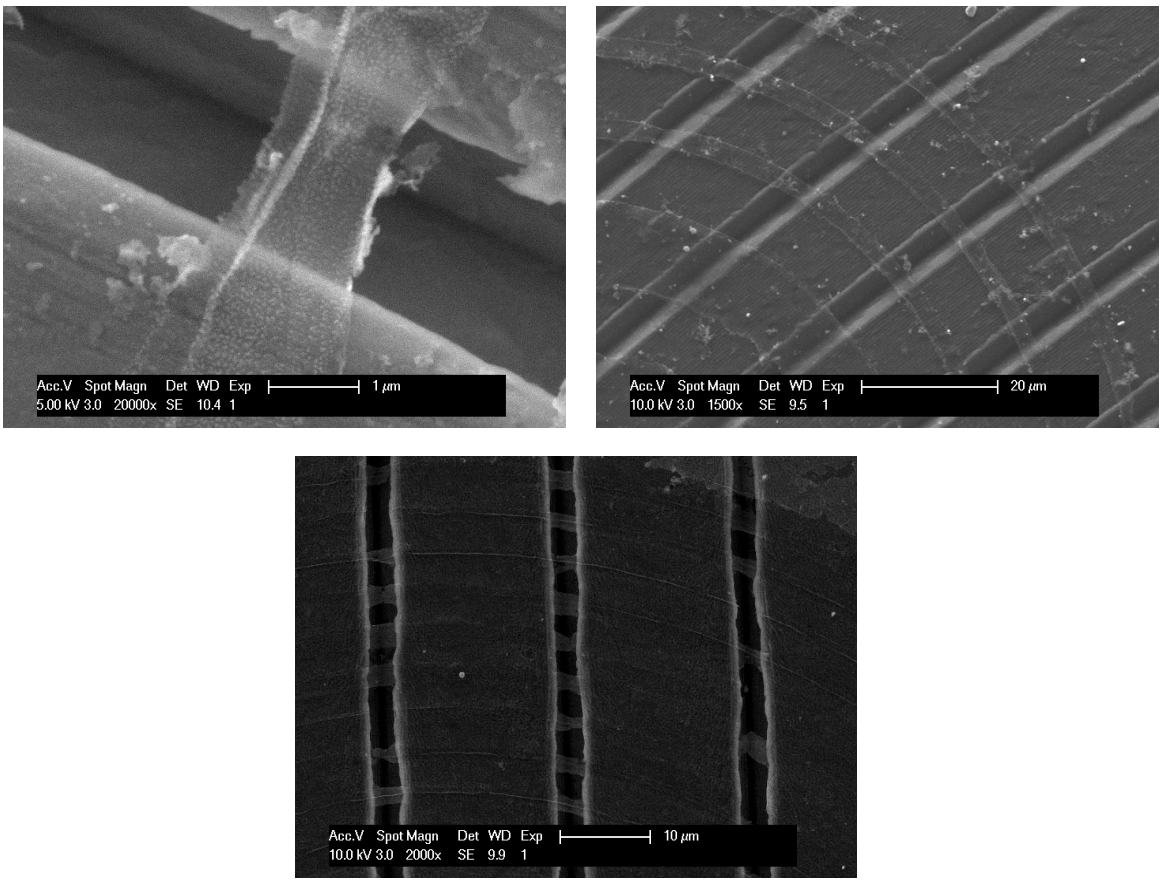


Figure 16: Devices made with photo lithograhy and transfer onto other pre-processed substrates (these devices are not all from the same sample) (a)A single graphene device made using this method, (b)A few such graphene devices and (c)One half of a spiral of graphene devices fabricated using the transfer method

After all these failures, we came upon a very simple and elegant method to pattern devices onto graphene, as explained below. This is what we used till the end of my time in the lab.

### 4.2.2 Deep UV Lithography of PMMA and Oxygen plasma etching of graphene

After coating graphene with nano-diamonds, it is spin-coated with PMMA. Deep-UV light (irradiance peaks at 240-310nm) and home-made Ti lithography masks are used to define patterns on PMMA [106]. With this method we have been able to pattern devices of different shapes: doubly clamped beams (bridges), circular drums and rectangular drums. Depending on device geometry, the processes of development and wet transfer onto grooved substrates vary, as outlined below. This method was mostly developed and handled by Jen-Feng Hsu, and more details can be found in his future thesis [58].

**Bridges**

- PMMA on top of graphene on copper is exposed to deep-UV through a mask with arrays of bridges of varying widths (0.5$\mu$m to 4$\mu$m).
- The PMMA is developed by dunking the sample in 70% iso-propanol (IPA)/water mixture, in which the exposed areas get dissolved away.
- Graphene in areas where PMMA has been removed is etched off using oxygen plasma cleaning.
- Then the whole piece is exposed to deep-UV light to soften the PMMA to promote adhesion of PMMA/graphene film to the substrate.
- The copper is then etched away in a saturated Ferric Chloride ($FeCl_3$) or 1 M Ammonium persulfate (APS) solution.
- The left-over graphene + PMMA film is then transferred from the etching solution into water, to clean away any remaining reaction products, and it is then transferred onto the above-mentioned grooved substrates, with the PMMA side up.
- The transferred sample is kept under vacuum to dry off any remaining water.
- The PMMA is then removed off the substrate with acetone, and the substrate is dried off with Critical Point Drying (CPD) to release the film over the grooves.

**Circular and Rectangular Drums**

Drums, being held down on all sides, are reported to give higher Q devices [61]. With our present method of patterning devices, we have successfully patterned graphene with Circular and Rectangular Drums, with PMMA supporting structure around them.

- The copper behind graphene is etched away in a saturated Ferric Chloride ($FeCl_3$) or 1 M APS solution.
- The left-over graphene + PMMA film is then transferred from the etching solution into water, to clean away any remaining reaction products, and it is then transferred onto the above-mentioned grooved substrates, with the PMMA side up.
- Transferred sample is kept under vacuum to dry off any remaining water.
- PMMA on top of graphene is exposed to deep-UV through a mask with arrays of circular or rectangular drums with dimensions varying between 2$\mu$m to 10$\mu$m.
- The exposed PMMA is dissolved by dunking the substrate in 90% IPA/water mixture.
- The substrate is then put into pure IPA to stop the development process and is then transferred into hexamethyldisilazane (HMDS). Due to the low surface tension of HMDS, the substrate is then pulled right out of HMDS, without any CPD and blown dry.

An SEM image of a bridge Fig. 17(a) and a circular drum device Fig. 17(b), fabricated with our latest techniques is shown.

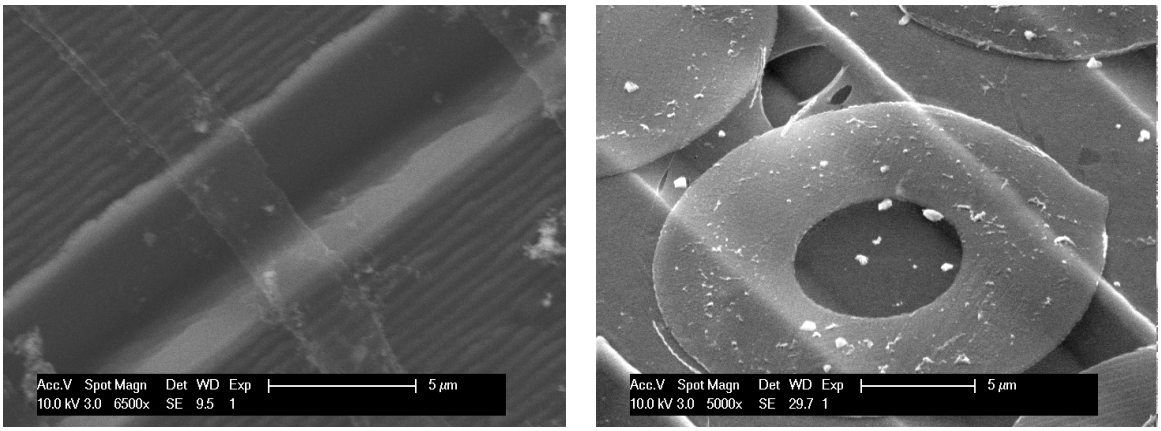


Figure 17: Devices made with deep UV lithography of PMMA and oxygen plasma etching of graphene: (a)Doubly-clamped beam and (b)Circular Drum with PMMA as the support material

## 4.3 NANODIAMOND DEPOSITION

### 4.3.1 Spin on before growth

This was our first attempt to deposit nanodiamonds on our samples, and this was a method that students in Dr. Gurudev Dutt's lab used. For this method we started with a solution that had a density of 100 carats/kg ($\approx$ 20 g/l) of nanodiamonds in the size range of 0-50 nm. We diluted this solution to a quarter of its original density, and then centrifuged it at 10,000 rpm a few times, discarding the bottom sediment at every step, to collect the smallest possible nanodimaonds. We then spun on this solution on our above-mentioned copper substrates, before the growth of graphene.

### 4.3.2 Electrophoretic Deposition

Because the above method involved a lot of steps, and had to be done in someone else's lab, we instead started using electrophoresis [107] for depositing the nanodiamonds onto our devices. For this purpose, we built a setup using some guidelines mentioned in the above reference. This electrophoretic deposition (EPD) of the nanodiamonds was done on graphene after growth on copper. I designed and built a custom fixture for the purpose of performing EPD on our graphene samples. Some specifications of this fixture was decided on the basis of the above-mentioned reference, such as distance between the electrodes. A picture of the top and front view of the EPD fixture is shown in the figure below.

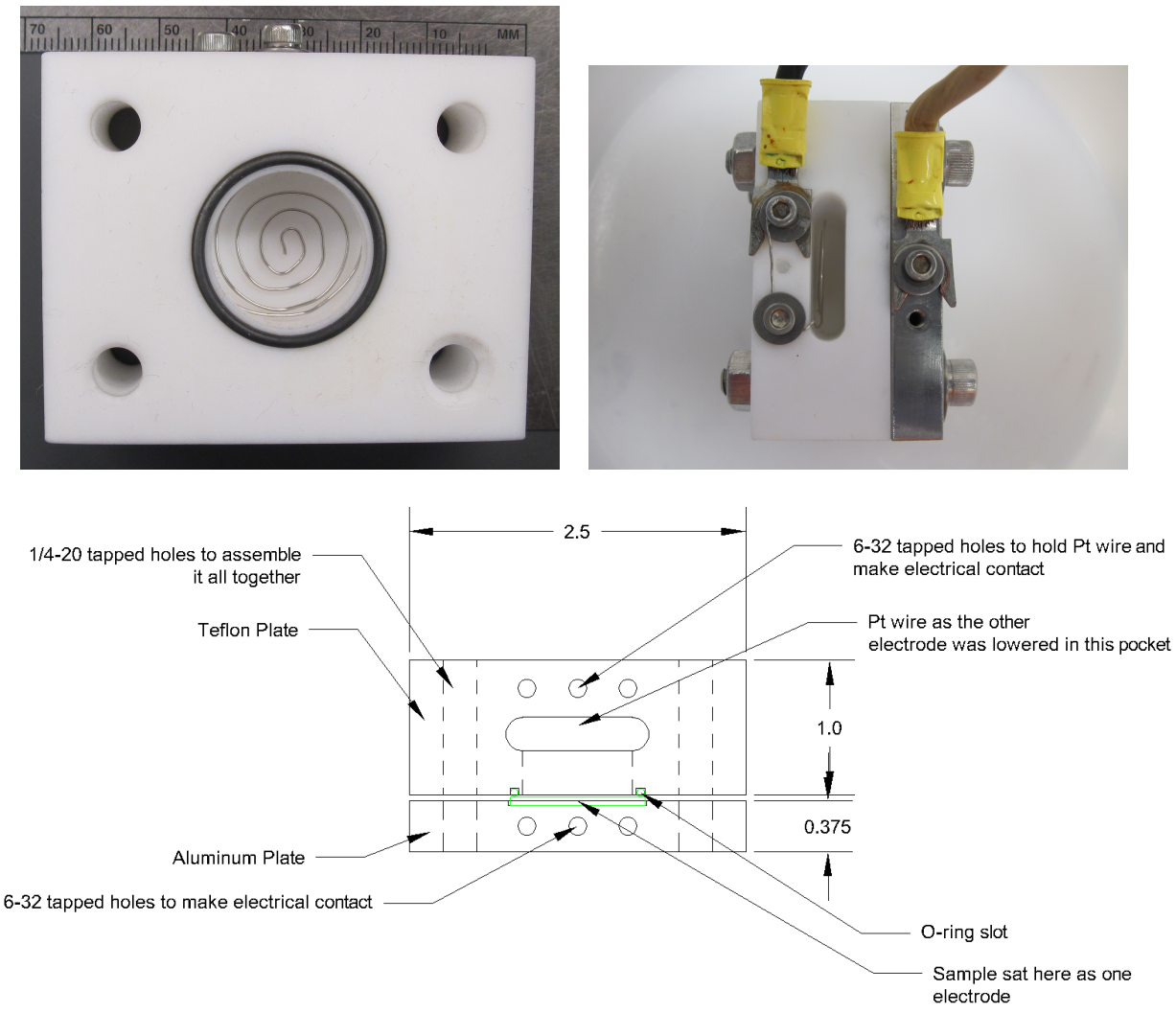


Figure 18: Pictures and Design of the home-made fixture built for the EPD of nanodiamonds on our graphene samples (a)Front View of the inside of the electrophoresis cell, (b)Top View of the whole fixture and (c)Top View of the assembly drawing of the EPD fixture.

As can be seen in these pictures, one piece of the fixture was made out of teflon, and the other was made out of aluminum. The whole fixture was meant to be standing vertical. The sample on which the nanodiamonds were to be deposited was made to be one of the electrodes. It was kept in place by the aluminum plate and pressed against an O-ring, to make the electrophoresis cell liquid-tight. The front of the sample was placed facing the other electrode, which was a home-made spiral made out of a platinum wire (Surepure Chemicals

Inc., 99.95% pure, 0.020" diameter, annealed temper). The cell between the two electrodes was filled with a dilute solution (anywhere between 0.1-5 mg/L) of nanodiamonds (diluted with DI water). Initially, using the above reference we started by making the sample as the cathode (negative electrode) and the platinum wire as the anode and applying a voltage of 10 V for 3 min between the two. But over time, we experimented with voltages between 1-10 V, being applied for 30 sec-3 min and making the sample either negative of positive electrodes. All these variations gave me a good deposition of nanodiamonds on our sample, the density of which would increase on increasing the voltage and the time of charge transfer.

This method of nanodiamond deposition was successfully tried for depositing on specific areas of the sample patterned using photolithography.

### 4.3.3 Dip after growth

Due to the fact that the EPD of nanodiamonds was a long process with multiple steps, we tried another simpler method: After graphene growth on the copper disc, we sat this disc, graphene face up, in a nanodiamond solution (5-500 mg/L) for a few minutes ($\sim$5 min), flushed the solution out a few times with ethanol and then dried the sample using Critical Point Drying (CPD). The purpose of flushing the solution with ethanol was to switch to a liquid with less surface tension than water to prevent tearing of the graphene film. This was further accomplished by performing CPD, during which ethanol was replaced with liquid $CO_2$, and then the sample was dried above the critical point of $CO_2$. This way we ensured that graphene was subjected to minimum surface tension, thus decreasing its chances of tearing up.

Various variations of this method were tried over the years:

- This method was tried without CPD, and letting ethanol dry on the surface of graphene in air.
- Another variation was to swap the nanodiamond solution with water, then swap it with ethanol, and then blow drying it.
- Another variation was to swap the nanodiamond solution with water, then swap it with ethanol, and then blow drying it.

- To reduce the surface tension even further, we tried swapping the ethanol solution with HMDS, and then letting the sample dry in air.
- After realizing that decreasing the surface tension and performing CPD was not really helping with too much - we tried dipping the sample into the nanodiamond solution and taking it directly out of it and letting it dry in air.

This was our longest-standing method, and was used, with or without CPD, for about 2-3 years!

### 4.3.4 Drop-coat

The last variation to the above method led us to put a drop of the diluted (with water) nanodiamond solution onto the desired area of our sample, and let it dry in air. This was done to achieve higher density of nanodiamonds over our samples.

This was done by putting a drop of high concentration (100-500 mg/L) nanodiamonds (250-500 nm/100 nm diameter) solution on the sample and letting it sit for 5-10 minutes. This drop was then either blow dried off (if large area coverage was required), or was left to dry in air (if a higher concentration was required in a small area).

In a variation of this method we tried diluting our nanodiamond solution (concentration of 500 mg/L) using isopropanol (IPA) instead of water. This was done to facilitate faster drying of the solution and leave less residue than water. We did not see much difference created by this variation.

## 4.4 FABRICATION OF SUBSTRATES

Nanoelectromenchanical systems (NEMS) are the basis of a lot of fields these days. Other than being used to study the electrical and the mechanical properties of materials, they are used in applications such as making electrical devices. Any NEMS system can be seen as composed of two elements: the material that is being studied and the substrate on which the material is being studied on. Though the substrate should not affect the properties of the

material being studied, but some properties of the substrate play a crucial role in studying the material, such as adhesiveness of the material on the substrate makes sure that energy dissipation in mechanical systems is solely dependent on the material.

We developed a design of a substrate onto which different thin films can be transferred and their properties can be studied electrically or optically. The proposed substrates can be made out of any metal, such as aluminum, copper or brass. The instruments required for making these substrates are: single-point diamond turning machine with diamond tools such as a big-radius tool for flattening out the substrate and a dead sharp tool for making flat-bottom grooves in the substrate; and a sputtering system with targets such as titanium, graphite and silicon or silica, and a provision for gases such as argon and oxygen.

These substrates were made out of oxygen-free electronic (OFE) grade ultra-pure (99.99%) copper. To make these substrates we started with ∼6 mm diameter, 1 ft long rod of OFE copper and cut out ∼2 mm thick discs, using conventional machining techniques. An 0-80 internal thread was tapped into the center of these substrates, for holding them onto the diamond-turning machine.

### 4.4.1 Diamond Turning

As mentioned in Section 3.1, we used the diamond-turning machine to flatten and put grooves on these copper discs. Initially, both faces of the copper discs were cut flat to an RMS roughness of ≈ 2 nm by SPDT, with a 1.5 mm radius single-crystal diamond tool. Diamond turning both faces of one such copper disc usually takes 30-45 minutes.

To get film suspension after transfer, we made circular grooves on these substrates, again using SPDT. These grooves were made using sharp-tip diamond tools, with an angle of 120° between the walls of the tools (we tried 60° and 90° tools too to get narrower and deeper grooves). A photograph of one such substrate getting grooved by SPDT is shown in the figure below. As can be seen in this picture, a second rounded tool is mounted to the right, likes of which are used for flattening these substrates.

These grooves were made with a flat patch at the bottom, for ease of device and film detection. These grooves were made with widths varying from 2-7 $\mu$m and depths varying

from ≈580 $nm$-1.46 $\mu$m, with the spacing between the grooves set nominally at 20 $\mu$m. An illustration of these grooves is shown in the figure below.

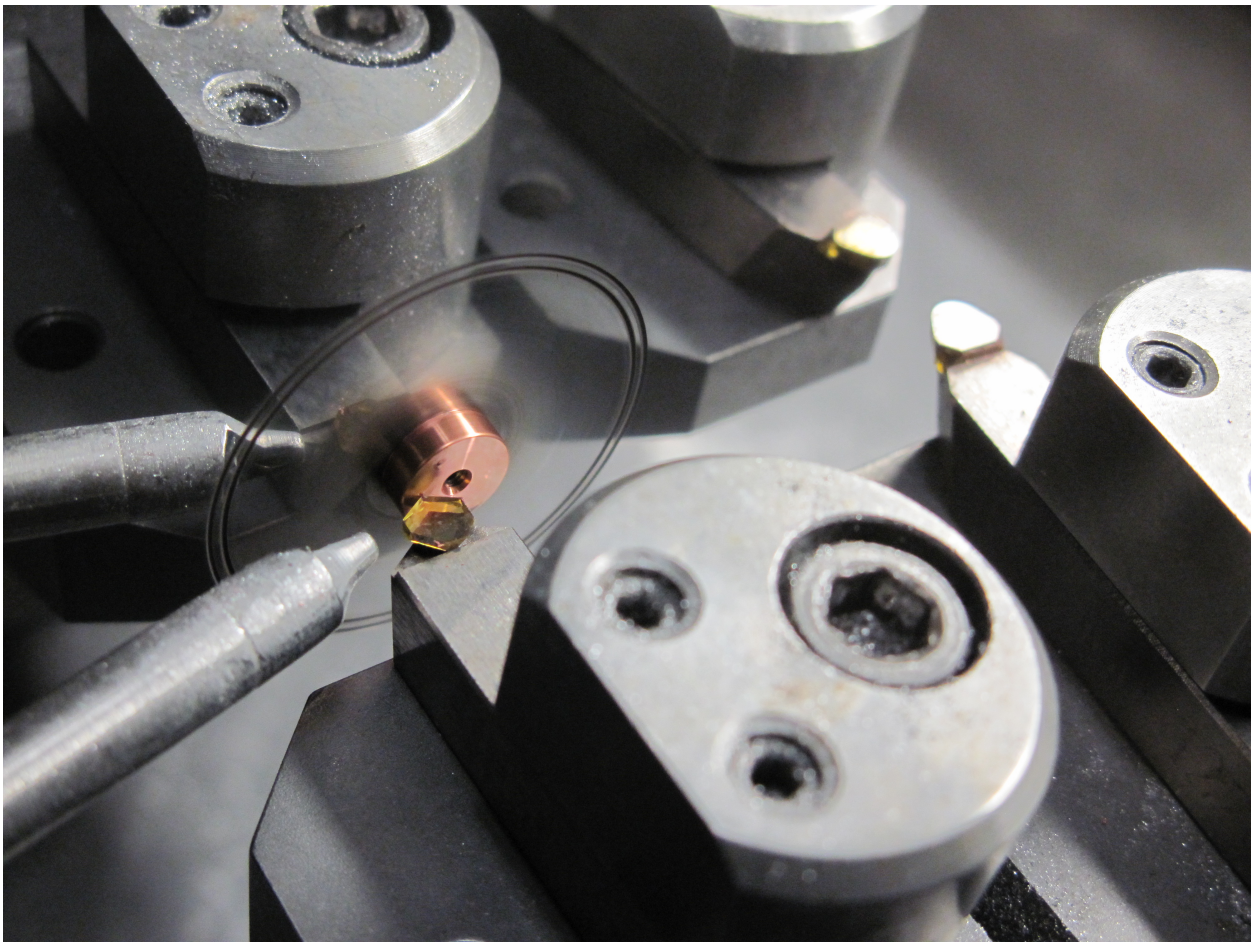

Figure 19: Photograph of a copper substrate being grooved by SPDT on the diamond-turning machine, to be used for device suspension.

### 4.4.2 Deposition - AR coating

For optical detection of films after transfer onto these substrates, we made an anti-reflective (AR) coating on the substrates by sputtering multiple films onto them. After cutting grooves these substrates were stored, if needed, in a vacuum bell-jar. Before AR coating them, they were cleaned with acetic acid, followed by acetone and IPA, to prevent any oxidation of the

surface.

For the AR coating, we started with a 50 nm thick titanium (Ti) layer.[1] The purpose of the Ti layer was to enhance the adhesion of the subsequent layers to the metal underneath. Thereafter, a ∼500 nm thick absorptive layer of Ti doped diamond-like carbon (DLC) was sputtered. This layer helped in cutting down the broadband reflections to ∼ 10%. Both these bottom layers could be somewhat conductive, due to the presence of Ti. We then sputtered an insulating thick DLC layer. The thickness of this DLC layer was tuned to minimize reflections in red (∼ 637 nm). This optimization occurred at a DLC thickness of ∼ 60 nm. After these layers, a final silica ($SiO_2$) layer was sputtered onto these substrates. This $SiO_2$ layer provides a hydrophilic surface onto which thin films, such as graphene, are known to adhere very well. $SiO_2$ was sputtered by reactive sputtering of silicon in oxygen, and before and during the sputtering the sample was heated to 600°C, to minimize the porosity of the sputtered silica film. The thickness of silica was also tuned to minimize the reflectivity in the red part (∼ 637 nm) of the visible spectrum to $< 1\%$, which was achieved ∼ 300 nm. This is done to get maximum visibility of the later-transferred films with a red laser. The following table mentions the sputtering parameters for every film.

| Layer name | Chamber P (mTorr) | Ar flow (sccm) | $CH_4$ flow (sccm) | $O_2$ flow (sccm) | Sample ht (au) | Deposition power (W) | Deposition time (min) |
|---|---|---|---|---|---|---|---|
| Sample bias | 25 | 20 | - | - | 95 | 15 | 10 |
| Ti | 25 | 20 | - | - | 95 | 150 | 10 |
| Ti doped DLC | 25 | 19.2 | 0.8 | - | 95 | 150 | 90 |
| Ti + DLC | 25 | 19.2 | 0.8 | - | 95 | 150 → 5<br>30 → 150 | 5 |
| DLC | 25 | 15 | 5 | - | 95 | 150 | 4 |
| $SiO_2$[2] | 25 | 20 | - | 4[3] | 100 | 150 | 35 |

Table 5: Experimental parameters for sputtering of various films on the substrates

[1] we used Dr. Choyke's Dektak and our monochrometer to measure the thicknesses of the sputtered films.
[2] The gun was moved closer to the sample - 2.3" flange-to-flange
[3] We always turn $N_2$ on while we're flowing $O_2$

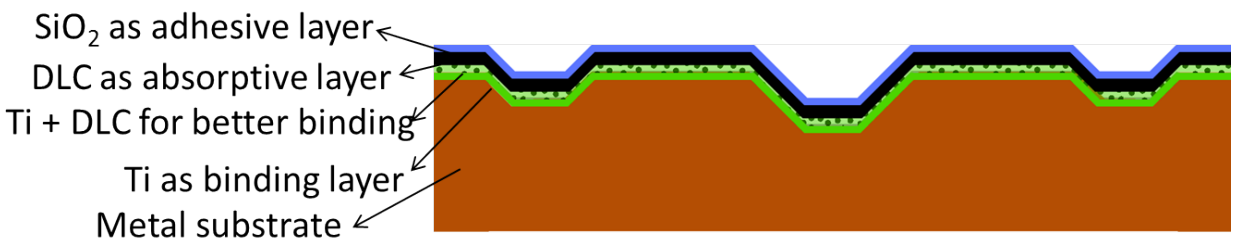


(a)

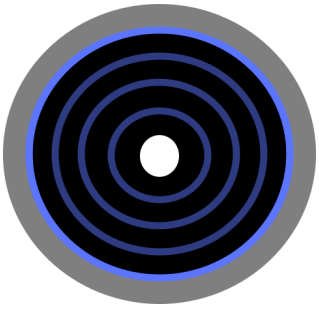

(b)

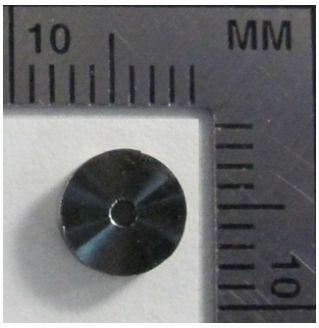


(c)

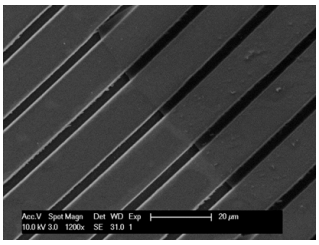

(d)

Figure 20: Grooved and AR coated substrates used for device suspension (a)Side-view illustration of the finished grooved substrates, (b)Top-view illustration of the finished grooved substrates, (c)A camera-clicked picture of the finished substrate and (d)A zoomed-in SEM image of the same.

The figure above shows an illustration of the finished grooved substrates from the side and from the top. The figure also has a camera-clicked picture of the finished grooved substrate, and a zoomed-in SEM image of the same, with a thin-film transferred over it.

To analyze the AR coatings theoretically, an undergraduate student (Harry Gilliland) developed a model based on Fresnel Law, as described here [108]. This model was able to take the thicknesses and refractive indices of the various coatings as variable. We tried to measure the thickness of each coating experimentally using a Dektak in Dr. Choyke's lab. We also tried to measure broadband reflectivities of these substrates using a monochrometer. As both of the experimental measurement tools used were a bit flaky, an iterative process was setup between the theoretical model and the experimental scheme.

Using the theoretical modeling, we could see that the DLC and $SiO_2$ layers together enhanced the contrast of graphene on our substrates. Even without the DLC layer, the contrast of graphene on our substrates was better by over a factor of 5 than reported [108] with the other commonly used substrates. This improvement was due to the absorptive layer (Ti-doped DLC) below the $SiO_2$. This difference in contrast between the substrates presented here and the ones reported in the past is shown in Fig. 21(a) and Fig. 21(b) respectively. As can be seen in these theoretical curves, the contrast achieved with graphene with the Blake et. al. substrates is much more broadband than achieved with our substrates. In other words, our substrates increase the contrast of graphene at the cost of bandwidth of wavelengths. With the DLC layer underlying the $SiO_2$ layer, the problem can be thought of as two coupled harmonic oscillators. It is then possible to tweak the thicknesses of each of the layer to control the wavelengths at which the maximum contrast happens and the width and height of the maximum contrast peak. The figure below gives a comparison of the graphene contrast on our substrates, with and without DLC, and with the Blake et. al. substrates.

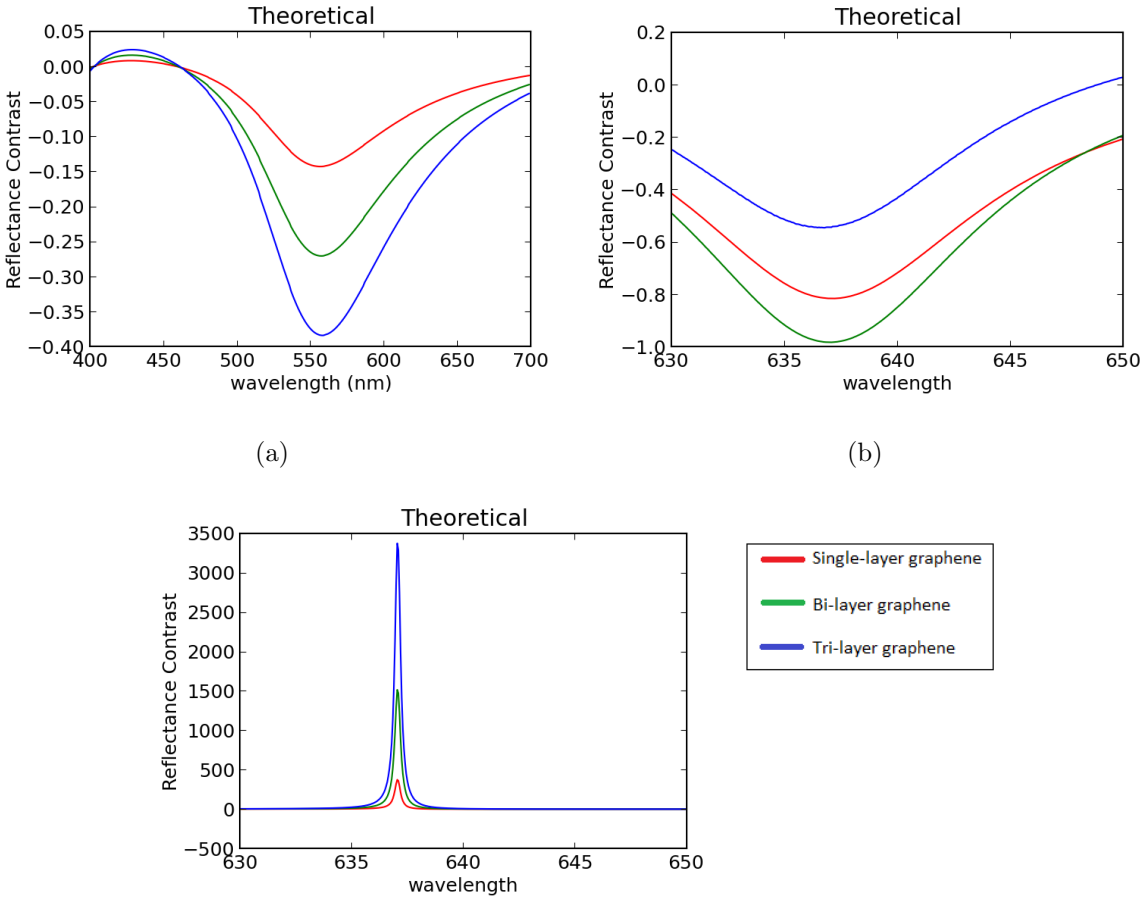


Figure 21: Theoretical comparison of contrast of graphene on different substrates. (a)Contrast on 280 nm thermal silica grown over silicon, as reported [108].(b)Contrast on $\sim$ 325 nm silica sputtered over Ti-doped DLC on our substrates.(c)Contrast on $\sim$ 312 nm silica sputtered over $\sim$ 60 nm DLC over Ti-doped DLC on our substrates.

These substrates are great for transfer and detection of thin films. The top silica layer is sputtered with heat and by putting the target very close to the sample, to ensure non-porosity in these films. This non-porous film can shown to be great for adhesion of thin films, such as graphene and aluminum oxide. The flat-bottoms of the grooves on these substrates help with interferometric detection of the transferred thin films.

# 5.0 CRYOSTAT

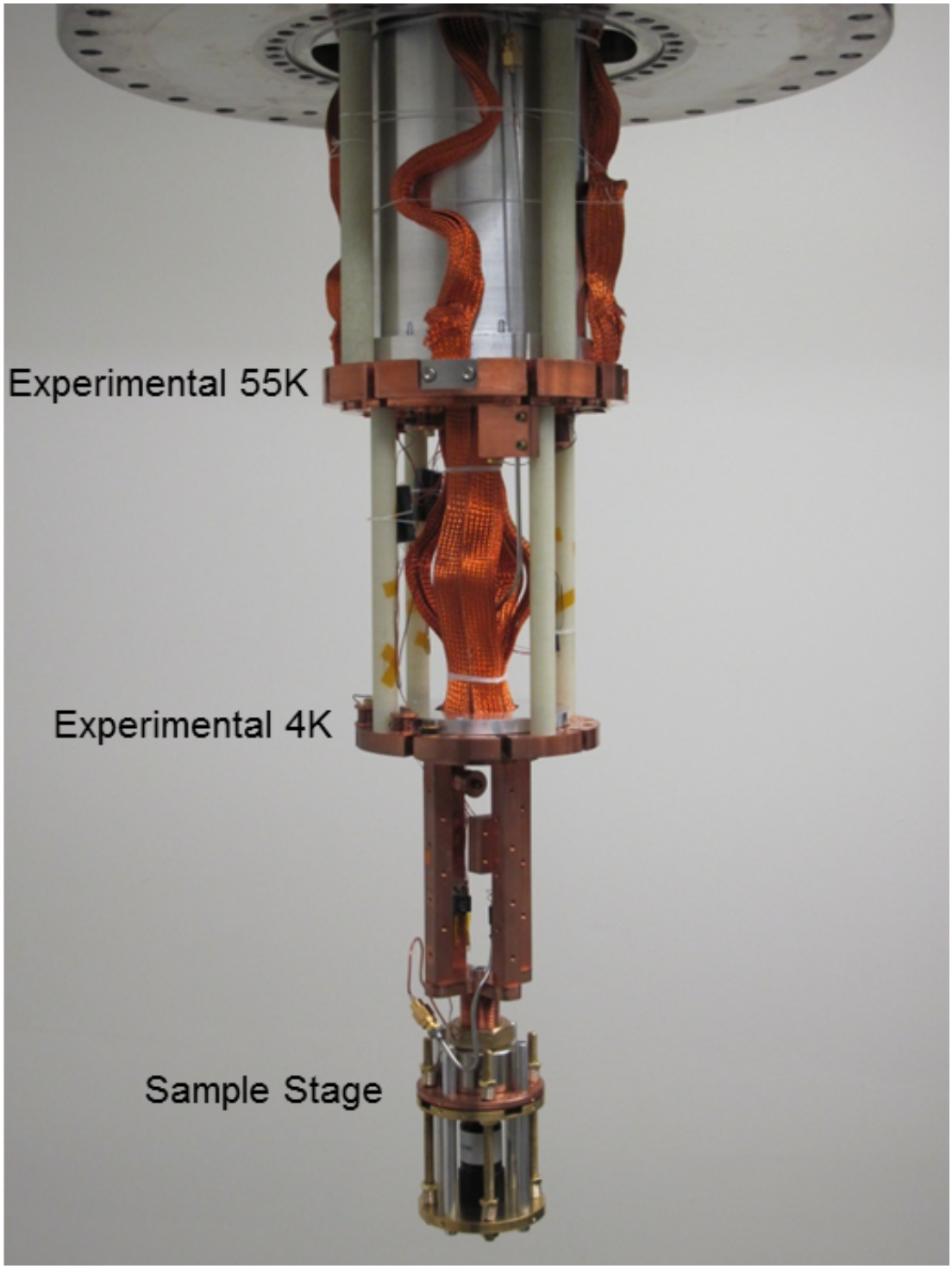


Figure 22: A picture of the internal parts of our Cryostat.

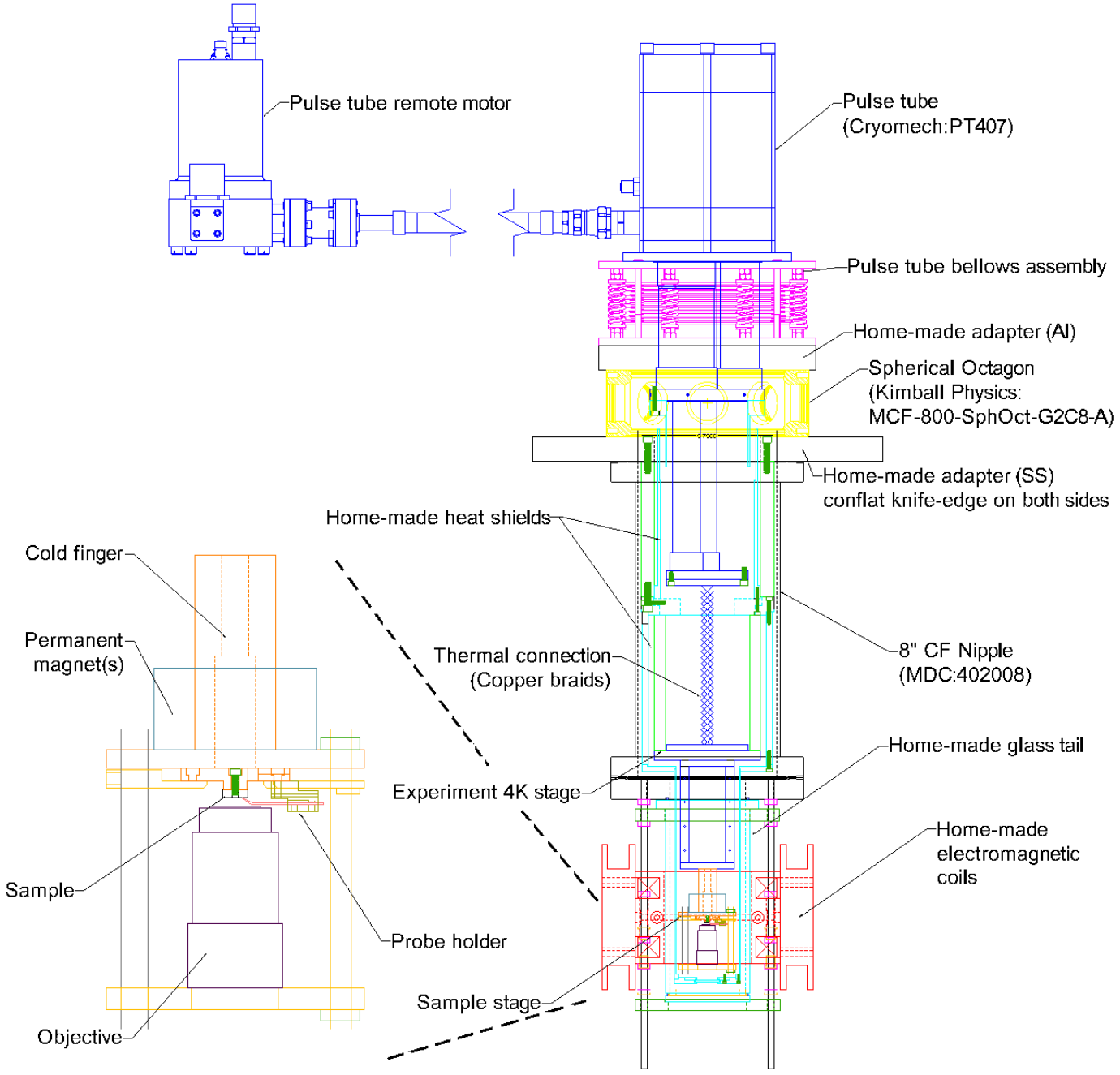


Figure 23: Schematic of our Cryostat - Outer and inner layers, with a blown-up layout of the sample stage on the left.

The first 1.5 years of my time in the D'UrsoLab was spent in designing and assembling the internals of the cryostat. Each part of it was carefully optimized for the required application,

making almost the whole cryostat user-customizable. Few such individual parts are discussed in detail below.

## 5.1 PULSE TUBE

The cryostat utilizes a Cryomech PT407 Pulse Tube Cryorefrigerator(with remote motor option and bellows assembly), which can go down to 2.8K without any load. The cooling capacity of the first stage of the refrigerator is 22W @ 55K, and 0.7W @ 4.2K for the second stage. The cryostat is designed, with most of the parts being home-made, around the pulse tube, to put our samples in vacuum with minimum heat load.

## 5.2 INTERNAL PARTS AND EXTERNAL BODY

Internally, it is divided into two (ready-made) + two (home-made) stages and three layers. The two ready-made stages are that of the pulse tube, as described above. The two home-made stages are experimentally usable 55K and 4K stages, thermally connected to the pulse tube stages, and thermally insulated from each other. The thermal contact between the pulse tube stages and the experimental stages was made using flat copper braids (AlphaWire: 95036). These braids can be seen in Fig. 22 - 4 sets of 6, 18" long braids were used for the 55K connection, and 6 sets of 5, 12" long braids were used for the 4K connection. Before making the connections, these braids were annealed in the tube furnace (at 700°C with 20 sccm of $H_2$ for 2 hours; I had annealed the first set at 1000°C, but they came out quite badly stuck to each other, and got severely bent while trying to pull them apart) to make them softer and remove any extra oxygen for better thermal contact. The lower of these two stages is in thermal contact with the sample stage. All these stages and their thermal connections are made with oxygen-free copper.

Outside all this internal structure of the cryostat there is a layer of aluminum heat shields, to minimize the heat load on to the cold stages from the environment. And the

outermost layer is of the vacuum-compatible parts to put the cryostat under high-vacuum ($\sim 2-3\times10^{-6}$ torr).

Our cryostat is hung from a ceiling i-beam and a hoist is used to lift or lower it. It sits on an extruded aluminum 80-20 structure, which is built inside a 18" $\times$ 18" hole in the optical table.

## 5.3 SAMPLE STAGE

As mentioned above, the experimental 4K stage is thermally connected to a home-made mechanical stage for the sample. As shown and labeled in Fig. 22, this stage has a few different parts. The thermal connection from the experimental 4K stage to the sample stage is made through the OFE copper cold-finger, which is part of the copper plate on which the sample plate slides. The sample plate, as shown in Fig. 22, is also made out of OFE Copper. This plate has a provision for the sample to get mounted on the requisite permanent magnet. In the past, this plate was also used to mount the sample on a piezo ring. The sample was mounted on the sample plate using non-magnetic titanium 0-80 screws (United Titanium, Inc.: 1-01-510-00.18, 1-01-510-00.25, 1-01-130-00.18). This sample plate also holds the probe holders, that are used to make electrical connections to the graphene film on the sample. This sample plate is sandwiched between the above-mentioned copper plate and a brass plate. This brass plate has threaded holes for 0-80 screws, which are used to slide the sample plate around.

Below this sandwich is a plate which holds the optical objective, used to focus the laser light on the sample. We tried the following different objectives for this purpose: Newport Reflective Objective 50102-02, 36X, 0.52NA (this was customized for our needs - see Fig. 60 in Appendix A); Olympus (Thorlabs: RMS20X) Plan Achromat Objective, 20X, 0.4NA; and Partec Quartz Objective 03-0202, 20X, 0.65NA (see Fig. 59 in Appendix A for some specifications). Out of these, the Olympus objective worked the best under room-temperature conditions, due to its achromatic nature. Under cryogenic conditions, the Partec objective was the only one we tried, because the quartz lenses in it were known to have no epoxy

between or around them, which reduced the risk of cracking under cryogenic temperatures. This objective, though worked well under cryogenic conditions, was hard to work with due to its chromatic and spherical aberrations.

The plate that holds the objective is connected to the sample-stage sandwich through four 6-32 threaded rods. Four 1/4" rods are also used at this spot to make this connection more sturdy.

## 5.4 ELECTRICAL CONNECTIONS

The sample inside the cryostat is connected to the outside world through a few electrical connections. These connections allow us to monitor the state and status of the sample.

To make most of these electrical connections, a twisted pair of teflon coated constantan wire (Omega Engineering: TFCI-005-100 FT.) was used. Each wire of the twisted pair was 5 mils ($\sim$ 125 $\mu$m) in diameter, with the insulation $\sim$ 3 mils thick. These wires were twisted using a Laboratory Stirrer, (Talboys: 107SC - was used in one of Elliot's old setup) which came with a mount and clamp.

All the wires for various electrical connections were fed into the cryostat using an electrical feedthrough flange (Kurt J. Lesker: IFTRG327013), a vacuum side connector (Kurt J. Lesker: FTACIR32V) and an air side connector (Kurt J. Lesker: FTACIR32AS). The above-mentioned electrical wires were soldered into the pins of both the above connector. These pins and wires were used to make the following connections:
Temperature Sensors - 4 - 4 wires each
Resistor Heater - 3 - 2 wires each
Magnetic field Sensor - 1 - 4 wires each
Detection Probe - 1 - 2 wires
Extra/Unused - 4 wires

For neatness these wires were wound around home-made copper bobbins, with the help of a varnish mentioned in Section 5.4.2, and attached to copper stages at various point

throughout the cryostat, with a bit of Apiezon N grease for better thermal contact. This grease was used for all parts such as temperature sensors, screws etc. that required a good thermal contact.

The functioning of the temperature sensors will be explained in Section 5.4.2, resistor heaters in Section 5.4.3, the magnetic field sensor will be explained in Section 5.5.3 and the detection probe will be explained in Section 6.1.1.

### 5.4.1 Coaxial Cable

As mentioned above, the sample plate has a provision for 2 probe holders, the probes in which are used to make electrical connection to the graphene devices on the sample. One of these probes is used for actuation of the devices, and the other one is used to detect the electrical signal getting to the graphene film. The purpose of these probes have been explained in Section 6.1.1.

The actuation probe of these two probes, is connected to the inner conductor of a copper coaxial (coax) cable (Microstock, Inc.: UT-47C; copper as outer conductor, 0.047" diameter, silver-plated copper as inner conductor), and the sample plate is connected to the outer conductor of this coaxial cable. This copper coax is then connected to a stainless steel coax (Coax Co., Ltd.: SC-219/50-SSS-SS; stainless steel as outer conductor, 2.19 mm diameter, silver-plated stainless steel as inner conductor http://www.coax.co.jp/page/display=cryogenic) that takes the electrical connection from the sample stage to the electrical feed-through flange, covering 2-3 feet in the process. This switch from copper to stainless steel is done to prevent any thermal shorting from the sample stage (@4K) to any room-temperature connections. The stainless steel coax was heat-sunk on the experimental 55K and 4K stages, using a heat-sink holder, the design of which is shown below. The final connection to the feed-through flange is then again made with a small copper coax piece, due to the flexibility of the copper coax over the stainless steel one. A similar coax was used for the application of microwave fields to the NV centers.

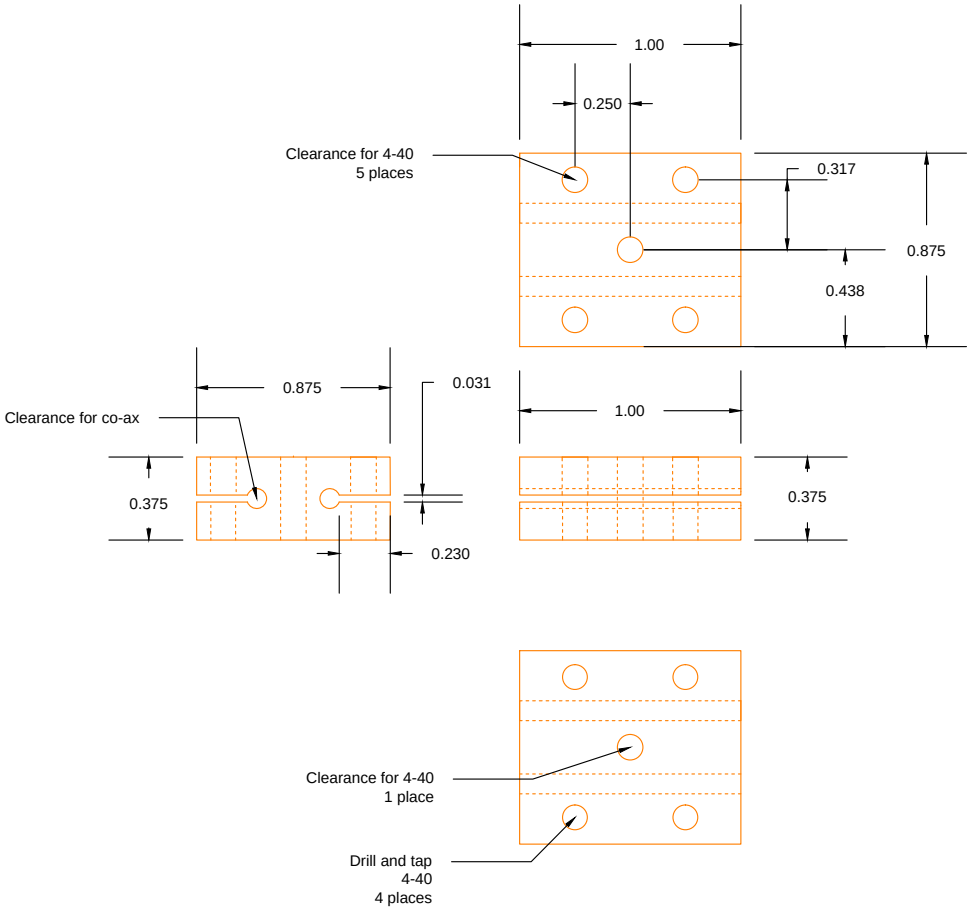


Figure 24: Design of the holder used to heat sink the stainless steel coaxial cable

One trick of the art that I would like to pass on is how to solder the coax connectors to the stainless steel coax. I tried a few different methods for this, such as using different kinds of solder flux and pastes. The easiest and the best way that I found to do this was to use 'No Clean' solder and the 'La-co N3 All Purpose Flux'.

### 5.4.2 Temperature Sensors

Four temperature sensors were connected at different points in the cryostat, to monitor the cooling and warming rate, and the equilibrium temperature, at these points. These four chosen points were: experimental 55K stage, pulse tube 4K stage, experimental 4K stage

and the sample stage.

The temperature sensors used for this purpose were Cernox (Zirconium oxy-nitride thin-film) [109] bought from Lakeshore: calibrated version - CX-1050-CU-1.4D (1.4K-100K) and uncalibrated version - CX-1050-CU. I then calibrated the uncalibrated ones using the calibrated sensor, and calibrated all 4 above 100K by extrapolation. We also bought a sensor monitor (Lakeshore: 218S) and adhesive/insulating varnish (Lakeshore: VGE-7031) for better thermal contact of the sensors.

A typically observed cooling curve of the system at the sample stage is shown in the figure. The lowest temperature recorded on the sample stage was 3.5K.

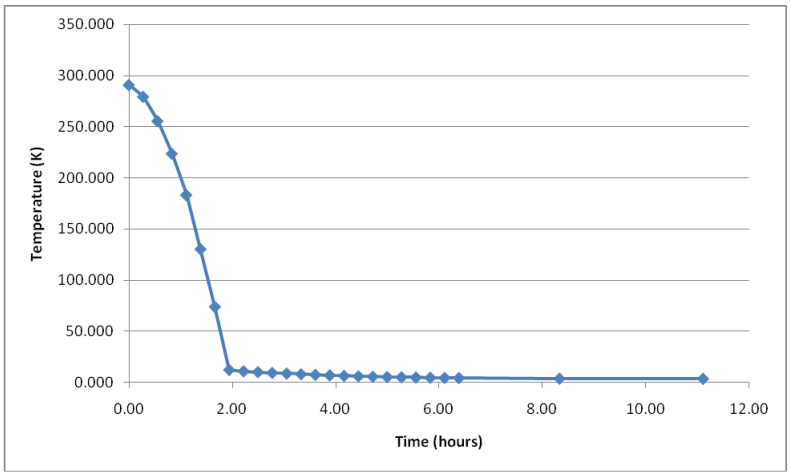


Figure 25: Cooling Curve of the sample region of the Cryostat

### 5.4.3 Heaters

As is, due to all the thermal load, the cryostat used to take a very long time to heat up to room temperature (24-48 hours!). To pace up the heating process, we put in three 1 kΩ, 35 W resistors inside the cryostat, one on the experiment 55 K stage plate, another on the experiment 4 K stage plate, and one close to the sample stage. The one close to the sample holder was screwed onto the side of a sorption pump plate (a plate with a lot of charcoal bits glued on, to act as an adsorbent), which was screwed onto the inside of the quad-pod area. These resistor heaters were powered in parallel through an Acopian power supply

(A150MT100), putting the whole 150 V from the power supply onto these resistors. The two heaters on the experimental stages were mainly used to heat up the cryostat and the one with the sorption pump was mostly used to get to better vacuum. Using these heaters led to a much faster heat-up of the cryostat - it now takes ∼5-6 hours to heat up the cryostat to room temperature.

## 5.5 MAGNETIC FIELDS

As explained in Chapter 2, coupling between the NMO and NV is achieved by applying an external magnetic field around the NMO. In our setup, we employed permanent magnets and Helmholtz coils for this purpose. The permanent magnets were used to achieve fixed magnetic fields and the Helmholtz coils were used to achieve a variation in the magnetic field, if and when needed. For experimental purposes, the Z-direction was defined as being perpendicular to the sample with the positive direction as vertically downwards. The plane of the sample was then taken to be in the XY plane, with the X and Y direction defined using a left-handed coordinate system (this happened by mistake, and discovered it much later - didn't want to change the notation on everything - maybe in the future, the vertically upwards direction can be labeled as +Z-direction). The specific magnets used and the configuration of the coils is described in detail below

### 5.5.1 Permanent magnet(s)

As mentioned in Chapter 2, ∼102-103 mT of magnetic field was needed around the NMO for maximum interaction with the NV centers. Because of the internal design of our cryostat, we wouldn't have been able to get this magnetic field in all three directions, except in the vertical (Z) direction. We thus used permanent magnets inside the cryostat around the sample to get us close to the targeted 103 mT in the Z-direction. In using permanent magnets to achieve this, alongside getting the right magnitude, another condition that we wanted to achieve was to get a somewhat flat field around the sample in the Z-direction. This was needed to

ensure that almost the same magnitude of $B_z$ was experienced at the surface of all samples, irrespective of their thickness.

[One major deciding criterion for the designs below was the off-the-shelf availability of specific sizes and shapes neodymium-iron-boron magnets. All our magnets for this purpose were bought from K & J Magnetics, Inc.]

**Design 1:** To satisfy both these conditions, the first design that we came up with, while we were still using piezos to drive the NMO, was to use:

1. Ring Magnet - 1.5" OD, 0.75" ID, 0.75" thick, in forward polarity, around the cold-finger
2. Ring Magnet - 1.25" OD, 0.75" ID, 0.25" thick, in reverse polarity, around the cold-finger, above (further away from the sample) the other big ring magnet mentioned above
3. Cylindrical Magnet - 0.3125" OD, 0.03125" thick, in forward polarity, inside the cold finger (very close to the sample surface)

Advantage: The magnetic field obtained was quite flat in the Z-direction, and on the sample surface.
Disadvantage: Sensitive to precise placement of the magnets, especially the cylindrical one inside the cold finger.

**Design 2:** This design was used to simplify the placement of the magnets, at the cost of flatness of the field in the Z-direction

1. Ring Magnet - 1.5" OD, 0.75" ID, 0.75" thick, in forward polarity, around the cold-finger ($-$Z-direction from the sample)
2. Ring Magnet - 1.5" OD, 0.85" ID, 0.75" thick, in forward polarity, around the objective (+Z-direction from the sample)

Advantage: Precise placement of the magnets was not required.
Disadvantage: The field was not very flat in the Z-direction and the net magnetic field was much higher ($\sim$170 mT) than the desired ($\sim$103 mT)field.

While using design 2 while looking for NV interactions with the NMO, we realized that the devices were moving around quite a lot while trying to modulate the magnetic field using the electromagnetic coils. We realized that this was happening due to the high magnetic moment of the large ring magnets was interacting with the external magnetic field from the

coils, thus torquing the internal guts of the cryostat and in-turn the sample. This led me to design 3, which was mostly based on getting close to the desired magnitude of the magnetic field, and not caring so much about the flatness of the field.

**Design 3:** This was the final design used in order to ensure the use of smallest possible magnets

1. Ring Magnet - 0.25" OD, 0.0625" ID, 0.0625" thick, in forward polarity, right behind the sample (in place of the old ring piezos)

Advantage: No torquing of the sample was seen.
Disadvantage: The field was not very flat in the Z-direction at the surface of the sample.

### 5.5.2 Electromagnetic coils

Electromagnetic coils were used on the outside of the cryostat. The development of the coils happened in a few stages, as outlined below. The pictures and designs for each stage are also shown:

**Z-direction coil** At the beginning, the cryostat had no provision for a variable external magnetic field, as seen in Fig 26(a). We then added Helmholtz coils for one direction, as shown in the designs below (This was done in December, 2010). The coils in this direction are quite close to Helmholtz configuration. I called these coils as the Z-direction coils, as the direction of the magnetic field produced by them is perpendicular to the surface of our samples.

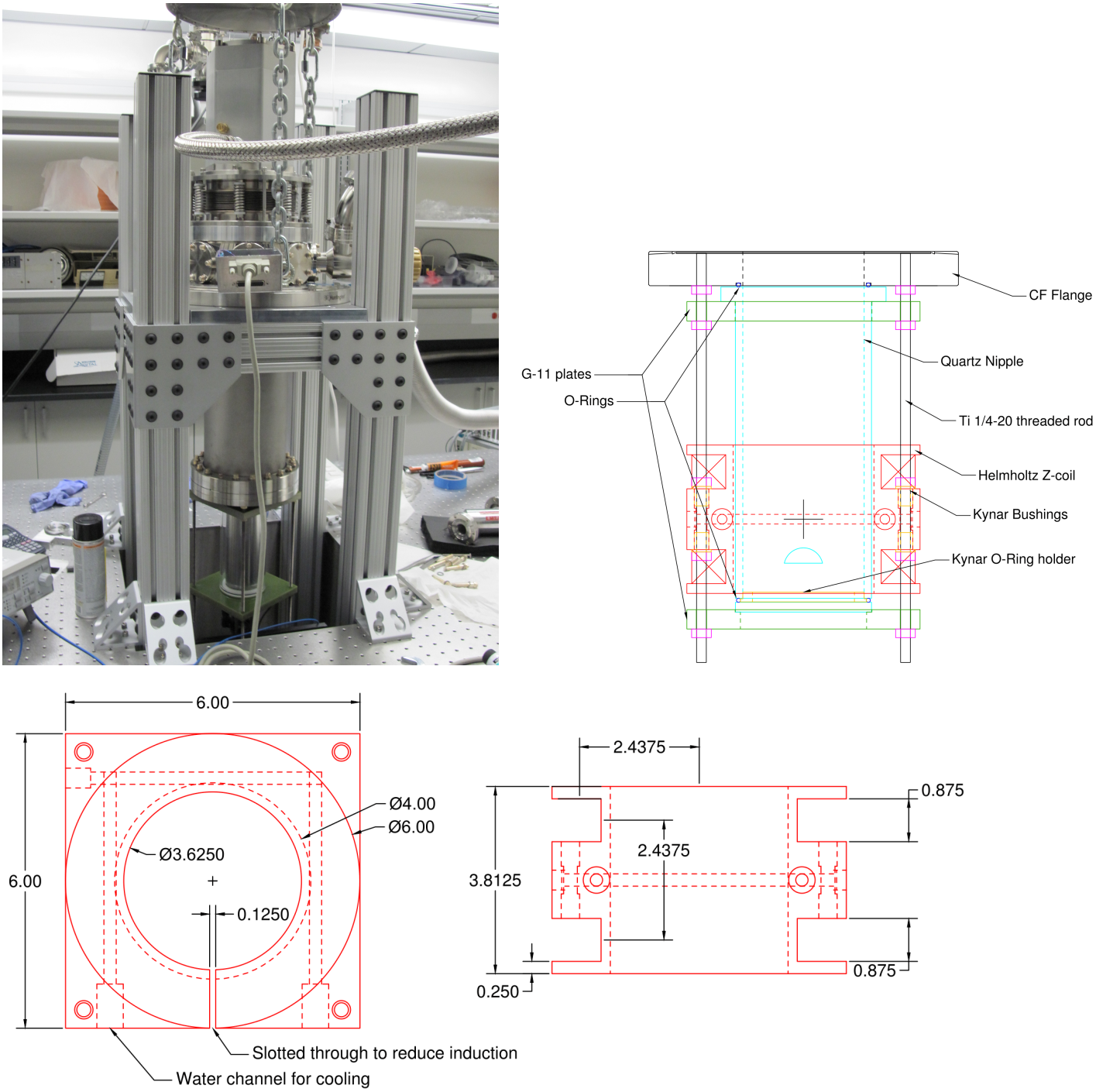


Figure 26: Development of Helmholtz coils in stages (a)Picture of the cryostat without any provision for varying the external magnetic field, (b)Design of the Z-direction Helmholtz coils added to the cryostat. and (c)Detailed design of the Z-direction Helmholtz coils

The physical dimensions of the Z-coils were decided on the basis of available physical space and easily available material sizes. As can be seen from Fig 26(c), these coils were machined to be in perfect Helmholtz configuration i.e. the two coils were separated by a distance equal to the radius of each coil, in this case $2\ ^{7}/_{16}$" . After the physical dimensions were finalized, following considerations went into winding copper wire on the Z-coils.

**Constants**

$$\rho = 16.9 \times 10^{-9} \Omega m \qquad \text{(Resistivity of copper)} \tag{5.1a}$$

$$\mu_0 = 4\pi \times 10^{-7} T.m/A \qquad \text{(Permeability of free space )} \tag{5.1b}$$

$$\text{"} = 0.0254 \qquad \text{(Conversion from inch to meters)} \tag{5.1c}$$

**Fixed Parameters**

$$A = 0.875\text{"} \times 0.875\text{"} \qquad \text{(Cross section area of each coil)} \tag{5.2a}$$

$$A_{eff} = A \times \frac{\pi}{4} \qquad \text{(Effective area due to packing of circles inside a square)} \tag{5.2b}$$

$$R = 2.4375\text{"} \qquad \text{(Radius of the coil)} \tag{5.2c}$$

**Independent and Dependent Variables**

$$d = \text{(Needed to solve)} \qquad \text{(Diameter of the wire to be wound )} \tag{5.3a}$$

$$a = \pi \times \frac{d^2}{4} \qquad \text{(Cross section area of the wounded wire )} \tag{5.3b}$$

$$n = \frac{A_{eff}}{a} \qquad \text{(Number of turns of the wounded wire in each coil)} \tag{5.3c}$$

$$l = 2\pi R n \qquad \text{(Length of the wounded wire in each coil)} \tag{5.3d}$$

$$r_{th} = \rho \times \frac{l}{a} \qquad \text{(Theoretical resistance of the wounded wire on each coil)} \tag{5.3e}$$

$$B = \text{Constant Value} \qquad \text{(Field due to each coil at the center of the confuguration)} \tag{5.3f}$$

$$i = B \times \frac{2R}{\frac{4^{3/2}}{5}\ \mu_0 n} \qquad \text{(Current through each coil in Helmholtz configuration)} \tag{5.3g}$$

$$V = i \times r \qquad \text{(Voltage across each coil in Helmholtz configuration)} \tag{5.3h}$$

We then plotted Current (i) and Voltage (V), at any constant value of Magnetic Field (B), with respect to the Wire Diameter (d). We chose the point of intersection between i and V as the optimal point of operation, which gave us an optimal value for the wire diameter.

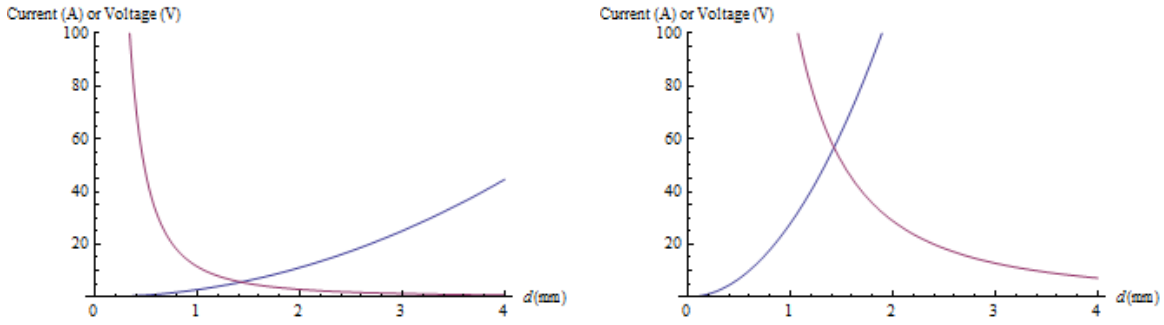


Figure 27: Plot of current and voltage at each Helmholtz coil, with respect to the wounded wire diameter (d)(a)At 10 mT magnetic field, (b)At 100 mT magnetic field. As can be seen from both the plots, the intersection point of d is independent of the magnetic field.

This gave an optimized value of $d$ as 1.43 mm (at values of current and voltage, that we could get to by the power supplies that we already had). WE then decided to use the wire gauge closest to that value, which is 15 AWG ($\phi$: 1.45 mm). Using this value, following dependent variables were calculated.

**Calculated Dependent Variables**

$$d = 1.45\ mm$$

$$n \approx 235$$

$$l \approx 91.4\ m$$

$$r_{th} \approx 0.94\ \Omega$$

These were the considerations taken into account in designing the Z-direction Helmholtz coil. Using these calculations, we bought the required length of 15 AWG copper wire, with polyimide insulation for high temperature tolerance, and got it carefully wound in the machine shop. An adequate quantity of heat sink paste was applied during winding, to ensure

good heat dissipation during operation. Experimentally, the resistance of the wounded wire ($r_{exp}$), without any current flowing, was found to be $\approx 1.7\ \Omega$.

**XY-direction coils** To produce variable magnetic fields in the X and Y direction, four more coils, two for each direction, were mounted on the Z-direction coil. The radius, and thus the wounded wire specifications, of the X and Y coils was chosen to be the same as the Z-direction coil, but due to getting mounted on the Z coil, neither of X and Y coils were in Helmholtz configuration. Design of a single coil and top view of the assembly of all the coils is shown in the figure below. For the purpose of mounting the X and Y-coils, the Z-direction coil had to be slightly modified. Mounting the X and Y-coils covered the old water channel inlet/outlet, and new inlet/outlet were made in the Z-coil, which connected to the old channel. The old inlet/out were plugged. Provisions were also made to attach an electrical terminal block to one of the X/Y coils, to make electrical connections between these three set of coils and their respective power supplies.

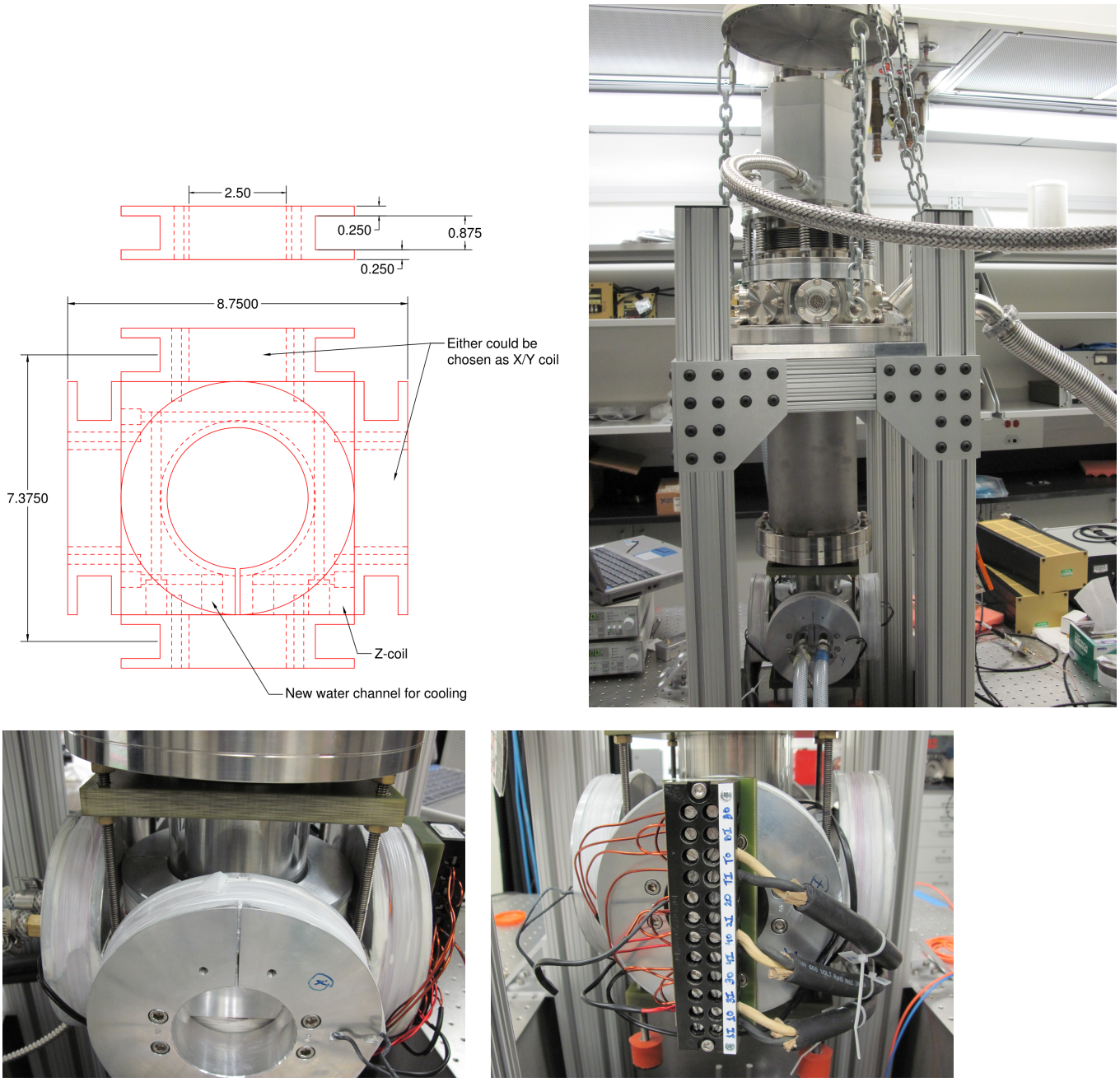


Figure 28: Building the X and Y Coils around the Z-Coils (a)Design of the X and Y-direction coils added around the Z-Coils, (b)Physical placement of all three sets of cols around the cryostat, (c)Close-up of all three sets of coils and (d)Close-up of all three sets of coils with the terminal block for electrical connection.

**Electrical Connections** After getting the coils made and wound, the next task was to hook them up to power supplies. For this purpose, we bought three Agilent power supplies, one for each direction. The part numbers and specifications of these power supplies are listed in the table below:

| Direction | Part Number | Specification |
|---|---|---|
| X and Y | 6652A | 25A, 20V |
| Z | 6673A | 60A, 35V |

Table 6: Power supplies used for the electromagnetic coils

We then tried to calculate the magnetic field values that we could get by connecting our coils to the power supplies. In doing so, we had the option of connecting the two coils for each direction either in series or parallel to the power supply. A quick calculation, as shown below, showed that connecting the coils in parallel will be more advantageous. The following equations use the same constants as defined in equation set 5.1 and 5.2.

**Powering Z-Coils**

$$B_Z = \frac{4}{5}^{3/2} \frac{\mu_0 n i}{R} \text{(Magnetic field at the center of the Z-coil pair)} \tag{5.5}$$

**Connecting coils in Series - Running Voltage Limited**

$$V|_{max} = 17.5\ V \qquad \text{(Voltage at each coil)} \tag{5.6a}$$

$$i = \frac{V}{r_{th}} \qquad \text{(Current through each coil)} \tag{5.6b}$$

$$B_{Z|max} \approx 64\ mT \qquad \text{(Calculated magnetic field)} \tag{5.6c}$$

**Connecting coils in Parallel - Running Current Limited**

$$i|_{max} = 30\ A \qquad \text{(Current through each coil)} \tag{5.7a}$$

$$V = i \times r_{th} \qquad \text{(Voltage at each coil)} \tag{5.7b}$$

$$B_{Z|max} \approx 102\ mT \qquad \text{(Calculated magnetic field)} \tag{5.7c}$$

**Powering XY-Coils**

$$B_{X/Y} = \frac{2\mu_0 n i R^2}{2(R^2+d^2)^{3/2}} \text{(Magnetic field at the center of the X/Y-coil pair)} \tag{5.8}$$

where d = Distance between the coils. For our geometry, d = 3.6875".

**Connecting coils in Series - Running Voltage Limited**

$$V|_{max} = 10\ V \quad \text{(Voltage at each coil)} \tag{5.9a}$$

$$i = \frac{V}{r_{th}} \quad \text{(Current through each coil)} \tag{5.9b}$$

$$B_{X/Y|max} \approx 8.5\ mT \quad \text{(Calculated magnetic field)} \tag{5.9c}$$

**Connecting coils in Parallel - Running Current Limited**

$$i|_{max} = 12.5\ A \quad \text{(Current through each coil)} \tag{5.10a}$$

$$V = i \times r_{th} \quad \text{(Voltage at each coil)} \tag{5.10b}$$

$$B_{X/Y|max} \approx 10\ mT \quad \text{(Calculated magnetic field)} \tag{5.10c}$$

We thus connected our coils parallel to each other and to the power supplies. Using the magnetic field sensor, as described in Section 5.5.3, we measured our experimentally achieved magnetic field from the coils to be very close to the above predictions.

**Iron frame and cores** As shown in the above calculations, we expected the magnetic field in the x and y-direction, to be ≈ 10 mT. Considering, that we wanted our net external magnetic field to be ≈ 102 mT as explained in Chapter 2, we tried a couple different ways to increase our magnetic field in the x and y-directions. The way we finally pumped up the fields in these directions was by using ductile cast iron pieces around these coils. For this purpose, we bought a rod (Grainger: 3ANR2) and a thick plate (Farmers Copper Ltd.: 1" thick, 3" wide) of cast iron alloy 65-45-12, which has high permeability and low hysteresis (a comparison chart of different alloys of iron is given in http://www.daycounter.com/LabBook/Physical-Properties-Ductile-Iron.phtml). Using these,

we machined some cores and a frame to go around the x and y coils, as shown in the design and pictures below.

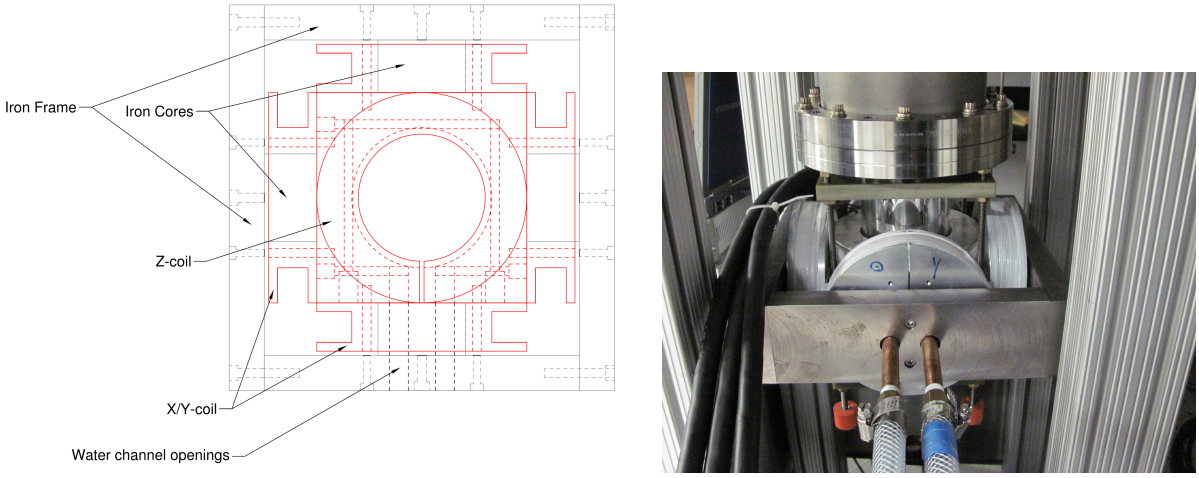


Figure 29: Cores and a frame were attached around the X/Y coils to increase the external magnetic field (a)Design of the cores and frame added around the X and Y coils and (b)Actual setup of the cores and frame around the coils (cores are not visible in this picture)

After attaching the iron cores and frame around the coils, we were able to get $\approx 25$ mT magnetic field in the X and Y-direction. The maximum attainable magnetic field in each direction and their respective calibration using the power supplies is shown in the table below. Experimentally, continuous use, for periods longer than 10-15 minutes, of X and Y-coils close to their maximum limit created problems. Such continuous use heated up the wire of the coils which increased its resistance, thus dropping more voltage to maintain a constant current. This led to the power supplies reaching their voltage and current-limits, which further led to a continuous decrease in the magnetic field. If the X and Y-coils needed to be used close to their limits for extended periods of time, we would periodically shut off the current for a few minutes to cool down the coil wire. E.g. to provide 15-18 mT, I had to run the power supplies with $\sim 50\%$ duty cycle, i.e. alternating on/off for equal amounts of time; and to provide 20-25 mT, I had to run the power supplies with $\sim 30\%$ duty cycle, i.e. keeping on for one-third of the time and shutting off for the remaining two-thirds. This is how the plots shown in Chapter 8 were obtained.

The experimentally measured data and its linear fit for the magnetic field in the Z-direction is shown in the figure below. Such fits were done for each direction, and the slope of such fits are used as the calibration for each direction. In the Z-direction, as shown in the figure below, the intercept of the linear fit is decided by the permanent magnet in the system, if any. In the plot shown below, a 90 mT magnetic field was attained in the Z-direction using permanent magnet(s).

| Direction | Maximum Field, $B_0$ (mT) | Calibration, K (mT/A) |
|---|---|---|
| X | 25 | 1.04 |
| Y | 25 | 0.996 |
| Z | 102 | 1.64 |

Table 7: Maximum magnetic field and their calibration in the respective three directions

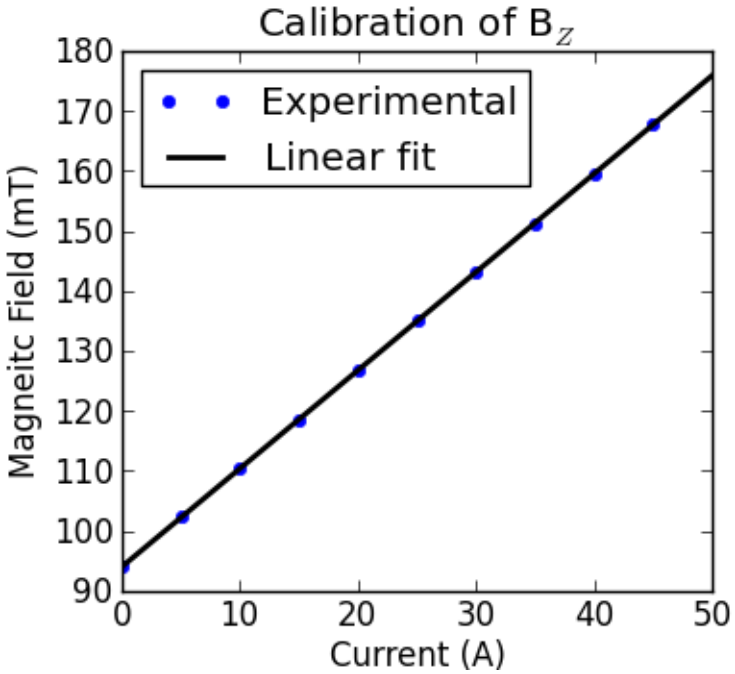


Figure 30: Available B-field and its calibration (in mT/A) in the Z-direction

**Relays for all three directions** After maximizing the magnetic fields we could get from our coils, in combination with the power supplies, iron cores and frame, as described above, the next challenge we faced was to flip the three fields into their negative directions. This was done using double-pole-double-throw (DPDT) relays, in conjugation with safety diodes and voltage regulators. The main components used for this relay circuit are given in the table below. A camera-clicked picture of such a circuit for one of the three directions and a layout of the circuit are also shown below.

| Label No. | Part name | Brief description | Newark Part No. |
|---|---|---|---|
| DPDT | Relay | DPDT Relay | 56F641 |
| D1 | Safety diode | For protection of power supply | 53H9635 |
| D2 | Safety diode | For protection of relay coil | 05R5983 |
| VR | Voltage regulator | To provide 12V to relay | 89K1395 |

Table 8: Description and part numbers of elements in the relay circuit

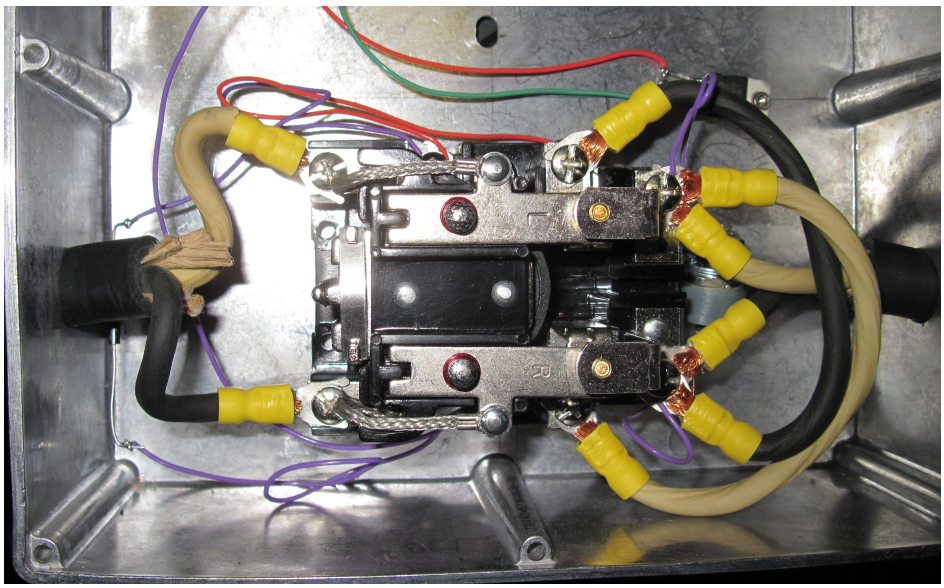

Figure 31: Picture of the relay circuit for one direction

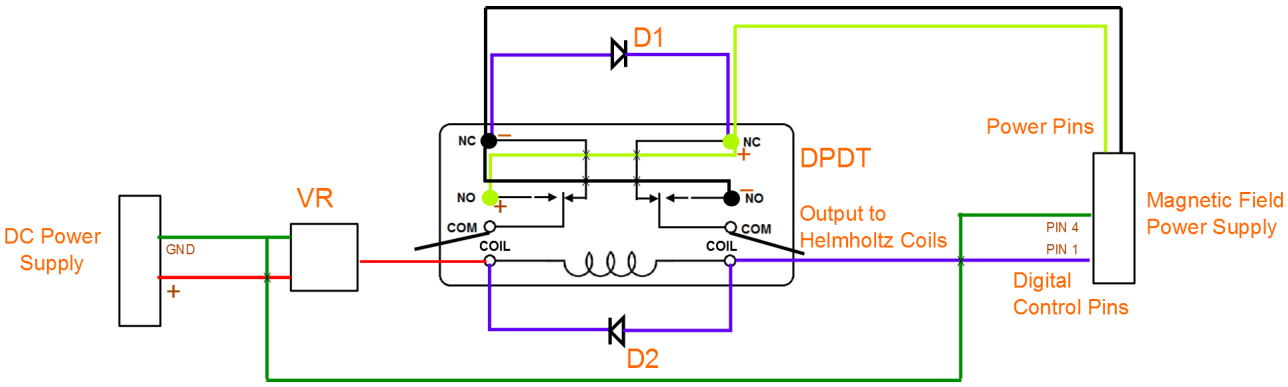


Figure 32: Layout of the relay circuit

The relay circuit employed a DPDT relay, with 12 V DC voltage required for the operation of the 70 $\omega$ coil (maximum current passing through the coil should be $\sim$200 mA). A safety diode (D2) rated for a maximum current of 1 A was used to protect the relay coil. Another high-power safety diode (D1) was used to protect the magnetic field power supply from any unintentional current reversal.

To control the relay, the magnetic field power supply's digital control terminal block on the back panel was used. To access the digital operations of the power supply, a jumper on its GPIB board (which was accessed after removing its top cover) was moved to a different location, as described in the power supply's operating guide. With this change, PIN 4 of the digital block was used as a ground pin, and PIN 1 could be programmed to provide either a HIGH or a LOW signal, using the DIG:DATA command, as described in the power supply's programming guide. For the operation of the relay coil, one end of the coil was provided 12 V DC (using a heat-sunk voltage regulator with a 24 V power supply), and the other end was connected to the digital PIN 1 described above. When a positive B-field was required (i.e. direction of the output current same as the input), value '3' was sent to the digital controller of the power supply - pulling PIN 1 to a HIGH state and thus not activating the relay coil. When a negative B-field was required (i.e. direction of the output current opposite to that of the input current), value '2' was sent to the digital controller - pulling PIN 1 to a LOW state, enabling the relay coil, and thus throwing the relay to the other pole, which was connected with the opposite polarity.

The need for the relays was to reverse the field direction to maximize the possibility of magnetic field interaction with the NV centers. As shown in the Chapter 2, $\approx$ 102.5 mT magnetic field is needed for maximum interaction with the NV centers. This maximum interaction regime can be thought of as a sphere with radius of 102.5 mT (the positive and negative halves of this sphere about the XY plane denote interaction between $|0\rangle$ and $|-1\rangle$ spin states and $|0\rangle$ and $|+1\rangle$ spin states respectively). Because of our above-mentioned physical limitations on the magnetic field coils, out of this maximum interaction sphere, the available region of magnetic field can be denoted as a cuboid of height $\pm$ 100 mT, with a square base of $\pm$ 25 mT in the XY plane. Because of this, to enable interaction with the NV centers, the maximum radius of a full sphere available to us is 25 mT. Beyond 25 mT, conical caps formed at the intersection of a sphere and the cuboid, of a specific magnetic field are available for interaction with the NV centers. Examples of these regions of availability are shown in the figure below.

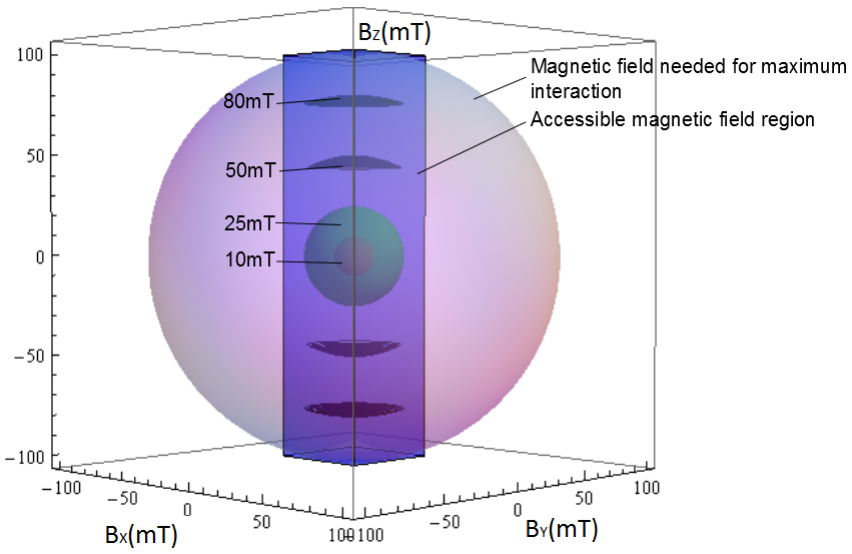


Figure 33: Maximum required and available magnetic field for interaction with the NV centers

### 5.5.3 Magnetic Field Sensor

A sensor was needed to measure the magnetic field produced by the above permanent magnets and the coils at the sample. For this purpose a sensor was installed inside the cryostat, which could be mounted at the spot of the sample at will.

**Specifications** A transverse single-axis Hall Sensor (F.W. Bell: BHT-921), meant for cryogenic operations, was bought for this purpose. The data sheet and calibration table for this sensor is attached in Appendix A. This four-lead sensor required a current source and voltage sensor/meter. The following were used for these functions.

**Current Source** As mentioned in the hall sensor's data sheet, the nominal control current for the sensor is 100 mA. To obtain this, I built a home-made current source using AD588JQ voltage reference chip. I used the 'Boosted Precision Current Source' application mentioned in the datasheet of this reference chip. The specifications of our circuit are shown in the layout circuit below.

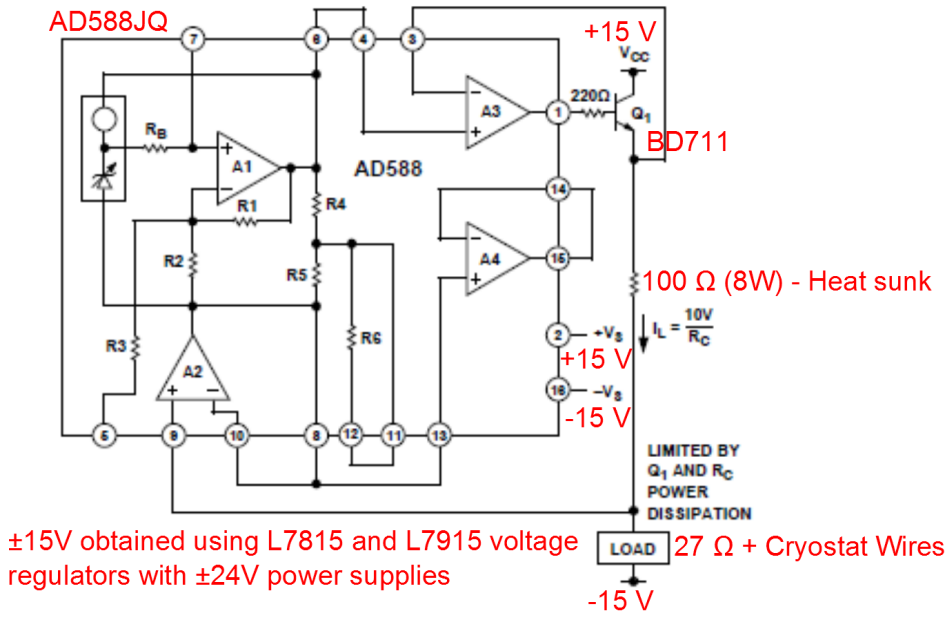


Figure 34: 100mA current source built to control the magnetic field hall sensor

A twinaxial cable was used to carry the DC current from the current source to the cryostat. Inside the cryostat, a twisted pair of the same wire as mentioned in Sec. 5.4.2 was used to carry the current to the Hall Sensor. As shown in the above circuit, one end of this twinaxial cable was tied to -15V to guarantee that the circuit was able to drive the 100 mA current through the cryostat wires to the field sensor.

**Voltmeter** To measure the voltage difference that developed across the other two terminals of the Hall sensor, I used a digital multimeter (Keithley: Model no. 2000). A twisted pair of wires mentioned above was again used to transmit these voltages from inside of the cryostat to the outside. A twinaxial cable was then used to carry these voltages from the outside of the cryostat to the voltmeter. The unloaded (as there was no resistive load put in parallel with the sensor) sensitivity of the magnetic sensor, as mentioned in its calibration sheet, is 0.793 mV/kG with 100 mA as the control current. Using this conversion factor, I was able to measure the magnetic field at the position of the sensor.

This control and measurement methodology of the sensor was used to obtain calibration curves for all three directions, such as the one shown in Fig. 30.

# 6.0 ACTUATION AND DETECTION

## 6.1 DEVICE

### 6.1.1 Actuation

#### Past methods

To drive the NMO devices, we started by trying to drive them with piezo-electric actuators.

The first kind of actuators that we used were 2-layer rectangular bending actuators (Piezo Systems Inc.: T220-A3NM-103Y). We used them in the Y-poled configuration, as shown in the figure 35. Due to their low resonant frequencies ($\approx$ 300 Hz), they were unable to drive our devices into resonance.

The second kind of actuators that we used were Ring Actuators (Noliac: NAC2121). These solved the above problem for us, cause of their high-enough unloaded resonant frequency (486 kHz) and blocking force ($\approx$ 1060 N). But these actuators drove numerous modes in our device simultaneously, due to which it was almost impossible for us to study any mode individually.

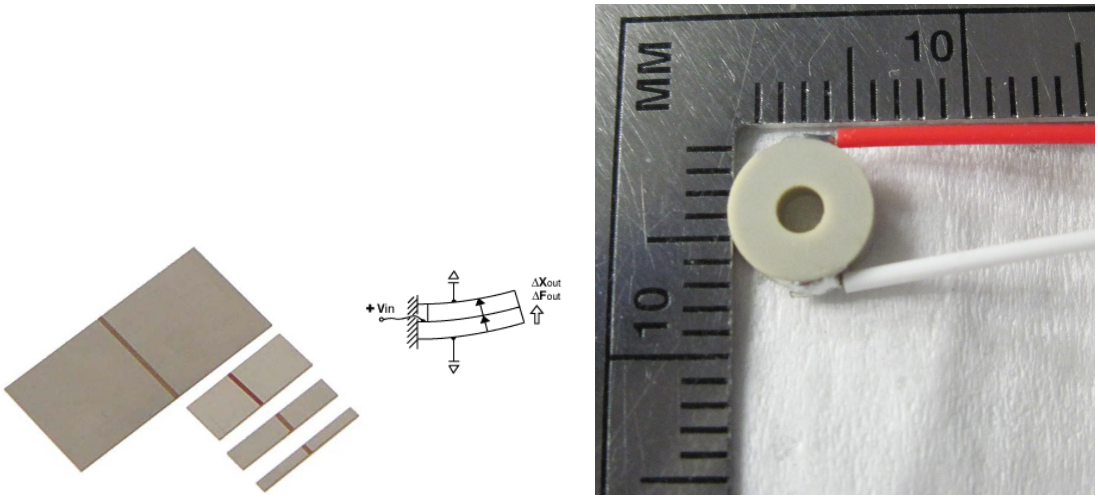


Figure 35: Piezo actuators used to drive the NMO devices into resonance: (a)Bending Actuators: didn't work because their resonant frequency was much lower than that of our devices; and (b)Ring Actuators: These excited numerous mixed modes in our devices.

**Present scheme**

Due to the above problems, we stopped driving our devices with piezo-electric transducers, and instead started driving them electrically, as will be explained in the rest of this section.

*Theory*

We use electrostatic actuation to drive the devices into resonance. As described in Section 4.4, our devices are suspended ≈580nm-1.46$\mu$m above the bottom of the grooves. We apply electrical voltage to any one point on the graphene film, and due to its conductive nature this voltage can be detected on the whole film. We also electrically ground our substrates to provide a return path for the current. This forms a capacitor between our devices and the substrate. Applying a sinusoidal voltage of varying frequency to such a device forces the device into resonance at its natural frequency. We also apply a DC voltage to the devices to keep them in tension.

Mathematically, the voltage ($V$) applied to a device can be written as:

$$V = V_{dc} + V_{ac}\sin(\omega t). \tag{6.1}$$

The force ($F$) that the device then faces due to this voltage goes as the square of the voltage

$$\begin{aligned} F &\propto V^2 = (V_{dc} + V_{ac}\sin(\omega t))^2 && (6.2)\\ &\propto V_{dc}^2 + 2V_{dc}V_{ac}\sin(\omega t) + V_{ac}^2\sin(\omega t)^2 && (6.3)\\ &\propto (V_{dc}^2 + \frac{1}{2}V_{ac}^2) + 2V_{dc}V_{ac}\sin(\omega t) - \frac{1}{2}V_{ac}^2\cos(2\omega t). && (6.4) \end{aligned}$$

The first term in the force keeps the device under tension. The second term drives the device at $\omega$ and the third term drives the device at $2\omega$. The detection scheme is set up to detect the device response at frequency $\omega$ and thus we can neglect the third term in the force.

*Experiment*

We use AC and DC synthesizers to apply the above-mentioned drive voltages to our samples. These are further explained in Section 6.1.2.2. These voltages were transmitted to the cryostat using BNC and SMA cables, and were transmitted inside the cryostat using the SS-Cu coax cables.

To apply these voltages to our devices, we designed and developed a probe mechanism. This *probe holder* is made of PEEK and we use a platinum wire, ≈500 $\mu$m in diameter, as the probe in this holder. The probe is kept under tension in the holder using 0-80 screws. Electrical contact was made to the probe through the copper tail-end of the co-axial cable inside the cryostat.

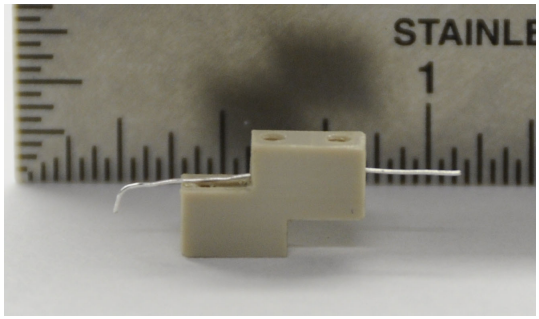


Figure 36: Probe setup used to apply voltages to the sample in the cryostat

To contact the film, I put small blobs of conductive *silver paint* (SPI supplies: 5001) on the corners or edges of the graphene film. I then contact one such blob with the probe. Due to good electrical conductivity of graphene, this voltage can then be detected at any point on the film, and thus reaches our devices. These silver paint blobs can be seen on our sample in the picture taken on an optical microscope, as shown below. Also shown in the figure is a schematic of the electrical actuation scheme of our devices.

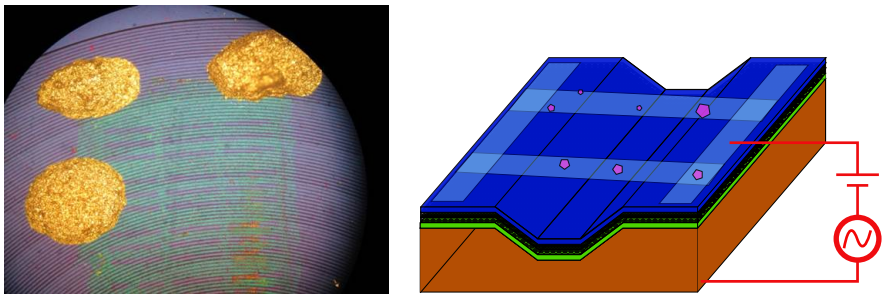

Figure 37: Components used for the electrical actuation of the NMO (a)Silver paint blobs, used to electrically contact the devices, can be seen in this picture taken in the optical microscope. A similar blob, almost diametrically opposite to the actutation blob, was contacted using a detection probe to ensure the voltages were reaching the film and (b)Schematic of our devices on the pre-processed substrates, shown here with the electrostatic actuation scheme. The pink circles on the devices show the nano-diamonds.

A *detection probe* similar to the actuation probe, as was mentioned in Section 5.4, was used to ensure the voltages were getting to the graphene film. The detection probe was also brought into contact with a different silver paint blob. I tried to align the actuation and detection probes in a way such that the devices being looked at were somewhere in between the two.

### 6.1.2 Detection

#### 6.1.2.1 Optical

*Principle*

We employ thin-film optical interference to detect the motion of our oscillators. As described in Section 4.4, the devices are suspended over anti-reflection coated flat-bottom grooves, their depth varying between $580-1460\ nm$. When we shine red-laser light on our sample, thin-film interference occurs on the devices between the light reflected directly off the device, and off the bottom of the grooves. As the device moves, the distance between the device surface and the bottom of the groove changes, thus changing the intensity of the interference light. We collect this interference light as our signal. The AR coatings at the bottom of the grooves

help in enhancing our signal-to-noise ratio. Shown in Fig. 38 is a picture of a sample with graphene, devices and film, in the optical microscope; subtle interference colors can be seen on the suspended areas.

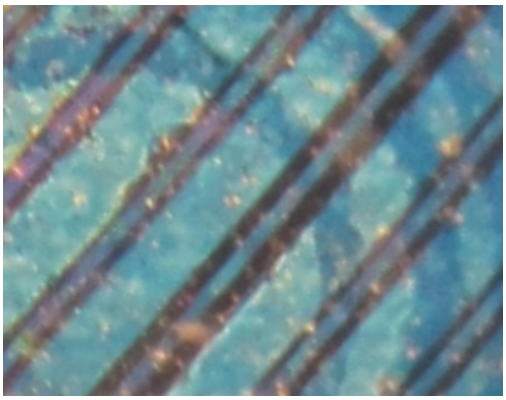

Figure 38: Sample with graphene suspended over grooves - Subtle interference colors are visible.

*Experimental Realization*

The optics for laser-light incidence on and detection from our sample is set up as shown in the figure below. Almost all the optics, as a unit, are positioned on a shelf under the cryostat.

The whole chain of optics can be briefly explained as follows: A red laser diode is mounted in a temperature and current controlled mount, which also houses a collimation lens. Collimated light from this setup is made to pass through an Optical Isolator and coupled into a polarization maintaining single-mode fiber with angled-ferrule, using another focussing lens. The purpose of the Isolator and a fiber with angled-ferrule is to reduce back-reflections of the laser into itself, thus decreasing any instability caused due to it. The optics till this point are all above the table, and using the fiber, the beam is then taken to optics under the table. The beam from the fiber is collimated using another collimation lens, and is made to pass through a beam splitter. A 2D Galvo Mirror System is put in the beam path to enable 2D laser-scanning of the sample. The beam then goes through two achromat lenses which act as a beam magnifier, which magnifies the beam to suit the next piece in

the chain. The beam then falls on to the objective, which focusses it on to the sample. This objective is placed inside the cryostat, and gets cooled down with the sample. The lenses and the objective are so positioned such that the beam falling on the Galvo is imaged at the back of the objective. The beam then reflects off the oscillating NMO, the intensity of which would vary due to optical interference, as explained above. This beam then traverses the return path and gets collected into a multi-mode fiber. It then goes into an Avalanche Photo Detector (APD), and gets converted into an AC current signal, that is then detected by electronics components. Another half of this beam is also projected on to a CCD camera using Pellicle Beamsplitters. An LED (white or red, depending on the objective and laser used - e.g. Partec objective had large chromatic aberration, thus red light had to be used for illumination while using red laser for device detection) is also put into the chain as a source of illumination for the sample. This illumination light also gets reflected off the sample, and is collected at the CCD camera to view the sample. A layout of the optical components and a picture of the actual optics setup is shown in Fig. 39(a) and Fig. 39(b), respectively. Part numbers and descriptions of the optical elements used are provided in Appendix A, Section A.1.

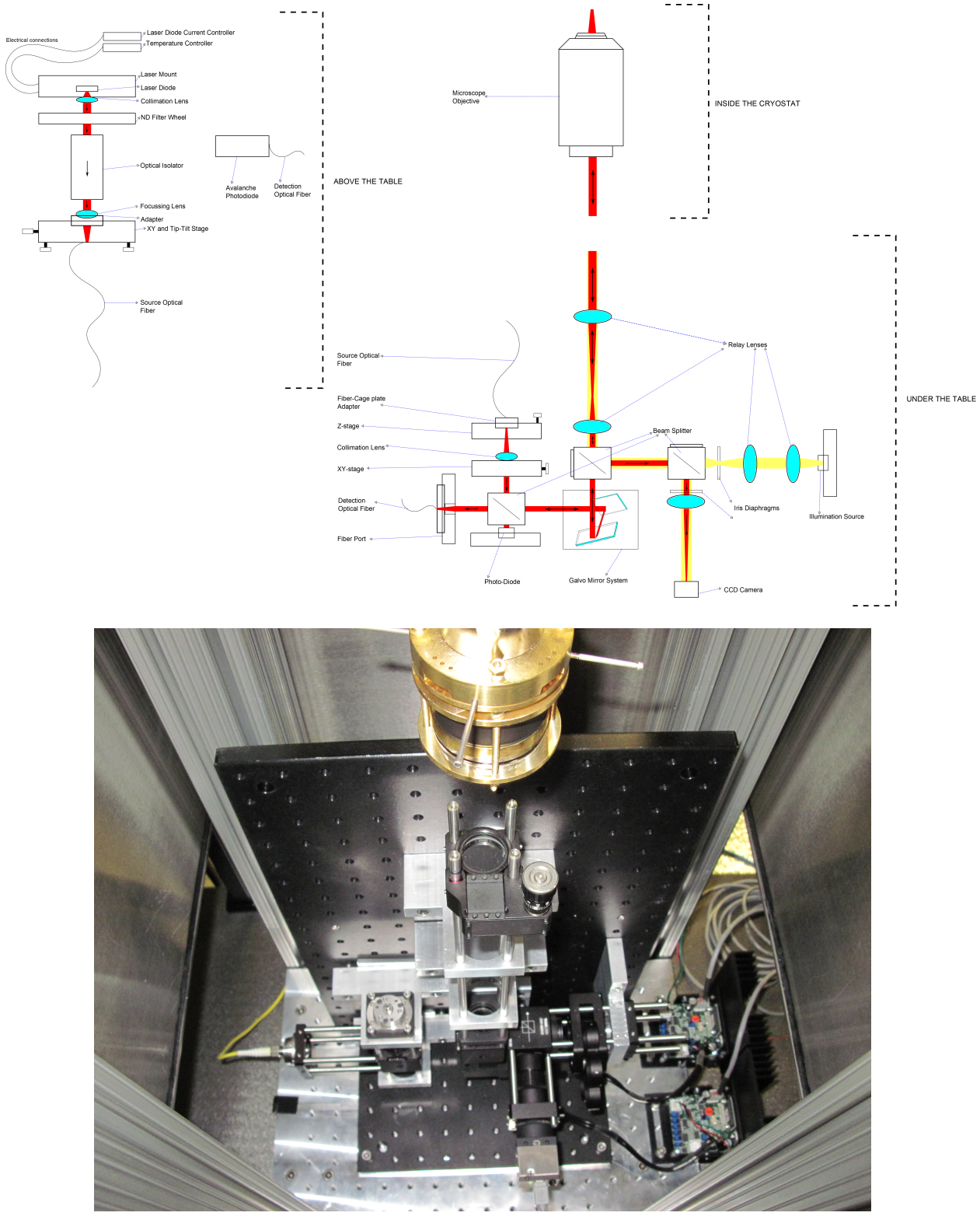


Figure 39: Optics used to detect the motion of the NMO (a)Layout of the optical components and (b)Actual optical setup, under the cryostat

**6.1.2.2 Electrical** As mentioned in section 2.1, the expected oscillation frequencies of our devices were in the radio frequency (RF) range i.e. 20 kHz to 25 MHz. We accordingly set up RF electronics for the detection of the oscillation frequency of our devices.

*Principle*

We employ Heterodyne Detection to study the resonance modes of our devices. This method is used for detecting radiation by non-linear mixing with radiation of a reference frequency. We use a lock-in amplifier for this purpose. The basic principle behind this detection scheme is that a drive signal is split into two channels, one of which goes through the experiment, and the other, the reference signal, does not. The channel that goes through the experiment has all the information from the devices. After this, both these channels are treated identically. Both these channels are then put into a lock-in amplifier, which can then extract out any device information from the channel that was put through the experiment, by non-linear mixing of this channel with the reference channel. This way the lock-in can extract out the amplitude and phase of any device response, with respect to the reference channel.

*Experimental Realization*

After the APD the optical signal from the experiment gets converted into a Radio Frequency (RF) electronic signal. This signal is then made to go through a few electronic components, as explained below and shown in Fig. 40(a) and Fig. 40(b), to extract the oscillator resonance information from it.

A synthesizer is used to provide varying-frequency ac voltages. One part of this ac-drive is added with dc voltages to drive the devices. Another part is used as a reference signal, for Heterodyne Detection of the experiment signal. The optical output from the experiment is converted to a varying-frequency ac signal after the APD. From this signal we detect the component that is at the same frequency as the drive signal, as explained above.

Both the actual and the reference signals are up-converted using mixers and local oscillators to 21.4MHz signals and made to pass through very narrow bandwidth (5kHz) Crystal Filters to eliminate a large portion of the noise. Both the signals are then down-converted to 10kHz to be able to put into a lock-in amplifier, which extracts the amplitude and phase of the actual signal. Refer to Appendix A, Section A.3 for more details of the setup.

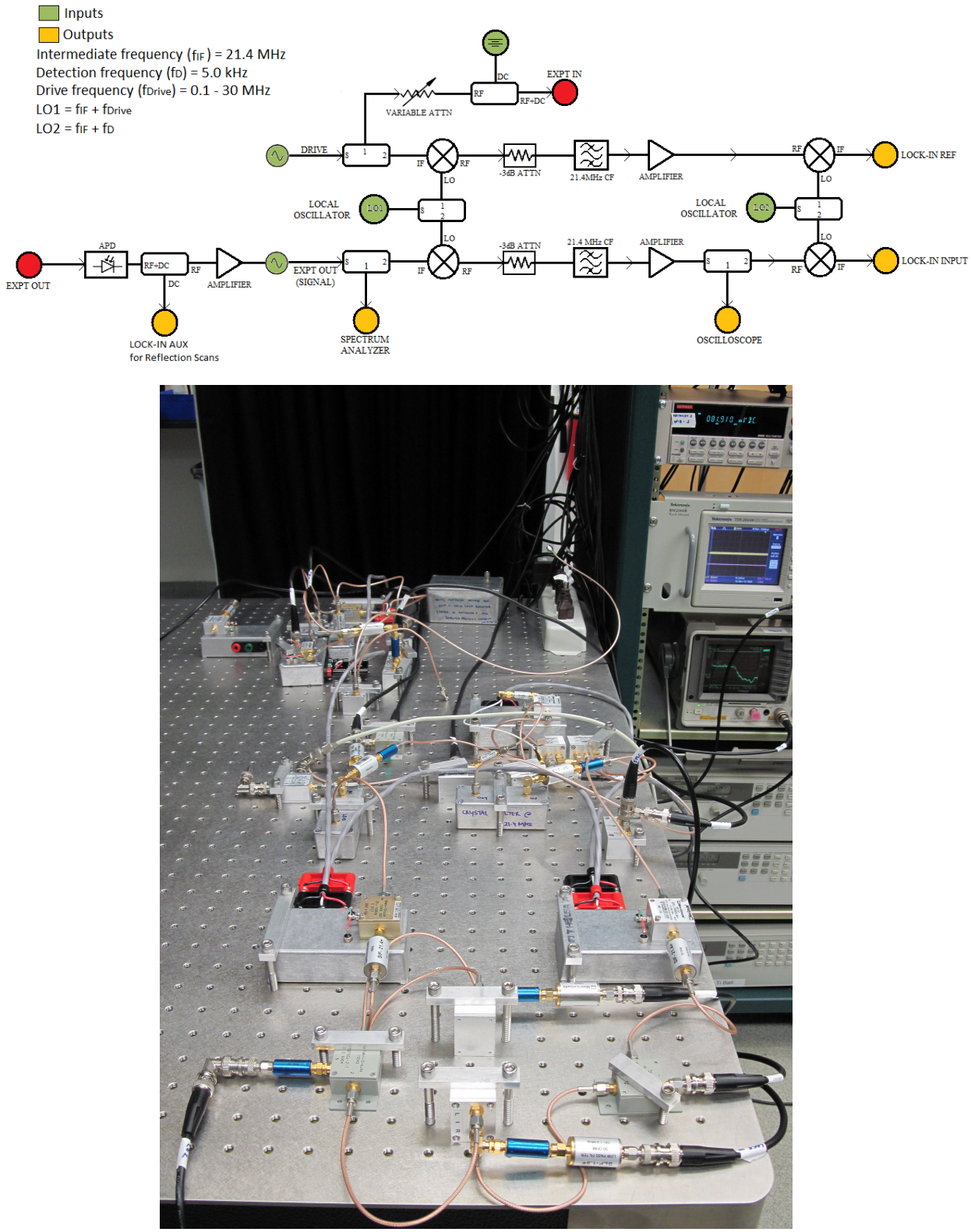


Figure 40: Electronic components used to detect the motion of the NMO (a)Layout of the electronic components and (b)Actual electronics setup

## 6.2 NV CENTERS

The NV centers are known to exist in negative ($NV^-$) and neutral ($NV^0$) charge states [110]. $NV^-$ has been more extensively studied due to its ease of detection with conventional magnetic resonance techniques. This state of the NV center is known to have six electrons [25], thus having an integer spin ($S = 1$) and a spin triplet ground state (from this point, I will simply use NV for $NV^-$ state of the NV centers). The energy level structure of the NV center is shown in the figure below.

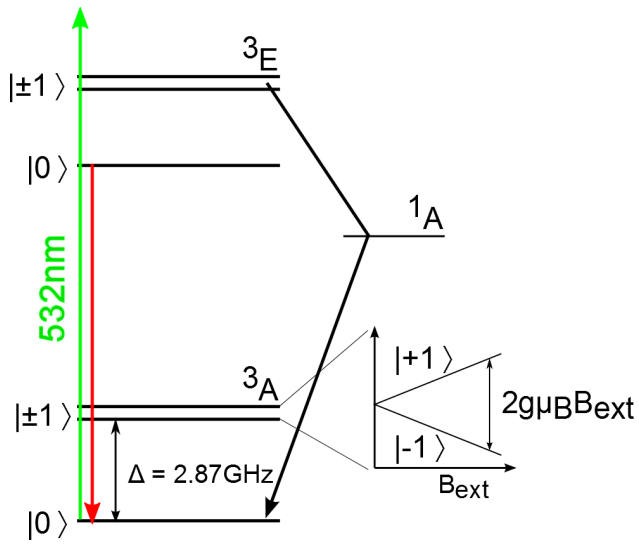


Figure 41: Energy structure of the ground state of the $NV^-$ center.

We employed electron paramagnetic resonance (EPR) or electron spin resonance (ESR) electron for the detection of the NV centers. This technique is used for the detection of systems with unpaired electron spins. This technique uses magnetic fields and electromagnetic energy, usually in the microwave (MW) range, to induce transitions between various spin states, and thus resulting in an absorption spectra. ESR has been used as a detection technique for NV centers since late-1970s [26]. To use this technique for our purposes, a few components were needed in the experimental setup, as discussed below:

*Confocal Microscopy Setup* For the ESR technique to be performed on the NV centers, they had to be optically excited and their fluorescence had to be optically detected. For

this purpose, some modifications were made to the optical setup used for device detection. Following are the biggest changes made to that setup:

1. As can be seen in the above-shown energy-level diagram of the NV centers, a green laser at $\lambda$ =532 nm leads to broadband optical excitation. Thus, the biggest change made to the CLSM optics setup was the swapping of red laser with a green one, and any optical component not designed to operate in this wavelength range. Details of this setup are given in Appendix A.

2. The NV center's emitted fluorescence, on relaxing after green-laser excitation, is in the 630 nm - 800 nm wavelength range. Because of this, another major change that had to be made in the optical setup was the addition of a dichroic mirror. This was added at 45° to the incoming beam, because of which the incident green laser beam reflects off this mirror and changes direction by 90° with respect to the incoming direction. From here on, the setup is the same as for device detection. On the way back from the sample, due to the dichroic mirror and other filters, the wavelengths between 630 nm-800 nm are detected, which mark the presence of fluorescence from the NVs.

Other than the above-mentioned big changes, the rest of the optical setup mostly remained the same, and is as explained in the previous section.

The layout and setup of the optics explained above is shown in the figure below:

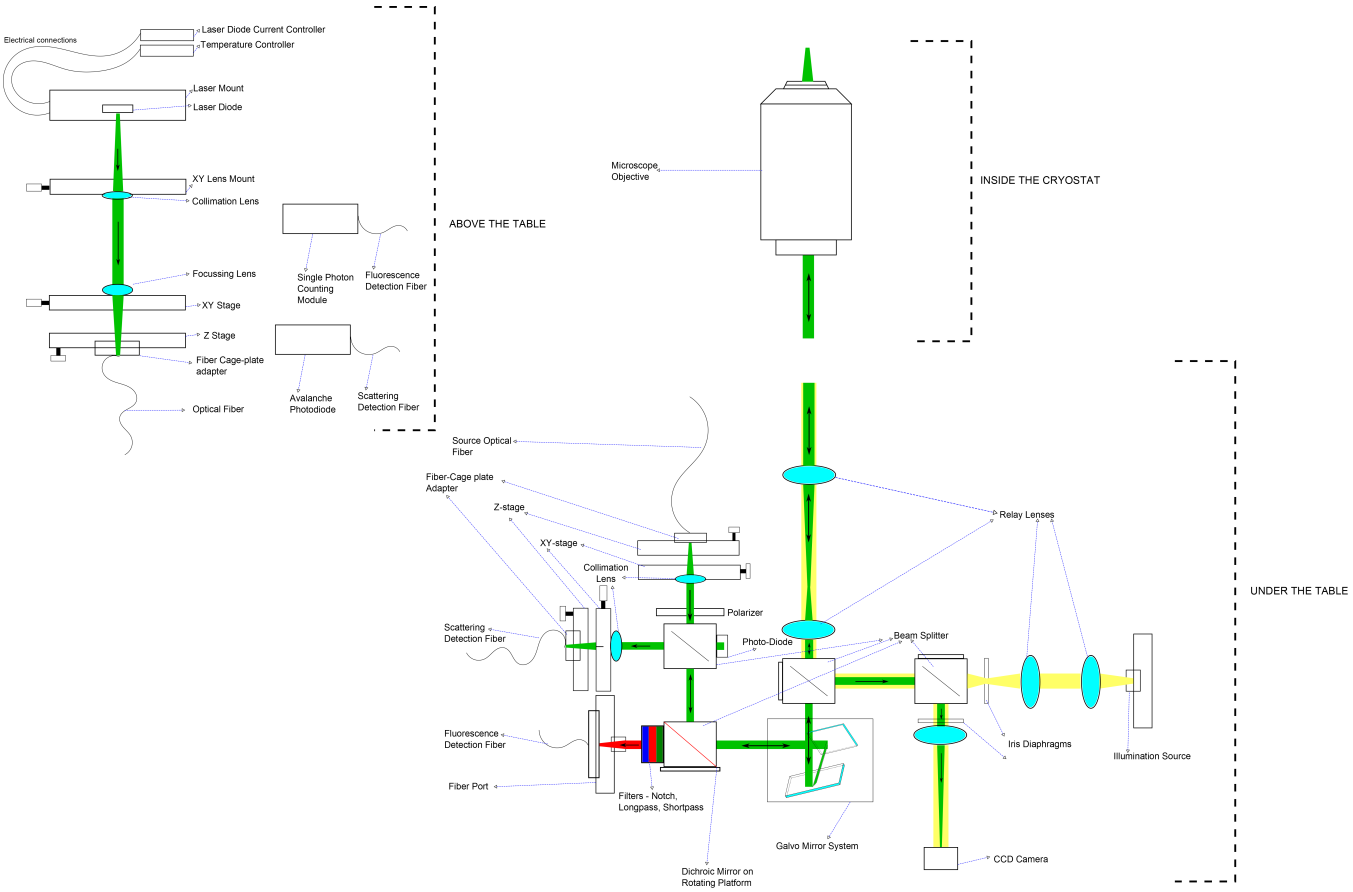


Figure 42: Schematic of the optics used to detect the presence of NVs, and characterize them

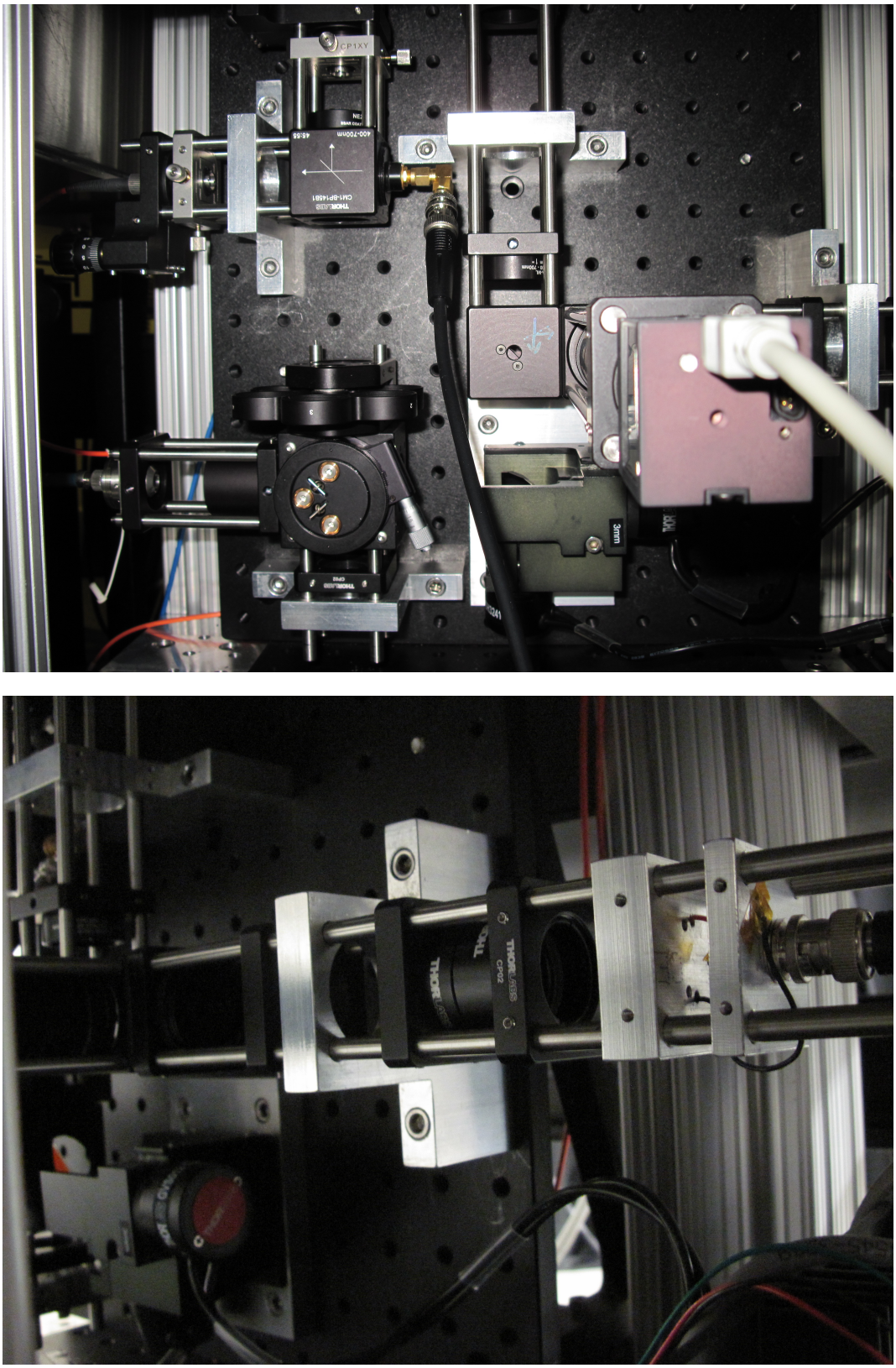


Figure 43: Actual optics used to detect the presence of NVs, and characterize them

A list of all the optical components used in the above optical setup is put in appendix A.

*MW Drive* To drive resonant transitions between spin states of the NV centers, an electromagnetic energy in the MW frequency range was required. As seen in the energy-level diagram above, in the absence of an external magnetic field, the spin states are separated by 2.87 GHz. On applying a magnetic field, this energy separation decreases linearly. Thus, for the application of this MW drive to the cryostat, we used a MW synthesizer (output∼10-12 dBm), some low-attenuation cables and a MW amplifier(gain∼8-10 dB). Refer to Appendix A, Section A.4 for details. Inside the cryostat, I used the SS-Cu coaxial cable, described in Section 5.4.1, to get the MW drive to the sample. The last bit of this coaxial cable is a copper coax, again described in Section 5.4.1, to which I soldered a twisted pair of polyimide-coated copper wire (≈140 $\mu$m in diameter), and to that soldered a gold-plated tungsten wire (≈30 $\mu$m) in the form of a loop (tried different shapes and dimensions, such as circular 2-3 mm, circular 5-6 mm, V-shaped etc). A schematic and a picture of the actual loop is shown in the figure below. As this drive line was practically shorted, a 3 dB attenuation was put on the MW cable before going into the cryostat, for frequencies less than ∼1 GHz (A couple amplifier chips got destroyed before I started doing this technique).

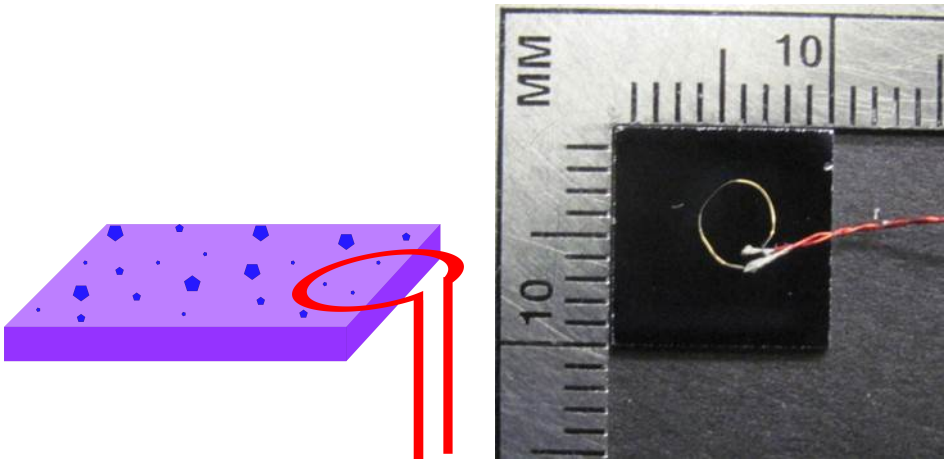


Figure 44: A 30 $\mu$m gold-plated tungsten wire was shaped in the form of a loop for applying MW drive to the samples inside the cryostat. A schematic and an actual picture of such a loop on a sample with diamond nanocrystals, as used in Chapter 8, is shown here.

*Magnetic Fields* External magnetic field is required to enable Zeeman splitting. This is provided using the electromagnetic coils described in Section 5.5.2, and the few more details of the accessible fields in explained in Section 8.3.

A *Single Photon Counting Module (SPCM)* (Excelitas: SPCM-AQRH-14-FC) was used to detect the fluorescence from the NV centers. The signal from the SPCM was put into a home-built Arduino-based electronic counter, which was connected to the computer for a direct read-out. Quite a few versions of this counter have been made, revised and re-made and is still a project-under-revision. The final version of the circuit that was used for the NV characterization is shown in Appendix A, Fig. 65.

# 7.0 DEVICE PERFORMANCE

The fabricated NMOs, as doubly-clamped ribbons and/or drumhead resonators, described in Chapter 3 and Chapter 4, were then characterized using techniques described in Chapter 6. Most of our characterization effort was centered around the graphene devices. Some properties, such as resonant frequencies and Q-factor, of similar graphene devices have been characterized by other groups as well [111, 112, 113, 114, 115, 61].

## 7.1 RESONANT FREQUENCIES

As described in Chapter 4, usually we had quite a few fabricated devices on our samples. To look for resonances of a specific device, I usually started by looking for light scattered off the sample surface (reflection scan) or low-frequency film movement (film-movement scan) on the whole sample.

- For the reflection scan, two different methods were used - One, an SRS synthesizer was used to drive an optical chopper (Thorlabs: MC2000) in the input beam path. The detected beam from the experiment was amplified using an Avalanche Photodiode (APD) (mentioned in Chapter 6) and used as the input of the lock-in amplifier, the reference for which was taken from a reference output of the chopper controller. Two, the usual signal detection scheme was employed (as mentioned in Chapter 6), with a bias-T on the output of APD - the ac signal from this was used for resonance detection (passing through the usual electronics chain) and the dc signal was uses as the auxiliary input of the lock-in, the output of which was recorded as the reflection off the sample surface.

- For the film-movement scan, a large area of the sample was spatially scanned while driving at a fixed frequency below resonance (100 kHz) using an SRS synthesizer, a reference output of which was used as the reference for the lock-in amplifier. The optical signal from the experiment was then fed into the APD, and the output of the APD was directly used as the input of the lock-in amplifier, without any down or up conversion or noise reduction electronics.

The purpose of the reflection scan was to get an estimate of the topology of the sample surface, and broadly recognize the placement of the devices on the sample. The film-movement scan helped recognize the areas of the film getting electrical signal and oscillating, at low frequencies. Such areas, including devices and arbitrary patches of film, were then individually inspected at higher frequencies for possible device resonances. For the drumhead resonators with PMMA as the support, reflection scan showed much more intense scattering from PMMA than graphene, as shown in Fig. 45(d). For such areas, a masked film-movement scan was generated, which would mask out regions of high-scattering, for better visibility of the graphene areas. Fig. 45 shows examples of such scans.

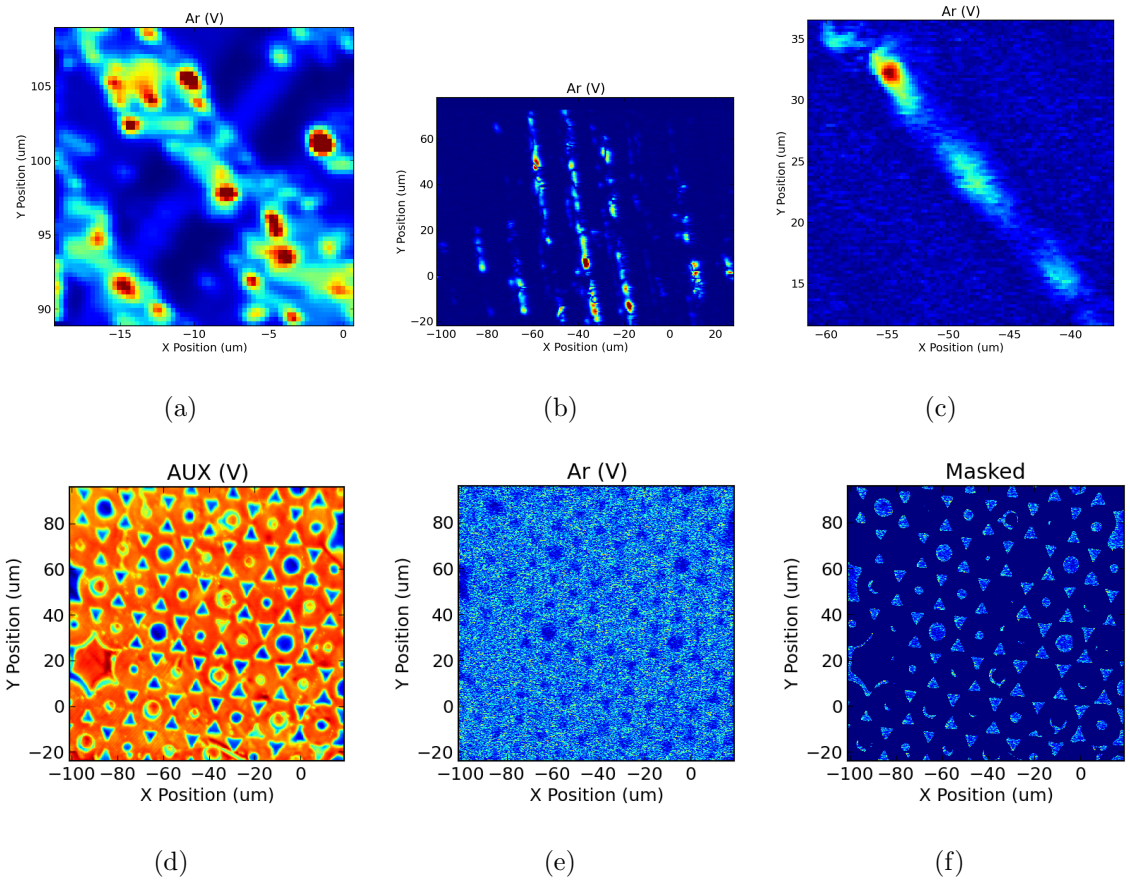


Figure 45: Examples of reflection and film-movement scans on bridges and drumhead resonators (a) and (b) Reflection and film-movement scan of an arbitrary area on a sample with bridge devices, respectively and (d) and (e)with drumhead resonators, respectively, (c)Film-movement scan over one groove of a sample with bridge devices and (f)The same drumhead sample region with high-scattering areas masked to increase the visibility of the graphene film areas.

After recognizing areas on the sample surface with useful devices using scans such as shown above, I would inspect individual devices for resonant frequencies. This was done by spatially parking at a probable device on the sample and sweeping the drive frequency while monitoring the amplitude response of the probable device. Using this methodology, I was able to characterize the frequency response of several bridge and drumhead devices on our samples. The resonant frequency response of two of these devices is shown in the

figure below. Also shown is the spatial response at the resonant frequency of the device shown in the reflection scan Fig. 45(a). Characterizing our devices in this fashion gave us a range of resonant frequencies between 2-25 MHz for bridge devices, while their lengths varied between 1-6 $\mu$m and their widths varied betweem 1-4$\mu$m. Similarly, for drumhead resonators, I obtained resonant frequencies between 6-8 MHz for drum diameters between 2-8 $\mu$m.

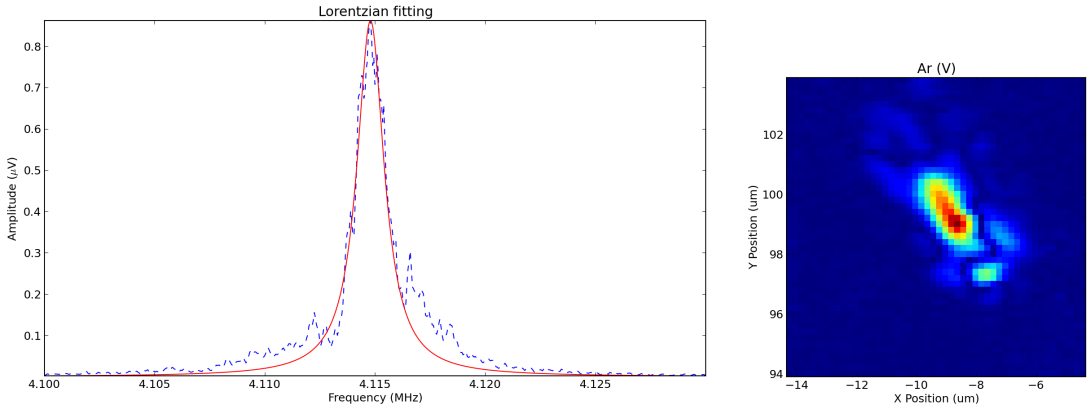


(a) (b)

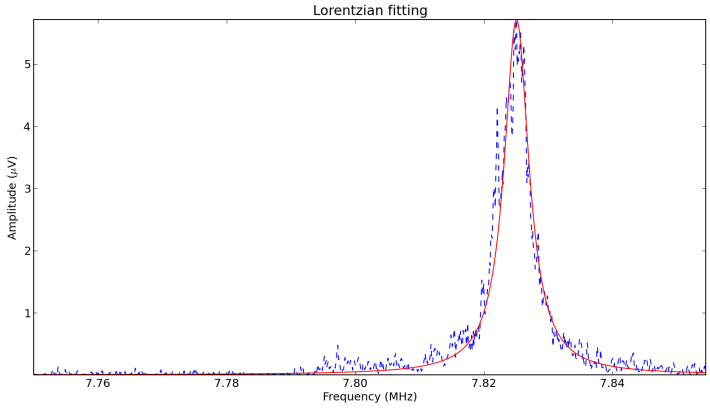


(c)

Figure 46: Examples of frequency and spatial scans of resonances on bridge and drum devices (a)Frequency Resonance at ≈4 MHz seen on a bridge device, (b)Spatial scan of a bridge device shown in Fig. 45(a) at its resonance frequency and (c)Frequency Resonance at ≈7.8 MHz seen on a drumhead resonator.

## 7.2 Q-FACTORS

Quality factor (or Q-factor) is an important metric of performance of a resonator. This dimensionless parameter is defined as

$$Q = 2\pi \times \frac{\text{Energy stored}}{\text{Energy dissipated per cycle}} = \frac{\omega_0}{\Delta\omega}, \tag{7.1}$$

where $\omega_0$ is the resonant frequency of the oscillator and $\Delta\omega$ is the full width half power maximum (FWHM) of the Lorentzian response of the power (amplitude squared) of the oscillator.

The Q-factor of a resonator can be thought of as a measure of damping of the resonator. The higher the Q-factor, lesser the loss of energy from the oscillator, or lesser the damping. Another way to think of the Q-factor is that it is a measure of the purity of frequency of oscillation. The higher the Q-factor, narrower the resonance peak in frequency space.

The Q-factor of graphene resonators reported by other groups varies from 50-2400 at room temperature for ribbon-like and drumhead devices. At lower temperatures, the Q-factor have been shown to be as high as 100,000 [115]. For our devices, I measured the Q-factors to be between 700-2700 for bridge devices and between 1000-1500 for drumhead devices, for temperatures below 10K. Though the Q-factors measured on our devices were not abnormal, they were a bit lower than that reported by other groups. I suspect this was so because of the following reasons:

- Maybe the edges of our devices were not as crisp as that of others, thus making them floppier and more prone to loss of energy. We tried fabricating and detecting drumhead resonators to fight this issue. But, the drumhead resonators also showed similar Q-factors.
- Maybe our method of transfer, substrates of transfer or the actuation scheme led to transfer of energy between devices, thus leading to loss of energy and lower Q-factors.
- Maybe in our devices, we were observing a lot of mixing of frequency modes, thus increasing the resonance bandwidth and leading to lower Q-factors. In other words, the methodology of calculating the Q-factor by measuring the FWHM of the Lorentzian

power response of the devices, is not a reliable way if there is a lot of mixing of modes. This could also have been the reason for the instability of our devices as explained in the next section. We were not able to answer why we might have been getting this mixing of modes.

## 7.3 PHASE/FREQUENCY NOISE

One very important characteristic of the resonance frequency of the devices for our purposes, was the stability of this resonance. As discussed in Chapter 2, the strength of coupling between the NMO and the NV center was expected to be ≈1-1000 Hz, and could have been as high as 4 kHz under ideal conditions. This would have meant that if an NMO was well coupled with an NV center, a jump of the order of the coupling strength would have been seen in the resonant frequency of the NMO. Whenever the NV center underwent a spin transition. Thus, after characterizing the resonant frequency of the NMO, we started monitoring the time-stability of this frequency. It was important that the NMO's resonant frequency was more stable over time than the order of expected jumps. We realized that the frequencies of our NMOs were not stable to within these limits.

We inspected the stability of the resonant frequencies in a few different ways:

- *Monitor frequency over time* This was the first kind of monitoring we did of the resonant frequencies of the NMO devices. Using the lock-in, we directly monitored the amplitude of the two quadratures of the resonance over a long span of time. We used this information to further monitor the phase of the oscillator. Further, using the Q-factor of the oscillator, we converted this phase instability into frequency instability of the oscillator. A plot showing these instabilities over >12 hours is shown below. Monitoring this way we realized that the frequencies of our oscillators were unstable within 100-2000 kHz.

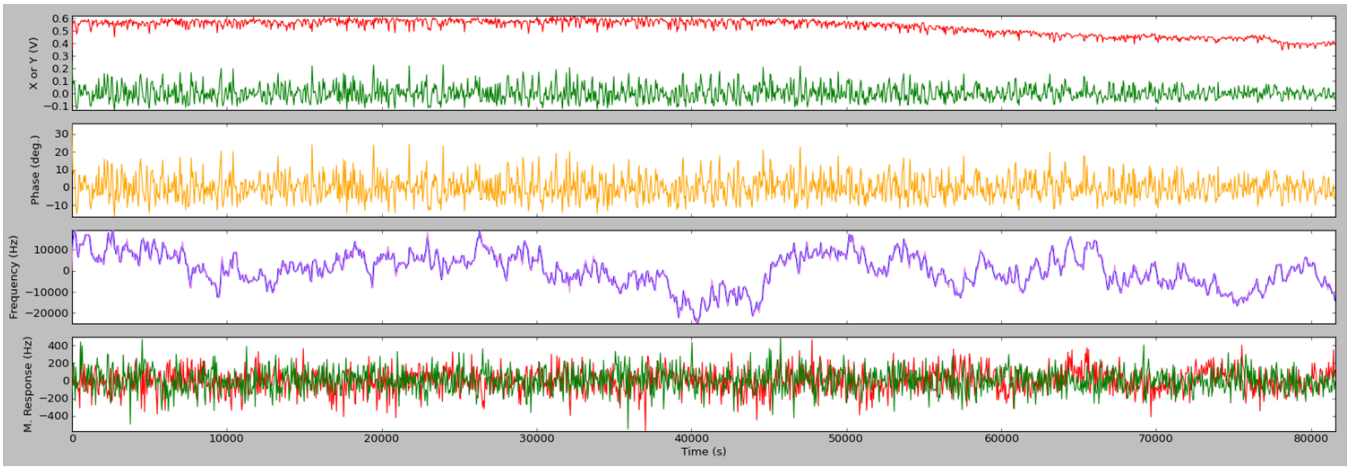


Figure 47: Monitoring the quadrature amplitudes, phase and frequency of the NMOs at resonance, over long spans of time, shown instability to within 100-2000 kHz

- *Fourier Transform* This monitoring was done to track any phase-coherent noise on the device resonance. In this control, we extract the device response in the two quadratures from the lock-in amplifier, while driving it at a fixed frequency. We then 'fast frequency transform' (FFT) this complex signal, keeping the driving frequency always at 0 Hz. We were hoping to see peaks in this fft, if there was a phase-coherent noise source. At times I did see peaks at 30 Hz, and its higher harmonics, which indicates leaking of some noise from the power lines, maybe through the dc power supply. Plots from this control are shown below, in linear and log scale.

  Using the linear and log fft scans, we confirmed that our oscillators were as unstable as expected, and the noise had a 1/f-like spectrum. As can be seen with the above scans, some devices were better than the others, with the frequency noise not extending beyond 10 Hz, while for the others it could extend to >1 kHz. Using above scans, we also concluded that annealing our devices with laser (either spurts of heating or scanning over slowly at high power) decreased the frequency noise.

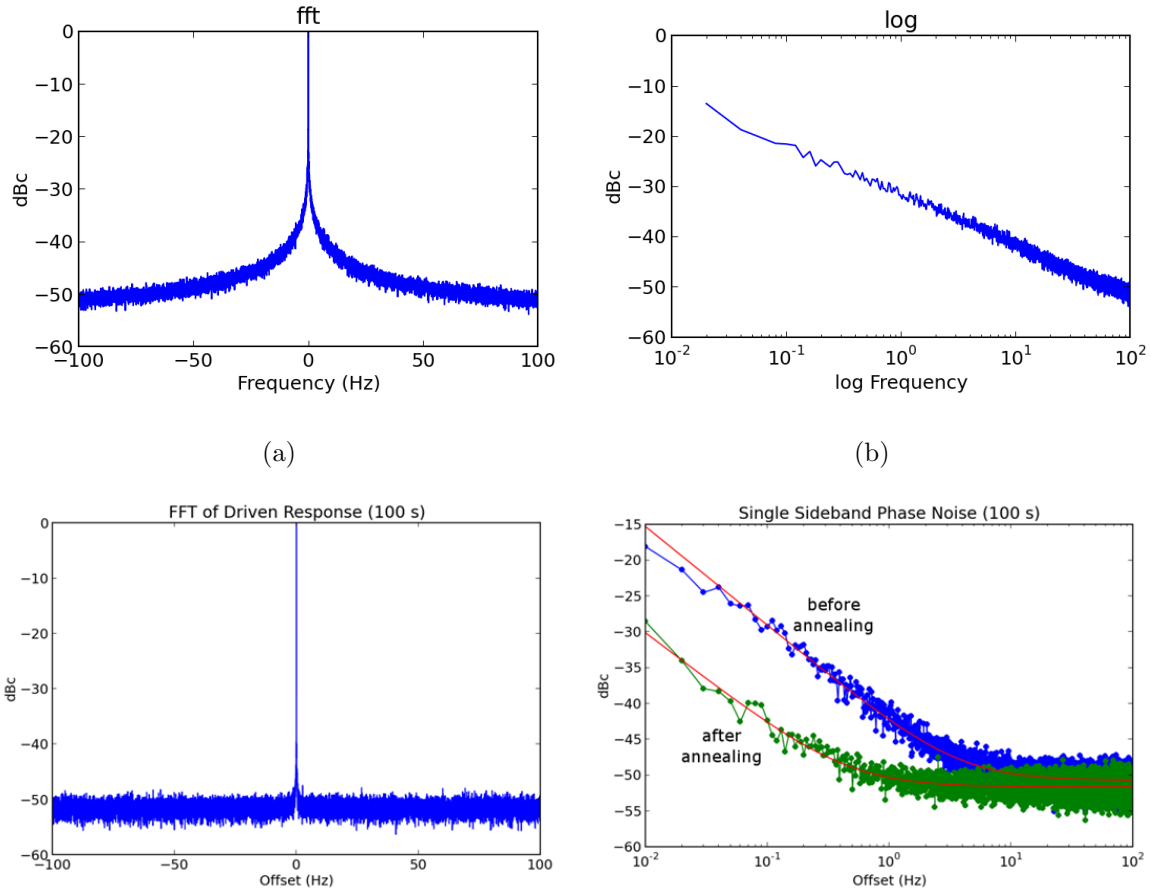


(a) (b)

(c) (d)

Figure 48: Monitoring the noise in the oscillators by taking the Fourier transform of the signal (a) and (b)Fourier transform of a general device shows a lot of frequency noise on it - plotted in linear and log scale, (c) and (d)One of the devices with lowest noise, which shows the decrease of noise with annealing

- *Correlation plots with possible causes* While trying to understand the possible cause(s) of the phase/frequency noise in the oscillators, we tried plotting voltage signals from such cause(s) on a phase plot with the device amplitude signals, to look for a possible correlation. Plausible causes for the device's frequency noise could have been: Electronics (such as ac drive, DC drive, amplifier and filters etc.), Optics (such as laser intensity, laser wavelength, lenses and mirrors etc.), temperature fluctuations, inherent device noise

(such as electronic noise in graphene) etc. Two such correlation plots are shown below, and unfortunately, none such plots helped us with identifying the main cause of noise in the oscillators.

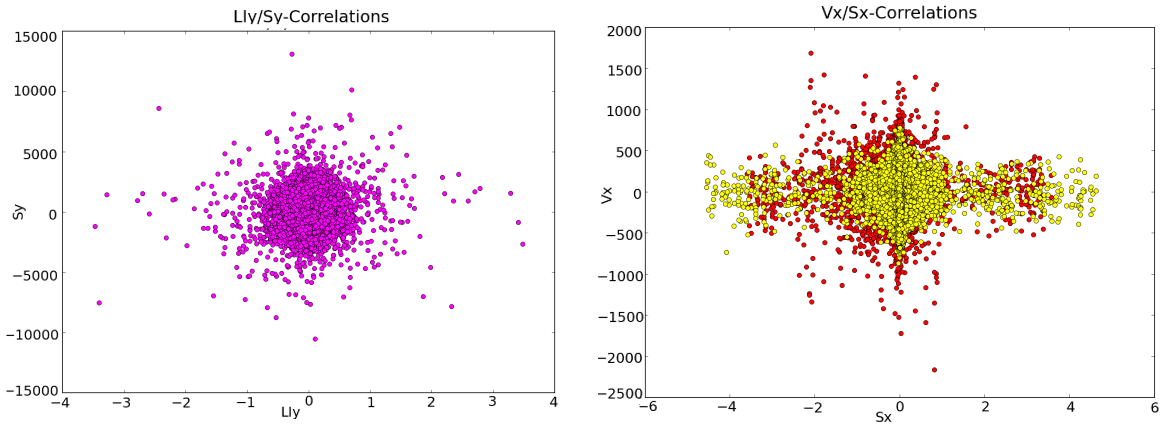


(a) (b)

Figure 49: Correlation plots between possible noise sources and device amplitudes were plotted (a)shows correlation between one phase of laser intensity and device amplitude and (b)shows correlation between drive voltage and one phase of device amplitude Such plots showed no significant correlation between the device amplitudes and possible sources of noise.

Using the above techniques for NMO characterization, we realized that trying to look for the NMO-NV coupling with our present toolkit would have been like looking for a needle in a haystack, cause of the following reasons:

- The frequency instability could easily have been much more than the coupling strengths for most of the devices.
- The direction of the NV center(s) on any arbitrary device could have been in any direction, and lookin for coupling without knowing that direction exactly would have been very hard.

Because of these two reasons, we decided to characterize the NV center(s) in any arbitrary diamond nanocrystal, at least so that we would have known the direction of the NV on any device before probing it for coupling.

# 8.0 NV CHARACTERIZATION

## 8.1 INTRODUCTION

Nitrogen vacancy (NV) centers in diamond are naturally occurring defects in diamond, which consist of a substitutional nitrogen atom and an adjacent carbon vacancy [26]. These defects can also be artificially introduced in diamonds through irridiation and annealing [25, 110]. Owing to their ease of manipulation and readout, and long coherence times, even at room temperature, they have recently being extensively characterized and used in myriad of applications [110]. One such application of NV centers is as a sensor for dc, ac and fluctuating magnetic fields [116, 52, 37, 36, 117, 118]. The work done in this regard has shown that the NV centers can be used to detect nanotesla magnetic fields with nanoscale spatial resolution [36], can be used for these purposes at room temperature [37], and an array of them can be used to map out the magnetic fields in a two-dimensonal area [117]. Most of these applications choose the NV center aligned in the direction of the external magnetic field [36] or they detect the component of the magnetic field that is aligned in the direction of the NV center [52]. For the applications that do detect magnetic fields that are not aligned with the direction of the NV center have to do so by iteratively fitting parameters and minimizing error functions [117]. Due to these limitations, the maximum magnetic fields measured by such techniques gets limited to $\leq$10 mT[37, 117].

Recently, a variety of hybrid systems, involving mechanical oscillators coupled with spin systems [8, 19, 42], are being studied and used for characterization of quantum properties of their components. With the advent of such systems, a class of measurement known as quantum nondemolition (QND) is re-emerging. Since the introduction of QND measurements [38, 7], this measurement class has found use in a wide variety of physics applications such as gravitational-wave detection [119], weak force detection using harmonic oscillators [120], optics [121] etc. A QND measurement scheme allows repeated quantum measurements to be made on the system by reducing back-action of such measurements onto the system. In a previous work, we proposed a hybrid system comprising of a nanomechanical oscillator (NMO) coupled to an NV center in presence of an external magnetic field [42]. This hybrid system results in quadratic coupling between the NMO and the NV center, which allows us to use a QND measurement scheme [120] on the system to discern

quantum behavior of the NMO using NV center as a probe.

The quadratic coupling in this system results from NV-containing diamond nanocrystals physically placed on top of the NMO undergoing torsional mode of oscillation. Under these conditions, in presence of an external magnetic field, the NV center gets coupled to the angle of oscillation ($\theta$) of the NMO in a quadratic manner around $\theta = 0$ (the linear coupling is negligible in this regime). This $\theta^2$ coupling occurs due to mixing of the spin states ($S_z$ with $S_x$ or $S_y$) of the NV centers, unlike previous works in which the $S_z$ spin state of the NV is used to detect the component of the magnetic field along the same direction [52]. For all such schemes which involve measuring only the component of the magnetic field aligned with the direction of the NV ($\cos(\theta)$ component), the NV center can be thought of as $\theta^2$ sensor, with its sensitivity increasing linearly with increasing the measured magnetic field. In our QND scheme, the NV center acts as a $\theta^2$ sensor, with its sensitivity increasing much faster than linearly with the measured external magnetic field.

In this work, we demonstrate how to identify the direction of NV centers by applying an external magnetic field around them. We further use this ability to experimentally verify that the NV center is indeed a great $\theta^2$ sensor, the sensitivity of which agrees with the theoretical predictions made in a previous work [42].

## 8.2 THEORY

The energy structure of the NV center's ground state has been extensively studied [26, 110], and is understood to be as shown in Fig. 50. As can be seen from this figure, the ground state ($^3A$) is a spin triplet, with $|0\rangle$, $|1\rangle$ and $|-1\rangle$ as eigenstates, defined in the $S_z$ basis (along the $NV - \hat{z}$ axis), where state $|i\rangle$ has $m_s = i$. In absence of any external magnetic field, the $|1\rangle$ and $|-1\rangle$ states are degenerate, with a zero-field splitting of $\Delta = 2.87$ GHz above the $|0\rangle$ spin state. In presence of an external magnetic field, the degeneracy between the $|1\rangle$ and $|-1\rangle$ states is lifted by amounts proportional to the external field.

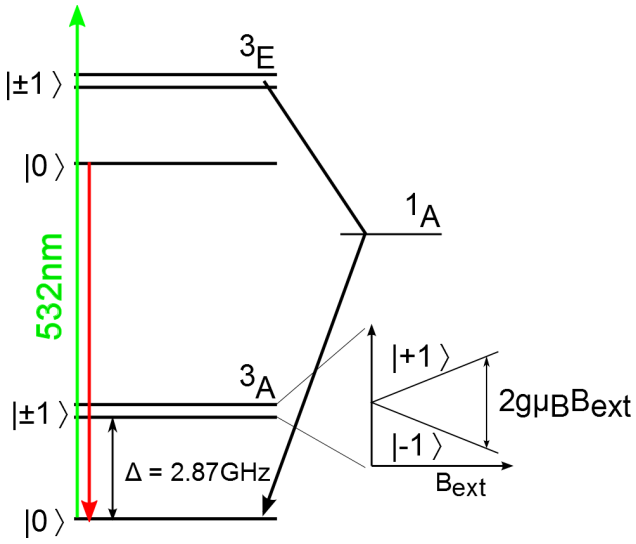


Figure 50: Energy structure of the ground state of the $NV^-$ center.

The Hamiltonian for the ground state of the NV center can be written as [30, 52]:

$$H_{NV} = \hbar \Delta S_z^2 + g\mu_B \left( \vec{S} \cdot \vec{B}_{ext} \right), \tag{8.1}$$

where $\Delta$ is the zero-field splitting, $g \approx 2$ is the electron g-factor in the NV center, $\mu_B$ is the Bohr magneton, $\vec{S}$ is the electronic spin of the NV center and $\vec{B}_{ext}$ is the external magnetic field.

In our experiment, at any instant in time, the applied magnetic field $\vec{B}_{ext}$ could be at an arbitrary angle with respect to the NV spin vector $\vec{S}$. This gives the term $\vec{S} \cdot \vec{B}_{ext}$ in Eq. 2.4 an angular ($\theta$) dependence, where $\theta$ is the angle between $\vec{B}_{ext}$ and $\vec{S}$. For this work, we fix the direction of the NV center, and vary the external magnetic field around on a spherical axes system. For the NMO-NV proposed hybrid system [42], we would fix the direction of magnetic field, and the direction of the NV center would move around due to the oscillation of the NMO. In either case, $H_{NV}$ takes the following form, where we assume a $\vec{B}_{ext}$ and $\vec{S}$ to be in the same plane

$$H_{NV} = \hbar \Delta S_z^2 + g\mu_B B_{ext} \left( S_y \sin\theta + S_z \cos\theta \right). \tag{8.2}$$

Further analyzing the Hamiltonian of the NV center, by finding the eigenvalues of $H_{NV}$ with $\theta$ as a parameter, we see the eigenvalues $\lambda_i(\theta)$ have the following form

$$\lambda_i(\theta) = \hbar\omega_i + \kappa_i\theta^2 + O(\theta^4), \tag{8.3}$$

where $i = -1$, 0, or $+1$ is a label which is equivalent to the NV center $m_s$ when $\theta = 0$. In the $\theta$-independent term in $\lambda_i(\theta)$, $\hbar\omega_i$ is simply the result of combining the zero field splitting with the static external field at $\theta = 0$:

$$\omega_{\pm 1} = \Delta\left(1 \pm B_{ext}/B_{zfs}\right), \tag{8.4}$$

$$\omega_0 = 0, \tag{8.5}$$

where $B_{zfs} = \hbar\Delta/g\mu_B \approx 102.5$ mT is the magnitude of the effective internal magnetic field which results in the zero field splitting $\Delta$. As a vector, $B_{zfs}$ can be thought of as being along the axis of the NV center. By writing the $\theta$-independent term of the eigenvalues of $H_{NV}$ in the above form, we can clearly see that on applying an external magnetic field, the degeneracy between $|1\rangle$ and $|-1\rangle$ states is broken, and the energy gap between $|0\rangle$ and $|-1\rangle$ decreases, and between $|0\rangle$ and $|1\rangle$ increases.

The $\theta^2$ coefficient in $\lambda_i(\theta)$, $\kappa_i$, for the three NV spin states, namely $|0\rangle$, $|1\rangle$ and $|-1\rangle$, is:

$$\kappa_{\pm 1} = -\hbar\Delta\tfrac{B_{ext}}{2(B_{ext}\pm B_{zfs})}, \tag{8.6}$$

$$\kappa_0 = \hbar\Delta\tfrac{B_{ext}^2}{B_{ext}^2 - B_{zfs}^2}. \tag{8.7}$$

This gives us an analytical form for the energy gap between $|0\rangle$ and $|-1\rangle$, and $|0\rangle$ and $|+1\rangle$ spin states, near $\theta = 0$, as $\kappa_0-$ and $\kappa_0+$, respectively, as shown below:

$$\kappa_{0-} = -\hbar\Delta\tfrac{(B_{ext})(3B_{ext}+B_{zfs})}{2(B_{zfs}^2 - B_{ext}^2)}, \tag{8.8}$$

$$\kappa_{0+} = -\hbar\Delta\tfrac{(B_{ext})(3B_{ext}-B_{zfs})}{2(B_{zfs}^2 - B_{ext}^2)}. \tag{8.9}$$

The eigenvalues, $\lambda_i(\theta)$, of $H_{NV}$ for $i = 0$ and $-1$, are plotted below for three different external magnetic field values. The energy gap between these spin states is also plotted for the same magnetic field values. As can be seen from Fig 2(b), the curvature of the

energy gap between spin states $|0\rangle$ and $|-1\rangle$ increases with the increase of the external magnetic field. This shows that the sensitivity of the NV center as a $\theta^2$ sensor increases with increasing magnetic field. Also looking at the figure, one can see a sharp nonlinear dependence of the energy gap between these spin states around $\theta = 0$, which is the result of an avoided level crossing between these states when $B_{ext}$ approaches $B_{zfs}$. This results in making the sensitivity of the NV center as a $\theta^2$ sensor increase more than linearly with increasing magnetic field, and diverge when $B_{ext}$ approaches $B_{zfs}$. In this work, we have tried to experimentally verify these theoretical predictions about the NV centers.

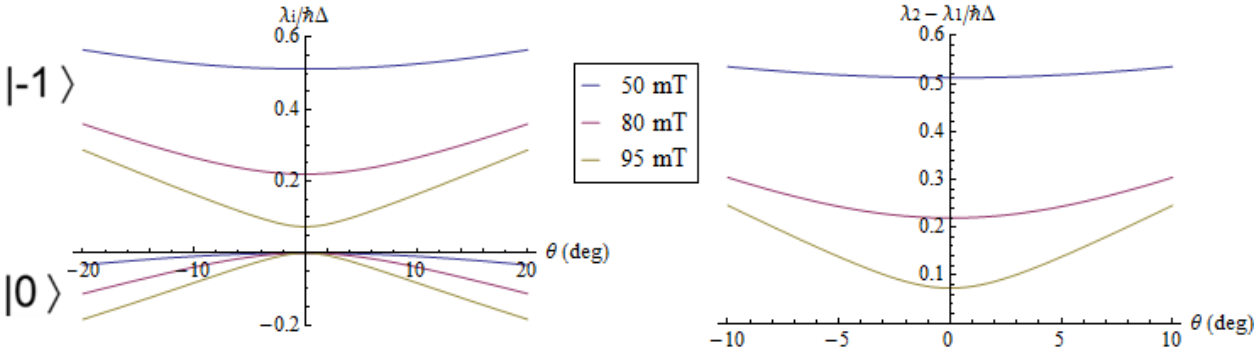


Figure 51: Considering only $|0\rangle$ and $|-1\rangle$ spin states: Eigenvalues of $H_{NV}$ and their energy gap, at different magnetic fields

## 8.3 EXPERIMENTAL DATA

To verify the above-mentioned theoretical predictions, electronic spin resonance (ESR) was performed on diamond nanocrystals with NV ensembles. The nanocrystals used for this purpose were ∼100 nm in diameter and were prepared using high pressure high temperature (HPHT) techniques (Adámas Nanotechnologies: ND-NV-100nm (400NV)). I spin-coated them on a polished piece of silicon, with a density low-enough to be able to resolve individual nanodiamonds. Confocal laser scanning microscopy (CLSM) was employed to visualize and detect the fluorescence of the nanocrystals. Green laser light ($\lambda$ = 532 nm, 2-20 mW) was used to excite the NV centers in these nanocrystals and their fluorescence was detected

by cutting out wavelengths between 517 nm and 548 nm, using a notch filter. To drive resonant transitions between $|0\rangle$ and $|\pm1\rangle$ spin states, a microwave (MW) drive ($\sim$20 dBm) was applied to this sample using an un-terminated loop, 2-3 mm in diameter, made out of 30 $\mu$m diameter tungsten wire (for more details of the optics and electronics used, refer to Appendix A). This resulted in a dip in fluorescence at the frequency corresponding to the energy gap between the $|0\rangle$ and $|\pm1\rangle$ spin states i.e. $\sim$2.87 GHz. This is the characteristic ESR signal as expected from single NV centers or NV center ensembles [122, 37, 110]. ESR signals from three such diamond nanocrystals on our sample is shown in the figure below, as can be seen the ESR dip depth obtained was $\sim$1-5% lower than the base counts. The breaking of the ESR dip into two dips shows the presence of strain and breaking of axial symmetry, again as expected for NV center ensembles [122].

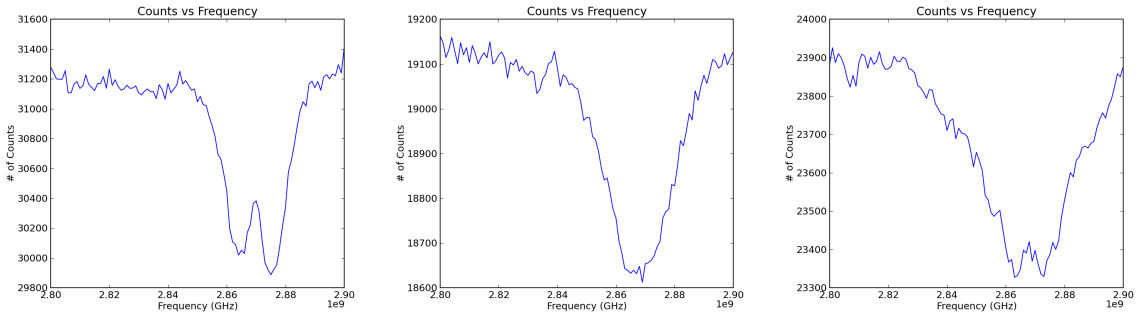


Figure 52: Optically detected ESR signal from three diamond nanocrystals, containing NV center ensembles, on our sample. All three show ESR dips $\sim$2.87 GHz in absence of any external magnetic field, as expected.

Before taking the ESR data in our lab, I took some of this data in Dr. Gurudev Dutt's lab. This was done using the silicon piece with the same diamond nanocrystals as described above, the same tungsten loop to apply MW, and the same Thorlabs objective as on our setup. Using their setup, I got $\sim$10% ESR dips in fluorescence. The input MW power going to the sample, using their amplifier, was $\sim$12 dBm, which was lower than the input power on our setup. I was never able to understand why the dips from our setup were weaker than their setup. It might have been related to optical saturation of the nanodiamonds or more effective coupling of the MW power.

To lift the degeneracy between $|\pm 1\rangle$ spin states, I applied an external magnetic field $B_{ext}$ around our sample, using electromagnetic coils. Due to experimental limitations, $\approx \pm 100$ mT was available in the direction perpendicular to the sample ($\hat{z}$), and $\approx \pm 25$ mT in the two directions parallel to the sample surface ($\hat{x}$ and $\hat{y}$). On a $3D$ plot, this accessible region of magnetic field can be though of as a cuboid with square faces of side 25 mT and a height of $\pm 100$ mT, as shown in Fig. 53. This cuboid-shaped region limits the accessible areas of magnetic fields with specific magnitudes, as shown by the shapes inside the cuboid. Full sphere can be accessed for $B_{ext} \leq 25$ mT, but for 25 mT $\leq B_{ext} \leq 100$ mT only spherical caps are accessible, as shown in Fig. 4(a). To account for all possible NV center directions in any arbitrarily-oriented diamond nanocrystal, we can think of the distribution of possible $B_{zfs}$ values as forming a sphere of radius 102.5 mT on the same $3D$ plot.

In a diamond nanocrystal, the direction of any NV center ($NV - \hat{z}$) can be in any one of the four possible orientations along the carbon tetrahedron bonds (shown in blue arrows in Fig. 53). Due to the symmetry between $|1\rangle$ and $|-1\rangle$ spin states, the $NV - \hat{z}$ direction could also be the four orientations directly opposite to the carbon tetrahedron bonds (shown in red arrows in Fig. 53). The direction of the $NV - \hat{z}$ also being the direction of $B_{zfs}$, suggests that for any arbitrary diamond nanocrystal, there are eight possible directions where $B_{zfs}$ and $B_{ext}$ could align with each other. These eight directions define the orientations along which the NV centers could behave as $\theta^2$ sensors.

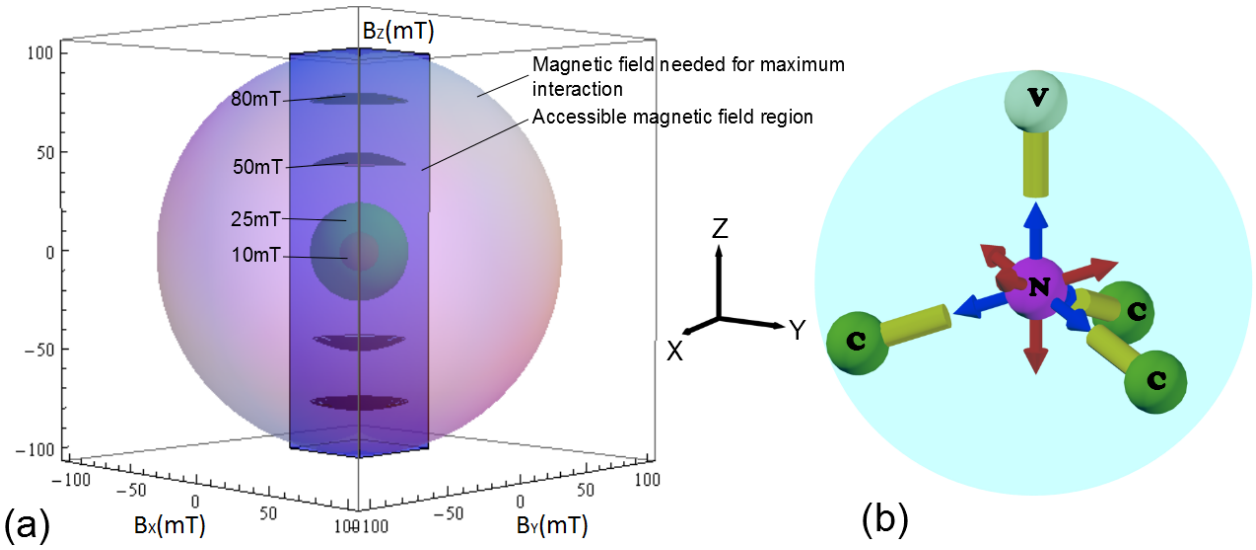


Figure 53: Pictorial $3D$ representation of accessible external magnetic field ($B_{ext}$) and possible NV center orientations (directions of $B_{zfs}$) in any arbitrary diamond nanocrystal (a) The pink sphere represents the direction of possible $B_{zfs}$ for all diamond nanocrystals. The cuboid with square faces of side 25 mT and a height of $\pm 100$ mT represents the experimentally accessible $B_{ext}$. This limits the accessible areas of magnetic fields with specific magnitudes, as shown by the shapes inside the cuboid. (b) A carbon tetrahedron structure in any arbitrary diamond nanocrystal is shown. Assuming the nitrogen atom of the NV center is at the center of the tetrahedron (pink), and one of the other carbon atom (green) sites is vacant (light green), the $NV - \hat{z}$ direction could be in one of four possible orientations (blue arrows). Due to the reversibility between $|1\rangle$ and $|-1\rangle$ spin states, the $NV - \hat{z}$ direction could also be the four orientations opposing the carbon tetrahedron bonds (red arrows).

Our first experimental goal for this work, was to recognize these $NV - \hat{z}$ orientations for any randomly-picked diamond nanocrystal. For this purpose I swept $B_{ext}$ only in the $+\hat{z}$ direction along hemispheres/spherical caps shown in Fig. 53. This would suffice due to the mirror symmetry about the XY-plane of $B_{ext}$ and the NV centers. On applying an external magnetic field, the $|1\rangle$ and $|-1\rangle$ spin states undergo Zeeman splitting, as shown in Fig. 50. Thus the ESR dip, which occurs due to resonant transitions between $|0\rangle$ and $|\pm 1\rangle$ spin states at MW frequencies corresponding to the energy difference between these states, splits into

two dips, as expected. Due to the decrease in energy gap between $|0\rangle$ and $|-1\rangle$, and increase in energy gap between $|0\rangle$ and $|1\rangle$, the corresponding ESR dips are expected to decrease and increase in frequency respectively from 2.87 GHz, on increasing the magnitude of $B_{ext}$. For our purposes, I monitored the ESR dip corresponding to the energy gap between $|0\rangle$ and $|-1\rangle$. The ESR dip shift is expected to be linear in frequency with increasing $B_{ext}$, if the direction of $B_{ext}$ is aligned with the $NV - \hat{z}$ direction.

I monitored the ESR dip depth and frequency location while sweeping a fixed magnitude of $B_{ext}$ around in azimuthal and polar angles about the $\hat{z}$ direction. These plots for a diamond nanocrystal which was $\approx$ 10 $\mu$m away from the edge of the microwave loop are shown in Fig. 54. Similar behavior was observed in other diamond nanocrystals within 20-30 $\mu$m of microwave loop. The colormap for these plots is also shown. Fig. 54(a) and Fig. 54(b) show the behavior of the ESR dip depth and dip location respectively, while sweeping 20 mT magnetic field on a hemisphere. Such plots help us broadly recognize the regions where the ESR dip depth is a maximum and dip location is a minimum, as shown by the circled regions in these plots. These regions can be thought of as orientations of the NV centers in a diamond nanocrystal, where we can hope for them to behave as $\theta^2$ sensors. For the plots shown here, in the space of polar [0-90°]($\phi$) and azimuthal [0-360°]($\Theta$) angles, these regions can be picked as follows - (a)around 50-70° $\phi$ and 90-120° $\Theta$, (b)around the pole of the hemisphere i,e, 0-20° $\phi$ and 250-280° $\Theta$ and (c)around 70-90° $\phi$ and 330-3520° $\Theta$. Due to the experimentally accessible magnetic field region being close to the pole of the hemispheres, I chose location (b) for further exploration. Fig. 54(c) shows the ESR dip at 20 mT at 12.5° $\phi$ and 264° $\Theta$ which, as theoretically expected, is shifted to $\approx$ 2.3 GHz.

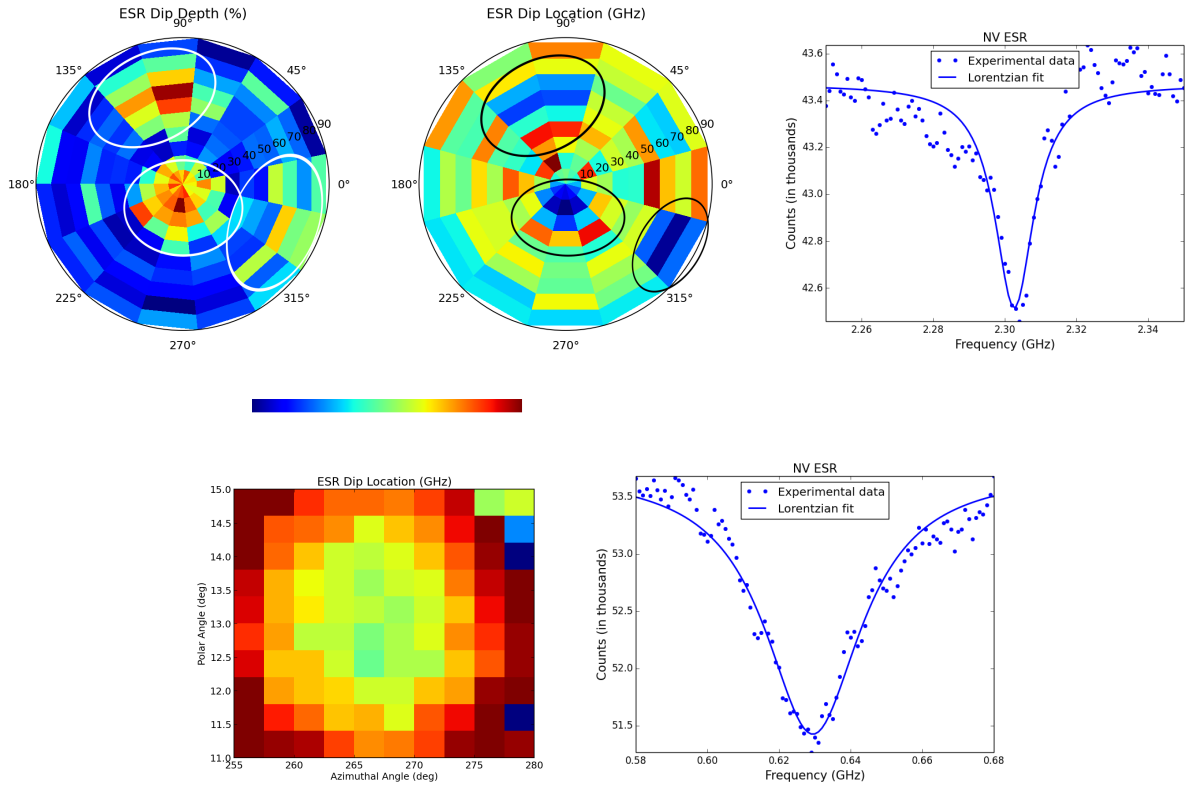


Figure 54: Trying to locate the maximum sensitivity regions for any arbitrarily chosen diamond nanocrystal (a)Monitoring the ESR dip depth at 20 mT $B_{ext}$ while around in azimuthal and polar angles around the $+\hat{z}$ direction and projecting the hemisphere onto a polar plot, (b)Similarly monitoring and plotting the ESR dip location, (c)Maximally shifted ESR dip at 20 mT at a location closest to the pole - 12.5° $\phi$ and 264° $\Theta$, (e)Similarly monitoring the ESR dip location at 80 mT $B_{ext}$ and projecting the spherical cap onto a planar plot and (f)Maximally shifted ESR dip at 80 mT at the same location as above. The colormap for the projection plots is also shown.

After choosing a broad location, such as (b) for this nanodiamond, I tried to narrow down the spread of this region in both $\phi$ and $\Theta$, by probing with higher magnetic fields. Fig. 54(e) shows such a plot of the behavior of the ESR dip location while sweeping 80 mT magnetic field. As can be seen in this plot, the spread of both polar and azimuthal angles narrows down as the external magnetic field is increased. A thing to note in this plot is that

the spread in the polar angle direction is much finer (<5°) than the spread in the azimuthal angle direction (<25°), which is expected for regions around the pole. The shifted ESR dip at 80mT at 13.4° $\phi$ and 267° $\Theta$ is shown in Fig. 54(f) and, as theoretically expected, is around 0.63 GHz.

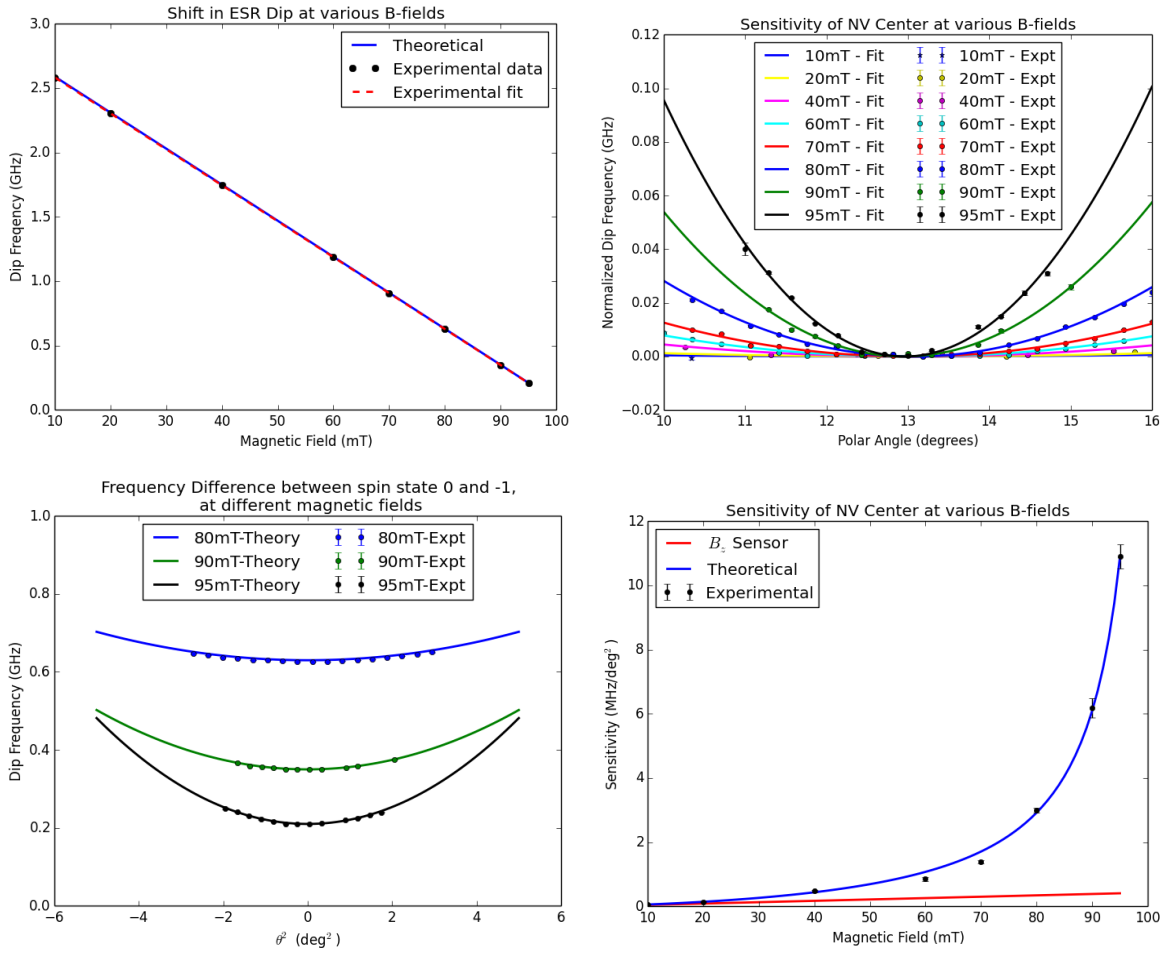


Figure 55: Various trends seen with the shift of ESR dip on applying external magnetic field (a)As theoretically expected, the ESR dip shifts down in frequency linearly with the magnetic field., (b)The ESR dip depth and location have a quadratic behavior with angle, which is plotted here with respect to the polar angle at various magnetic fields, (c)The difference in eigenvalues of $|0\rangle$ and $|-1\rangle$ spin states achieved experimentally agrees very well with the theoretical predictions and (d)Plotting the quadratic sensitivity at different magnetic fields shows that the NV center is a much more sensitive $\theta^2$ sensor than any general $B_z$ sensor.

By fixing $B_{ext}$ at different values between 0-95 mT, and analyzing the shifting of the ESR dip in location and frequency, trends shown in Fig. 55 were observed. As seen in Fig. 55(a), the ESR dip that shifts down in frequency on increasing magnetic field does so linearly. Fitting the experimental data to a straight line, I get an x-intercept of 102.46 mT, which is very close to the expected value of $B_{zfs}$, and a y-intercept of 2.863 GHz, which is very close to the expected frequency of the ESR dip without an external magnetic field. At various magnitudes of $B_{ext}$, I quantitatively explored the variation of the ESR dip depth and location, with respect to both $\phi$ and $\Theta$ angles, and found this variation to be quadratic. I explored this variation with $\phi$ and $\Theta$ iteratively, and for the plots presented here, I fixed the azimuthal angle at its minima (266.5° for the location (b) on this nanocrystal). This quadratic variation was expected from Eq. (8.3), and the variation of the ESR dip frequency (normalized for the plot's vertical-axis) with respect to $\phi$ is plotted in Fig. 55(b). The experimental data (normalized for the plot's horizontal-axis) with the expected theoretical results is plotted in Fig. 55(c), and they seem to be in great agreement. The data presented here was fit to quadratic functions, and the coefficient of the quadratic term at different magnitudes of $B_{ext}$ was noted as the sensitivity of measuring $\theta^2$ at that magnetic field. These experimentally measured sensitivities are plotted in Fig. 55(d) and seem to be in great agreement with the expected theoretical behavior. This experimentally verifies that the NV centers are great $\theta^2$ sensors, the sensitivity for which increases as $B_{ext}$ increases, and diverges as it approaches $B_{zfs}$. As mentioned before, for a general magnetic field sensor, say the NV center measuring the component of the magnetic field along its axis, the sensitivity of measuring $\theta^2$ would be linear, as shown by '$B_z$ sensor' line on plot Fig. 55(d). This clearly shows that if the NV centers' axis is aligned with $B_{ext}$, they can work as great $\theta^2$ sensors.

## 8.4 CONCLUSION

In conclusion, we have developed an experimental scheme to estimate the NV centers' axes in any arbitrarily chosen diamond nanocrystal. We further demonstrated the ability to align an external magnetic field with the direction of the NV center and sweep the external field

around it in a spherical fashion. Using this technique, we have clearly shown that if the NV centers' axis is aligned with $B_{ext}$, they can act as very effective $\theta^2$ sensors, the sensitivity for which increases much faster than linearly with increasing external field. This sensitivity diverges as $B_{ext}$ approaches $B_{zfs} \approx 102.5$ mT, practically limiting the sensitivity. We have also experimentally shown that the sensitivity for this measurement matches perfectly with its theoretical predictions. The ability of the NV centers to be very sensitive $\theta^2$ sensors demonstrates that they can be very effectively used for making QND measurements on systems such as a harmonic oscillator. This class of measurements lends use in a variety of applications such as gravity wave detection and probing quantum behavior of NMOs in a hybrid system.

# 9.0 SUMMARY AND CONCLUSIONS

## 9.1 SUMMARY

In summary, the work done for this thesis can be broadly categorized under Condensed Matter Physics and Quantum Physics. The main crux of this thesis involved a hybrid system consisting of a nanomechanical oscillator (NMO) and a quantum spin system - nitrogen vacancy (NV) center in diamond.

A general introduction of hybrid systems, an overview of our hybrid system and its theoretical analysis is presented in Chapter 1 and Chapter 2.

The first few years of my PhD time and the next two chapters of this thesis deal with the fabrication of the NMO for this hybrid system. The fabrication process of the NMO can be broadly divided into two steps. Firstly, fabrication of the thin films out of which the NMO is made, which is the subject of Chapter 3. For this purpose, I explored the growth of thin films of aluminum oxide and graphene, for the first 2-3 years of my PhD time. The second step included various processes required to fabricate NMOs of various shapes and sizes out of the thin films, which is covered in Chapter 4, which again was going in parallel for 3-4 years of my grad school time. In the last 2 years, a spin-off project came out of the graphene growth - growth of large domain graphene, and in this regard I was able to increase our graphene domain sizes from $\approx$70 $\mu$m to $\approx$4-5 mm. I have been trying to grow arbitrarily large-domain graphene using progressive growth, and this is an on-going project which requires further exploration.

The next two chapters of the thesis, Chapter 5 and Chapter 6, deal with the experimental setups used for the characterization of the hybrid system. These chapters include a description of our home-assembled cryostat, electric and vacuum components inside it, magnetic field coils around it, optical and electrical components outside it - all of which are used to actuate, excite, drive and detect parts of the hybrid system. I designed and assembled almost all the parts of these experimental setups without anyone's help and input, other than Dr. D'Urso's. Almost every piece of the cryostat, from the smallest probe-system to the largest electromagnetic coils, is self-designed and optimized, machined in the department's machine shop, and self-assembled - this took most of the fist 2 years of my PhD. Assembling the optics under the cryostat, on a shelf at the bottom of the optics table, was literally a

backbreaking task (I had to visit several doctors, including an orthopedic, during this time to make sure I wasn't inflicting any permanent damage!), but was as satisfying as well.

The next two chapters of the thesis talk about the characterization of the two parts of the hybrid system, the NMO and the NV center. Chapter 7 talks about the various properties of the our fabricated NMOs that I characterized in the lab, such as frequency, Q-factor and frequency stability. Chapter 8 discusses the characterization of the NV centers as $\theta^2$ sensors, and their ability to make QND measurements on the NMO. These chapters discuss why I couldn't demonstrate the expected coupling between the NMO and the NV, that I had set to achieve. But on the other hand, I was able to show that the NV centers are great QND sensors for mechanical oscillators, which set the path for the future trapping experiments in the lab.

## 9.2 FUTURE OUTLOOK

A lot of the work done for this thesis either has spin-off projects that need further exploration, or implications that require more extensive research than done here. Some such projects and ideas are mentioned below:

- One of the most exciting and biggest project that is partially a part of this thesis is the progressive growth of large-domain graphene. A significant effort has already been put into this idea as mentioned in Chapter 3, and we have made considerable progress but is still far from a complete success. This idea is patent-able and has the potential of making graphene greatly useful for a wide-range of applications in large-scale electronics.
- In this thesis I was able to develop a hybrid system with graphene as an NMO and NV centers. Though, I was able to characterize these two components separately, I was unable to see coupling between the two systems, primarily due to the phase/frequency instability and low-Q of the graphene NMO, as mentioned in Chapter 7. To see the QND coupling between an NMO and NV centers thus requires another material and/or kind of NMO, such as a stiffer graphene NMO, diamond wire with inherent NV centers, carbon nanotube with attached nanodiamonds containing NV centers, or a standalone

diamond nanocrystal as the NMO, again with inherent NV centers. This last approach is being pursued in our lab by Jen-Feng Hsu, for which he is trying to optically and/or magnetically trap a diamond nanocrystal and characterize its behavior, both as an oscillator and a spin system. It would be very interesting to pursue these directions, and other similar ones, to observe QND coupling in such hybrid systems.

- Another interesting project would be to characterize and explore the origins of the phase/frequency noise in the graphene oscillators. A stiffer NMO can be fabricated using graphene, say with corrugations as mentioned in Chapter 3, to investigate if this noise originates due to mode-mixing in graphene. Another idea to try would be to fabricate NMOs out of bilayer/multilayer graphene, so see if the origin of this noise is inherent to the electronic properties of single-layer graphene.

- One sub-project that could not be turned into a publication, and was commonly used throughout this thesis work, was the development of substrates for film transfer, as mentioned in Chapter 4. For this project, we had a theoretical model and the experimental technique, but we were unable to publish it cause of lack of reproducibility of our sputtering system. Maybe another sputtering system could give us better results, or maybe just another person's set of hands and perseverance could do the trick!

## 9.3 CONCLUSIONS

In conclusion, I'd like to thank the reader for making the hours spent in writing this thesis worth the effort. The effort would be justified if anyone uses or learns from the material presented here, even to a small degree.


Figure 56: In Conclusion

# APPENDIX A

# OPTICS, ELECTRONICS AND OTHER INSTRUMENTS

## A.1 OPTICS USED FOR DEVICE DETECTION

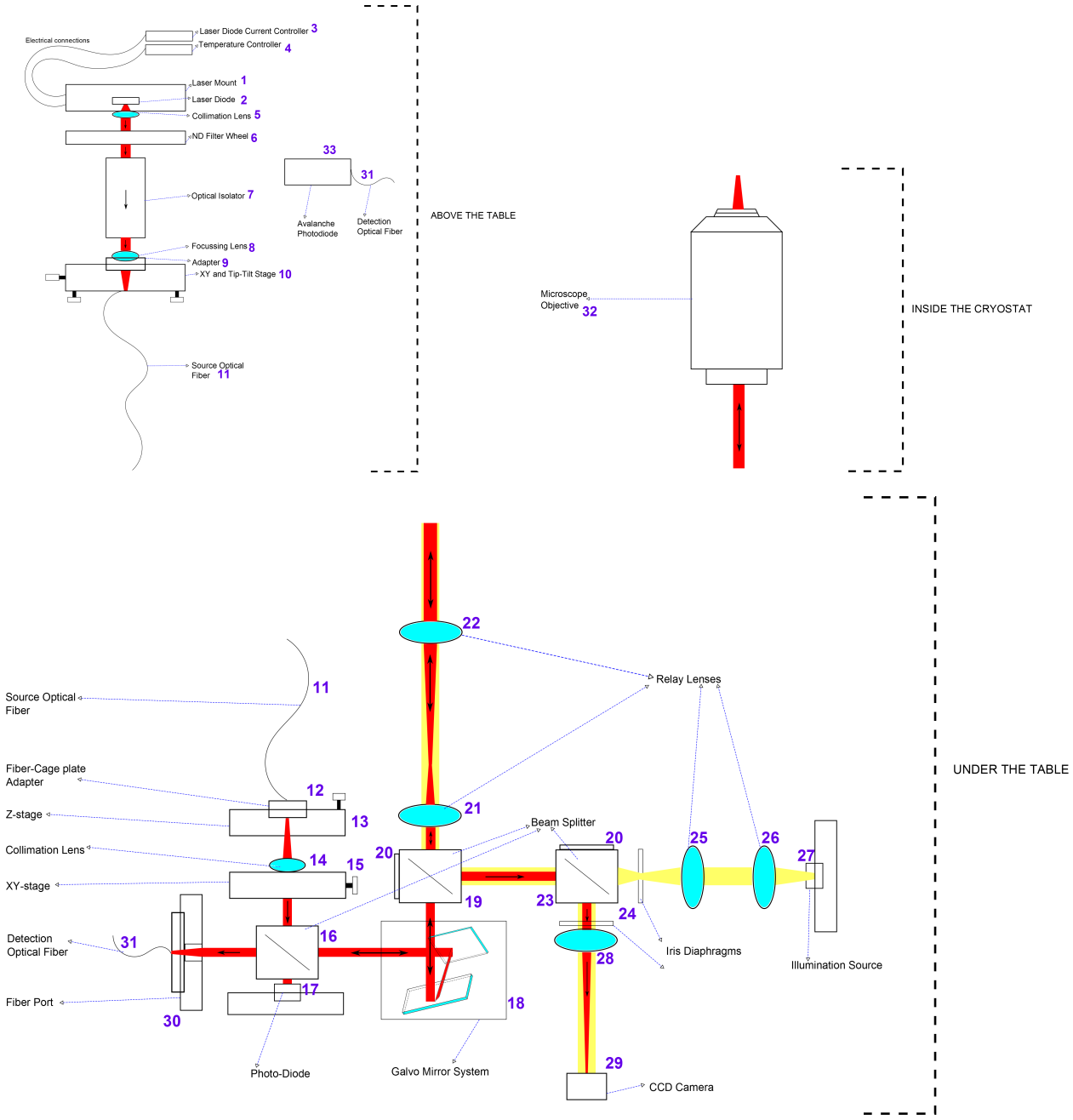


Figure 57: Layout of optics used to detect the motion of the NMO. Refer to Table 9 for numbering reference.

All the optical elements shown here are from Thorlabs, unless specified otherwise.

| S.N. | Component Description | Part Number |
|---|---|---|
| | **ABOVE THE TABLE** | |
| 1 | Laser Diode Mount | TCLDM9 |
| 2 | Laser Diode | HL63133DG [1] |
| 3 | Laser Diode Current Controller | LDC205C |
| 4 | Laser Diode Temperature Controller | TED200C |
| 5 | Collimation Lens | C240TME-B |
| 6 | Neutral Density Filter Wheel | FW1 |
| 7 | Optical Isolator | IO-3-633-LP |
| 8 | Focusing Lens | F240APC-B |
| 9 | Adapter to mount lens into SM1 | AD12F |
| 10 | XY and Tip-Tilt Stage | K6X |
| 11 | APC/PC Polarization maintaining fiber[2] | P5-630PM-FC-2 |
| | **UNDER THE TABLE** [3] | |
| 11 | Source Optical Fiber comes down from above the table | |
| 12 | Fiber to cage-plate adapter | SM1FC |
| 13 | Z Stage | SM1Z |
| 14 | Collimation Lens | C280TME-B |
| 15 | XY Stage | CP1XY [4] |
| 16 | Pellicle 45:55 Beam Splitter | CM1-BP145B1 |
| 17 | Photodiode [5] | SM05PD1A[6] |
| 18 | 2D Large Beam Diameter Galvo System | GVS012 |
| 19 | Pellicle 8:92 Beam Splitter | CM1-BP108 |
| 20 | Caps to reduce reflections | NE20A-A mounted in SM1L03T |
| 21 | Relay Lenses for Laser[7] | AC254-100-A-ML |
| 22 | | AC254-200-A-ML |
| 23 | Pellicle 45:55 Beam Splitter | CM1-BP145B1 |
| 24 | Graduated Ring-Activated Threaded Iris Diaphragms [8] | SM1D12C |
| 25 | Relay Lenses for Illumination Source[9] | AC254-100-A-ML |

| | | |
|---|---|---|
| 26 | | AC254-35-A-ML |
| 27 | Illumination Source - Red [10]<br>Illumination Source - White | CREE XRE-R<br>CREE XRE-W107 |
| 28 | Focusing Lens [11] | AC254-060-A |
| 29 | CCD Color Camera | DCU224C |
| 30 | Fiber Port (comes with Collimation Lens) [12] | PAF-X-18-PC-B |
| 31 | Multimode fiber for Detection | M31L05 |

**INSIDE THE CRYOSTAT**

| | | |
|---|---|---|
| 32 | Objective[13] | Thorlabs - RMS20X<br>20X, 0.4, 1.2 mm, 9.3 mm<br>Partec[14] - 03-0202<br>20X, 0.65, 2 mm, 12 mm<br>Newport[15] - 50102-02<br>36X, 0.52, 10.4 mm, 5 mm |

**ABOVE THE TABLE**

| | | |
|---|---|---|
| 31 | Detection Optical Fiber comes above from under the table | |
| 33 | Avalanche Photo diode | APD110A |

Table 9: List of the optical components used for Detection of NMO

[1]Additional home-made adapter was used to heat-sink the diode in the mount
[2]Held in using adapter SM1FCA
[3]All of these parts are held in a 30 mm cage system
[4]Lens is held in using S05TM09
[5]Optional - if incoming beam needs monitoring
[6]Mounted using CP02 and SM1A6
[7]Held using CP02
[8]Held either using CP02 or SM1V10
[9]Held using CP02
[10]Held using home-made holder - design shown in Fig. 58
[11]Held using SM1V10 and other fixed lens tubes
[12]Held using CP02FP
[13]Specifications - Magnification, Numerical Aperture, Working Distance, Clear Aperture - in that order
[14]Got it with 03-0208 AR coating - Received an additional spec sheet as shown below
[15]Got it customized as shown in the quote below

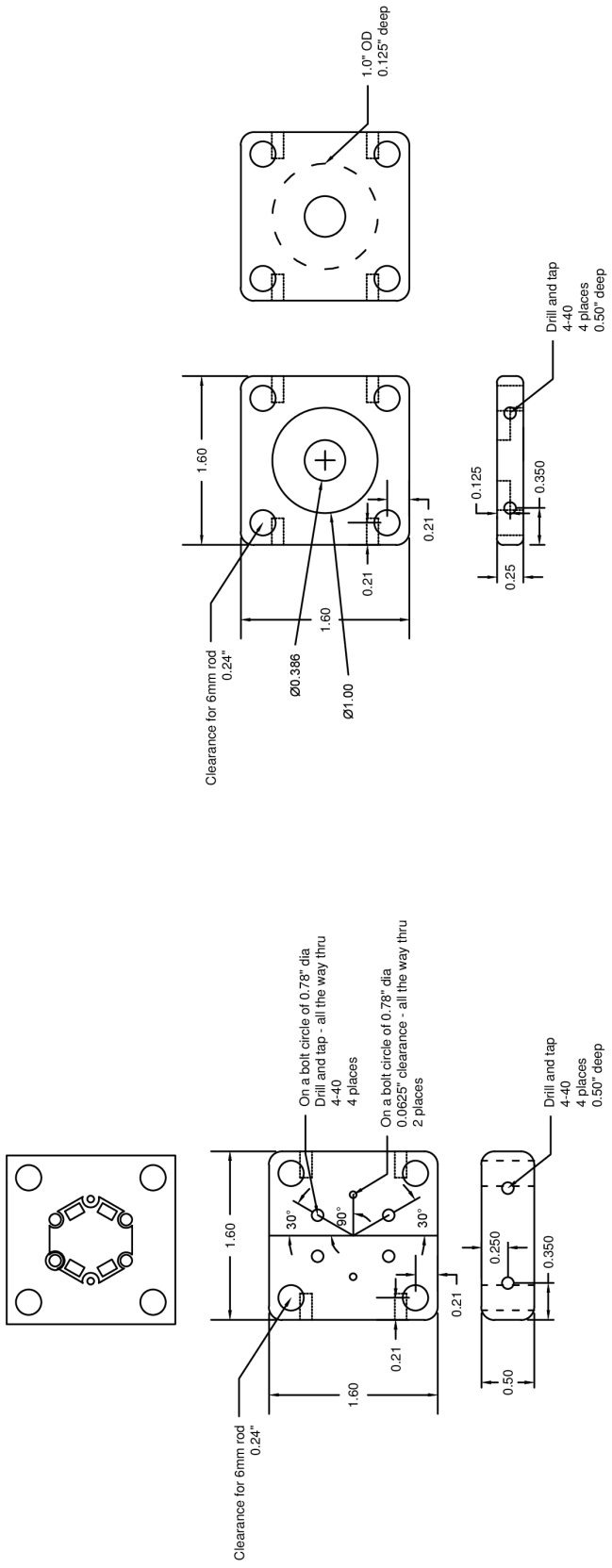


Figure 58: Home-made holder for CREE XRE LED and strain-relieving plate for its electrical connections

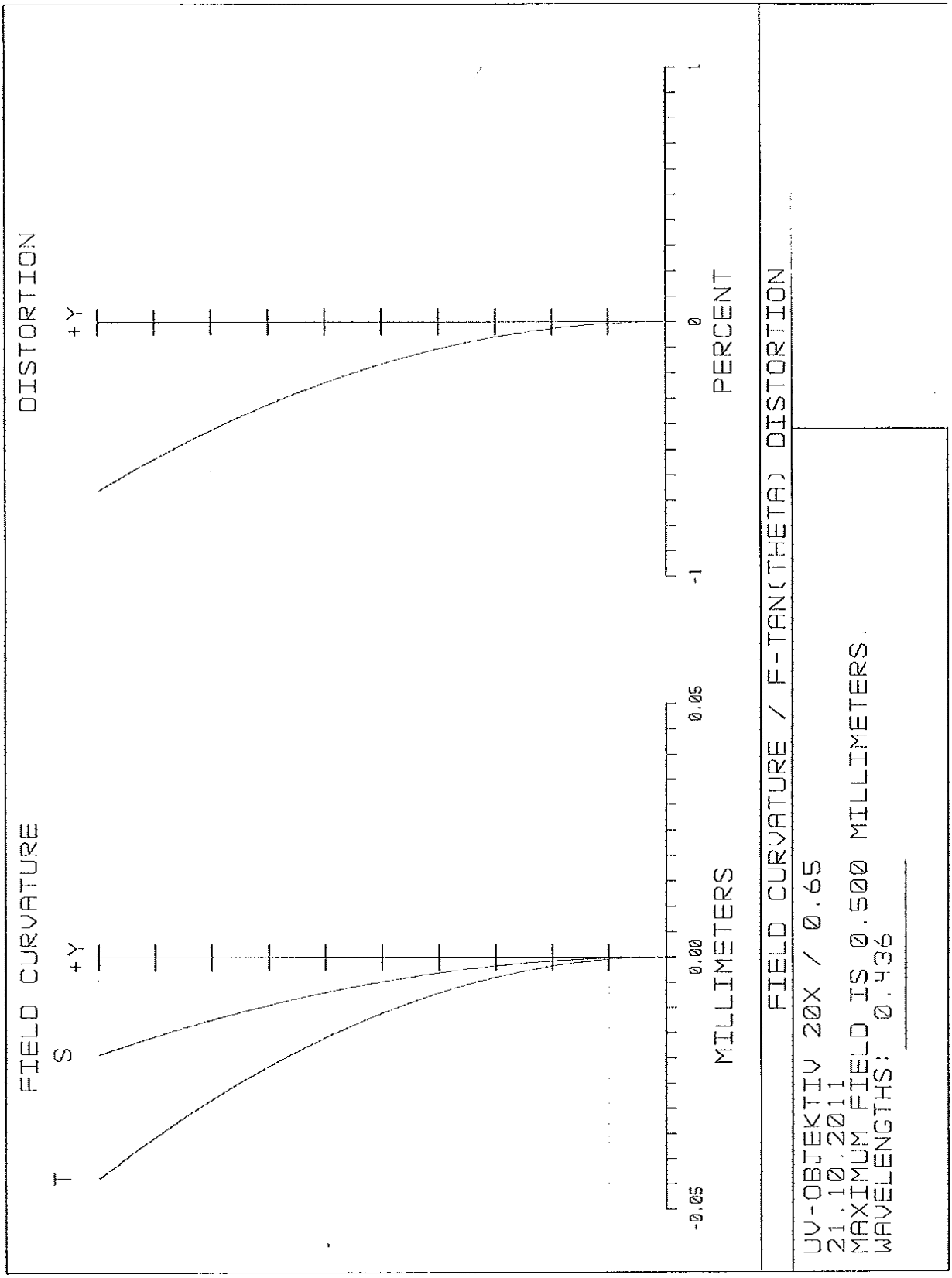


Figure 59: Some specifications of the Partec objective


***Newport Corporation***
8 East Forge Parkway Franklin, MA 02038
TEL. (508) 528-4411 FAX. (508) 520-7583

Newport Quotation No. 16675
Customer Request No.
Date of Request:
Date of Quotation: 8/12/2010
Quotation Valid For: 60 Days
Page 1 of 1

TO: University of Pittsburgh
Department of Physics & Astronomy
3941 O'Hara Street
Pittsburgh, PA 15260

Phone: 412-624-5502
Fax:

FOB: Franklin, MA
Terms: Net 30 Days
Delivery: 8 Weeks ARO

Thank you for your inquiry, we are pleased to quote the following:

| Item | Qty. | Description | Unit Price | | Extension |
|---|---|---|---|---|---|
| 1 | 1 | Custom Microscope Objective, Modified P/N 50102-02<br><br>36X, Infinite BFL, modified as follows:<br><br>1. All screws to be brass.<br><br>2. Screws on the secondary mirror side to be treated as normal during assembly including loctite, epoxy and painting.<br><br>3. Screws on adapter/primary mirror side to have no loctite or epoxy to facilitate easy removal of screws and adapter. | $3,195.00 | | $ 3,195.00 |

Authorized Signature



Figure 60: Customization and Quote for the Newport Reflective Objective

## A.2 OPTICS USED FOR NV DETECTION AND ESR

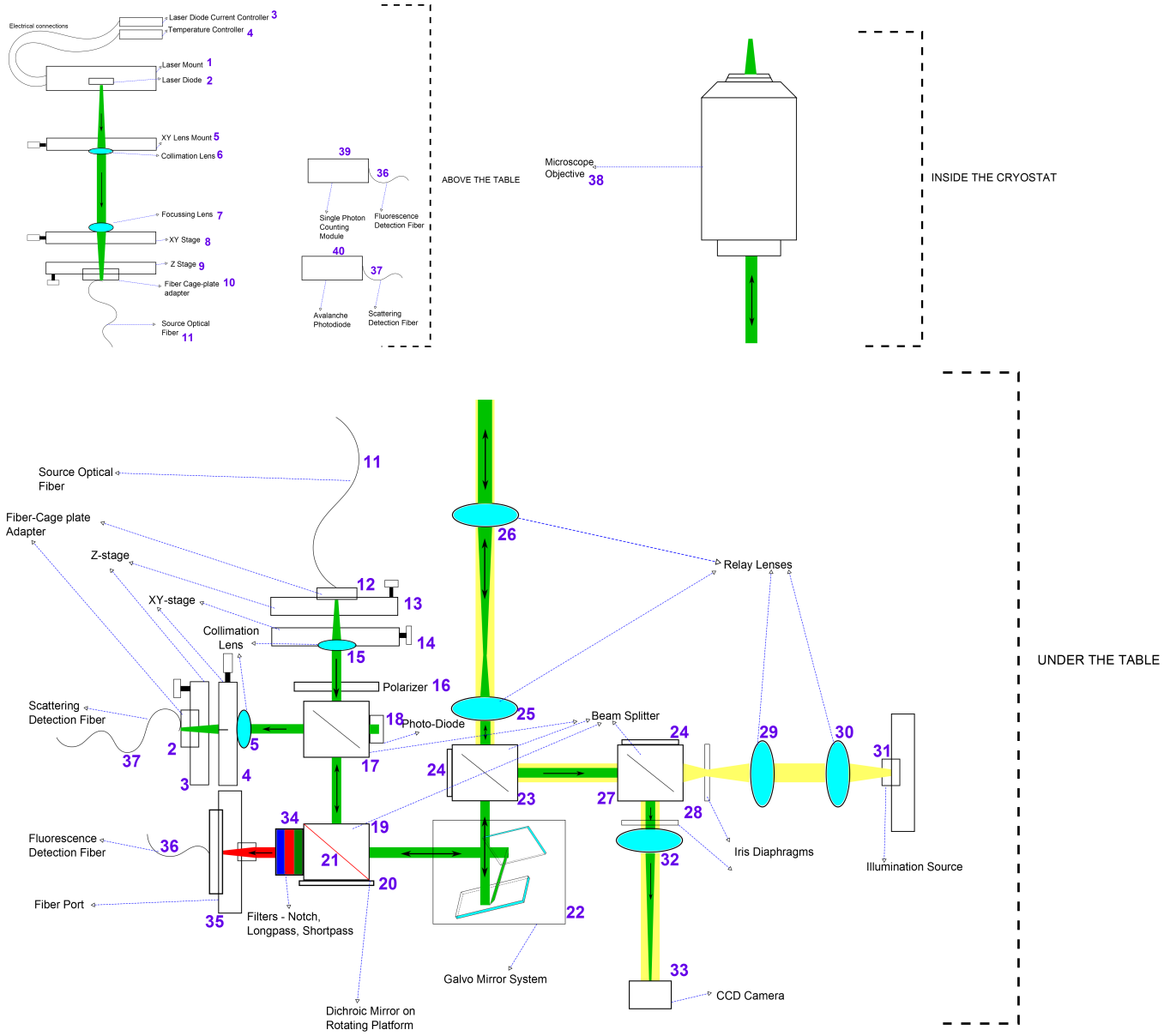


Figure 61: Layout of optics used to detect the presence of NV centers in diamond. Refer to Table 10 for numbering reference.

The figure above and the table below give a description of the optical elements used to detect the presence of NV centers on a sample and perform ESR on them. The figure above is shown in Fig. 42, and is repeated here with more details. All the optical elements shown here are from Thorlabs, unless specified otherwise.

| S.N. | Component Description[16] | Part Number |
|---|---|---|
| **ABOVE THE TABLE** | | |
| 1 | Laser Diode Mount | TCLDM9 |
| 2 | Laser Diode | DJ532-40[17] |
| 3 | Laser Diode Current Controller | LDC205C |
| 4 | Laser Diode Temperature Controller | TED200C |
| 5 | Cage XY Translation Stage | CXY1 |
| 6 | Collimation Lens | AC254-075-A-ML |
| 7 | Focusing Lens | C671TME-A |
| 8 | XY Stage | CP1XY [18] |
| 9 | Z Stage | SM1Z |
| 10 | Fiber to cage-plate adapter | SM1FCA |
| 11 | APC/PC Polarization maintaining fiber | P5-405BPM-FC-2 |
| **UNDER THE TABLE** | | |
| 11 | Source Optical Fiber comes down from above the table | |
| 12 | Fiber to cage-plate adapter | SM1FC |
| 13 | Z Stage | SM1Z |
| 14 | XY Stage | CP1XY [19] |
| 15 | Collimation Lens | C280TME-A |
| 16 | Polarizer | LPVISE100-A [20] |
| 17 | Pellicle 45:55 Beam Splitter | CM1-BP145B1 |
| 18 | Photodiode [21] | SM05PD1A[22] |
| 19 | 30 mm Cage Cube | C4W |
| 20 | Precision Kinematic Rotating Cage Cube Platform | B4CRP |

| | | |
|---|---|---|
| 21 | 567 nm Longpass Dichroic Mirror | DMLP567R[23] |
| 22 | 2D Large Beam Diameter Galvo System | GVS012 |
| 23 | Pellicle 8:92 Beam Splitter | CM1-BP108 |
| 24 | Caps to reduce reflections | NE20A-A mounted in SM1L03T |
| 25<br>26 | Relay Lenses for Laser[24] | AC254-100-A-ML<br>AC254-200-A-ML |
| 27 | Pellicle 45:55 Beam Splitter | CM1-BP145B1 |
| 28 | Graduated Ring-Activated Threaded Iris Diaphragms [25] | SM1D12C |
| 29<br>30 | Relay Lenses for Illumination Source[26] | AC254-100-A-ML<br>AC254-35-A-ML |
| 31 | Illumination Source - Green [27]<br>Illumination Source - White | CREE XRE-G<br>CREE XRE-W107 |
| 32 | Focusing Lens [28] | AC254-060-A |
| 33 | CCD Color Camera | DCU224C |
| 34 | Notch filter | NF533-17 |
| | Longpass Filter [29] | FEL0650 |
| | Shortpass Filter [30] | FES0800 |
| 35 | Fiber Port (comes with Collimation Lens) [31] | PAF-X-18-PC-B |
| 36 | Single-mode fiber for fluorescence detection | P1-630PM-FC-5 |
| 37 | Multimode fiber for scattering detection | M42L05 |

**INSIDE THE CRYOSTAT**

| | | |
|---|---|---|
| 38 | Objective | Same as mentioned in Table 9 |

**ABOVE THE TABLE**

| | | |
|---|---|---|
| 36 | Fluorescence Detection Fiber comes above from under the table | |
| 37 | Scattering Detection Fiber comes above from under the table | |
| 39 | Single Photon Counting Module | Excelitas: |

| | | |
|---|---|---|
| | | SPCM-AQRH-14-FC |
| 40 | Avalanche Photo diode | APD110A |

Table 10: List of the optical components used to detect the presence of NV centers in diamonds

[16]Most of these parts are held in a 30 mm cage system
[17]Additional adapter TCLDM9DJ was needed to hold the diode in the mount
[18]Lens is held in using S05TM09
[19]Lens is held in using S05TM09
[20]Held in SM1L03 lens tube and threaded into the below-mentioned beam splitter
[21]Optional - if incoming beam needs monitoring
[22]Threaded into the beam-splitter port using SM1A6
[23]Held onto above platform using FFM1
[24]Held using CP02
[25]Held either using CP02 or SM1V10
[26]Held using CP02
[27]Held using home-made holder - design shown in Fig. 58
[28]Held using SM1V10 and other fixed lens tubes
[29]The longpass and shortpass filters are optional
[30]All three filters are stacked together in SM1L10 and threaded into the side-port of the beam splitter
[31]Held using CP02FP

## A.3 ELECTRONICS USED FOR DEVICE DETECTION

| S.N. | Component/Instrument Name | Part Number | Manufacturer |
|---|---|---|---|
| 1 | Avalanche Photo Diode (APD) | APD110A | Thorlabs |
| 2 | Bias T | ZFBT-4R2GW+ | Mini-Circuits |
| 3 | Amplifier | AU-1310 | Miteq |
| 3* [32] | Low-Pass Filter | SLP-30+ | Mini-Circuits |
| 4 | Splitter | ZMSC-2-1+/ZMSC-2-1W/ZMSC-2-1W+ | Mini-Circuits |
| 5 | Spectrum Analyzer | E4404B | Agilent |
| 6 | Synthesizer | D310 | PTS |
| 7 | Fixed Attenuators | SAT/VAT-(Shown Value) | Mini-Circuits |
| 8 | Mixer | ZLW-1-1+ | Mini-Circuits |
| 8* [33] | Fixed Attenuator<br>Amplifier | VAT-20+<br>ZFL-1000+ | Mini-Circuits<br>Mini-Circuits |
| 9 | Synthesizer | 500 | PTS |
| 10 | Variable Attenuator | 0-70dB+0-10dB Rack-Mounted | |
| 11 | Amplifier | Customized circuit - described below and shown in Fig. 63 | |
| 12 | DC Supply | Home-built circuit - as shown in Fig. 64 | |
| 13 | Band-Pass (Crystal) Filter | SIF-21.4+ | Mini-Circuits |
| 14 | Amplifier | ZFL-1000LN/LN+ | Mini-Circuits |
| 15 | Splitter | ZFSCJ-2-1 | Mini-Circuits |
| 16 | Oscilloscope | TDS 2024B | Tektronix |
| 17 | Mixer | ZLW-6+ | Minicircuits |
| 17* [34] | Fixed Attenuator<br>Low-Pass Filter | SAT-3<br>SLP-1.9+ | Mini-Circuits<br>Mini-Circuits |
| 18 | Lock-In Amplifier | SR830 | SRS |

Table 11: List of RF electronic components/instruments used for Detection of NMO

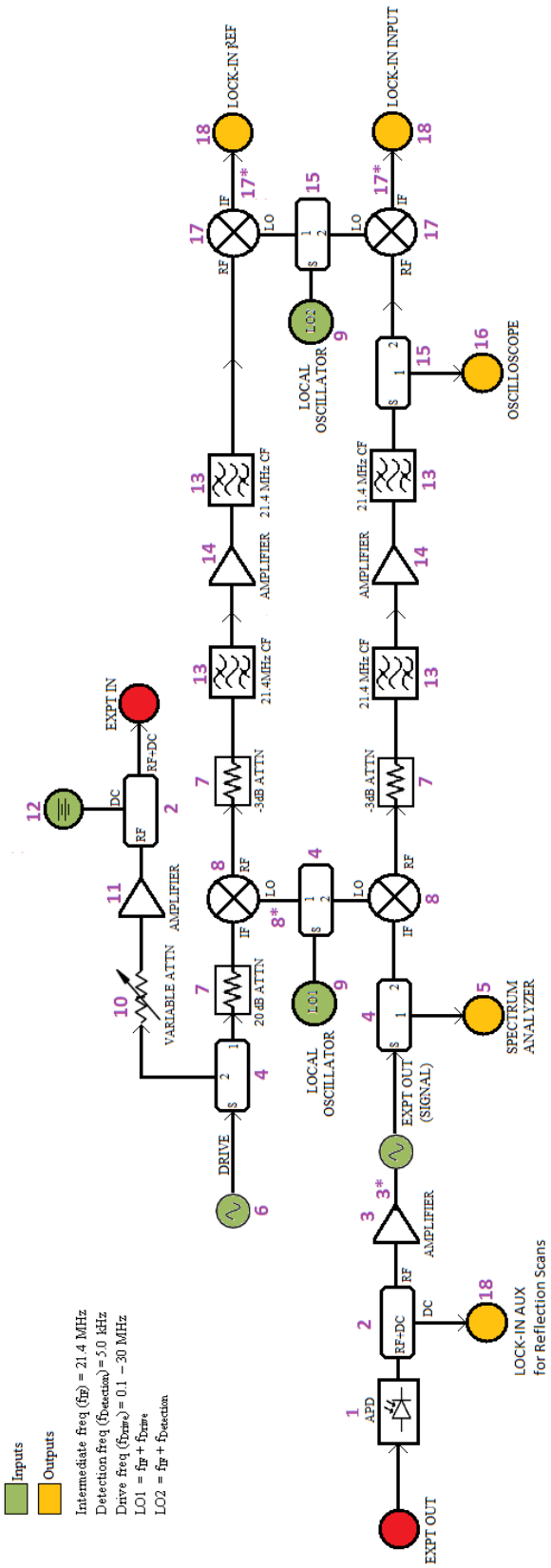


Figure 62: Layout of the electronic components used to detect the motion of the NMO

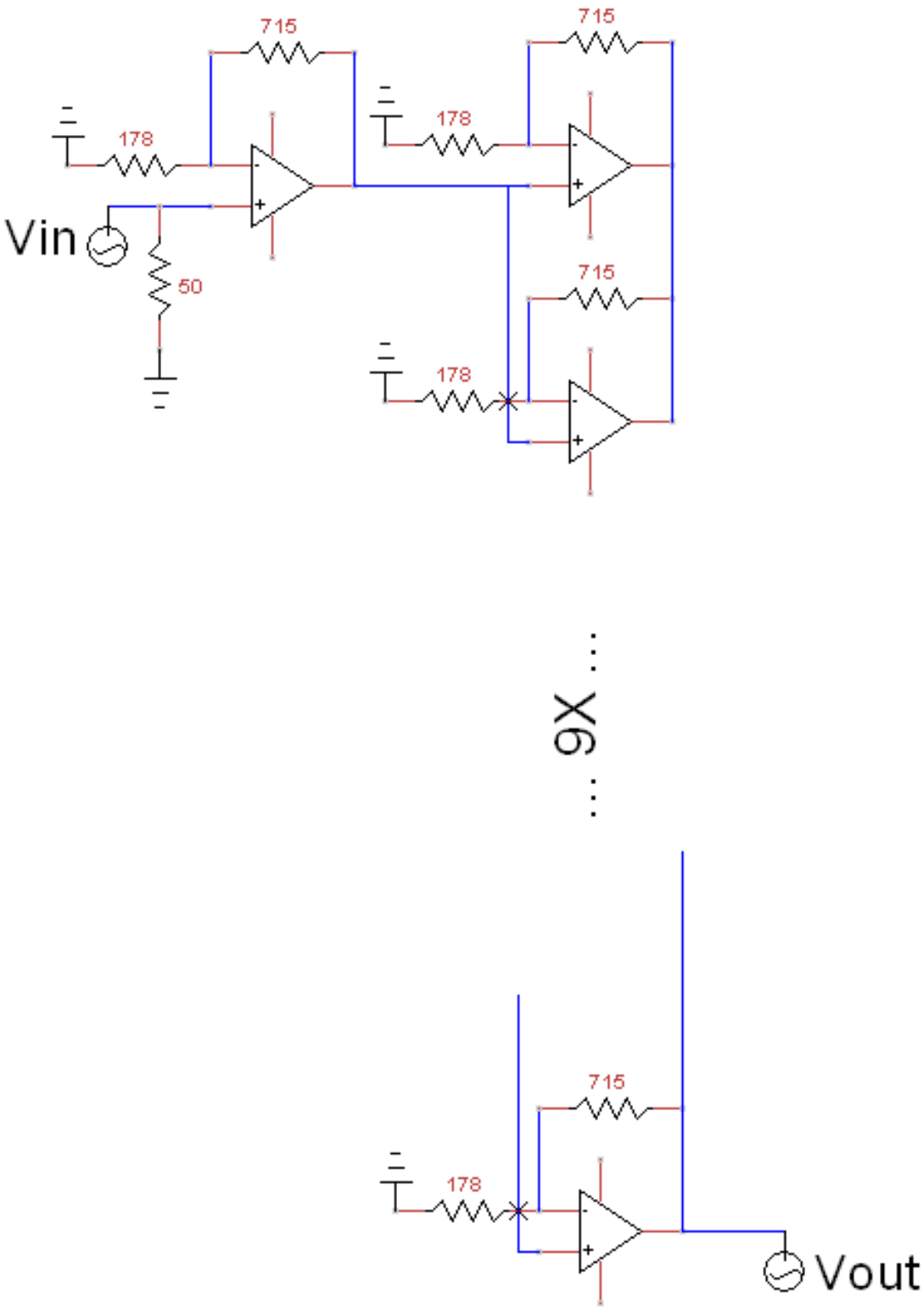


Figure 63: Home-made amplifier used to drive the devices, built using evaluation boards

The custom-built amplifier used to amplify the ac drive of the devices on our sample was made using five evaluation boards (Texas Instruments: THS3092DDA EVM). Each of these boards had two op-amps each, with resistors as shown in the circuit above. A few changes and connections were made on these boards, described with reasons below:

1. The first op-amp on the first board was connected in series to the second op-amp on the same board.

2. The first op-amp on the first board was used as a non-inverting amplifier, giving a voltage-gain of 5 (due to the resistors on the board) to the drive signal.

3. The second op-amp on the first board, and all the op-amps on the other boards were connected in parallel to each other. This was done to increase the output current of the amplifier, to drive the capacitative and resistive load of our sample.

4. The output of the last op-amp on the last board was used taken and transmitted through the coax in the cryostat to drive the devices on our sample.

5. The 50Ω resistors on the input of the second op-amp on each board were removed, to make parallel connections between the op-amps easy. Also, due to unknown load resistance of the sample, this was essential to avoid any unnecessary loss of power.

6. The 50Ω resistors on the input of the first op-amp on each board, except the first board, were removed. Again, this was done to make the interconnections easy, and the first one was left in there, to ensure impedance matching with the drive synthesizer.

[32]3* - This Low Pass Filter was added to decrease the noise from the APD
[33]8* - This was done to decrease any noise from LO1 to go into the experiment
[34]17* - This was done to decrease the noise going into the Lock-in Amplifier

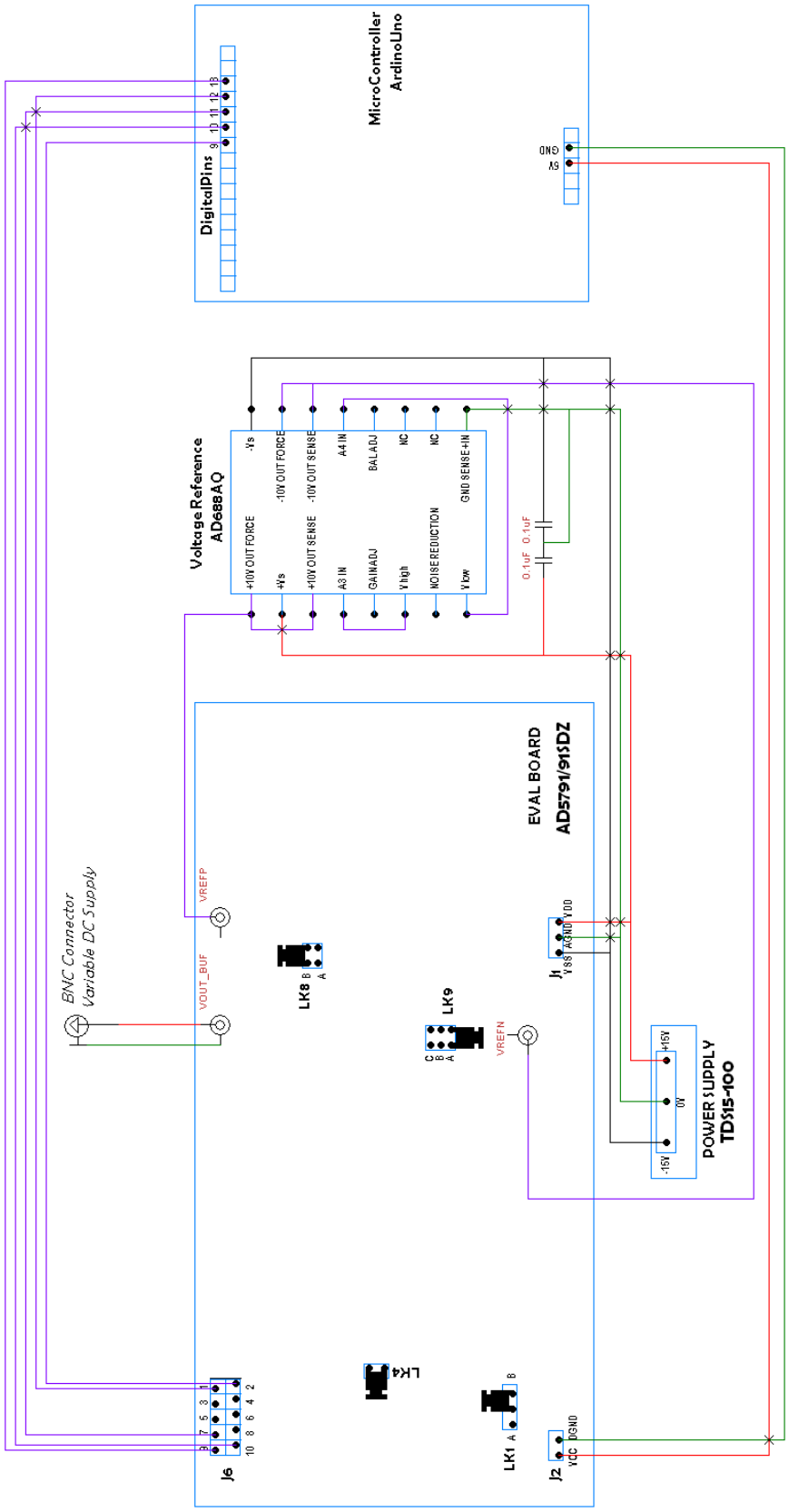


Figure 64: Home-made circuit for the DC supply used for device actuation

## A.4 ELECTRONICS USED FOR NV DETECTION AND ESR

Here I list the electronic components and instruments used for CW ESR on the NV centers in the nanodiamonds.

| S.N. | Component/Instrument Name | Part Number | Manufacturer |
|---|---|---|---|
| 1 | Synthesizer | PTS3200 | PTS |
| 2 | Microwave Cable | CBL-10FT-SMSM+ | Mini-Circuits |
| 3 | Variable Attenuator | 8496B | Agilent |
| 4 | Microwave Cable | CBL-15FT-SMSM+ | Mini-Circuits |
| 5 | Amplifier on Test Board | PHA-1+ on TB-545-1+ | Mini-Circuits |
| 6 | Variable Attenuator | 8494A | HP |

Table 12: List of RF electronic components/instruments used for Detection of NMO

A home-made counter was used to count the pulses from the SPCM, the circuit for which is shown in Fig. 65:

## A.5 MAGNETIC FIELD SENSOR

Attached below is the data sheet and calibration table of the magnetic field sensor that was used to measure the magnetic field generated by the permanent and electrical magnets in the cryostat.

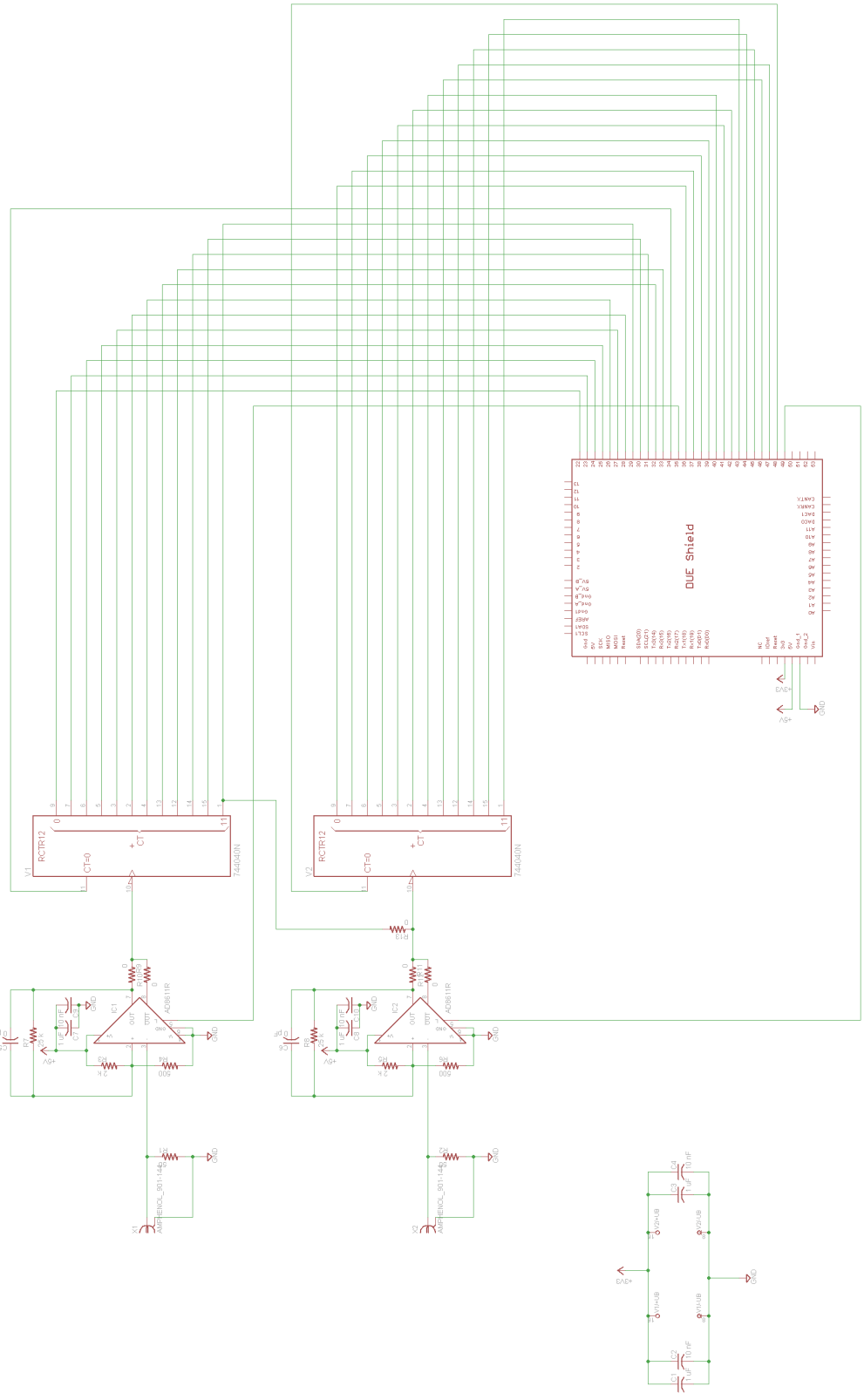


Figure 65: Home-made counter was used to count the pulses from the SPCM

# Bulk Indium BH-900 Series **Hall Sensors**

High Linearity

## Description

F.W. Bell 900 Series Hall Sensors are high-performance units providing high linearity and broad field and temperatures ranges for a wide variety of magnetic field measurements. All units in the series are encapsulated in rugged, epoxy, sealed cases. A room temperature linearity error curve from -30 to +30 kG is supplied, indicating optimum operating conditions for each device. The models 900 and 921 are not calibrated above 30 kG.

## Mechanical Specifications

a. Leads
b. Material: AWG 34 Copper with Teflon Insulation (Model 921) or Polyurethane Insulation (Models 900 & 910).
c. Color Code
d. Control Current ($I_c$): Red (+ $I_c$) Black (- $I_c$)
   Hall Voltage ($V_H$): Blue (+ $V_H$) Yellow (- $V_H$)
e. Polarity: With the magnetic field vector (+B) entering the top of the Hall plate and $I_c$ entering the red lead, the positive Hall voltage will appear at the blue leads.

Axial Hall Sensors BHA-900, 910 & 921

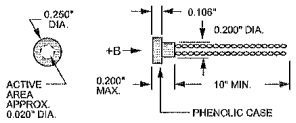


Transverse Hall Sensors BHT-900, 910 & 921

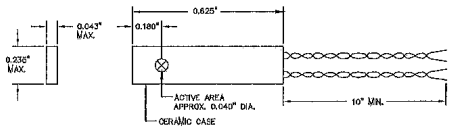


Note: cross indicates tail of magnetic field vector

## Models

a. BH-910 High Linearity
b. BH-921 Cryogenic Operation (1.5 to 350° k)
c. BH 921 & 900 Wide Dynamic Range

| SPECIFICATIONS | UNITS | BHT-900 | BHT-910 | BHT-921 | BHA-900 | BHA-910 | BHA-921 |
|---|---|---|---|---|---|---|---|
| Input resistance, $R_{in}$ (1) (4) | ohms | 1.2 max. | 1.2 max. | 1.2 max. | 1.5 max. | 1.5 max. | 1.5 max. |
| Output resistance, $R_{out}$(4) | ohms | 1.2 max. | 1.2 max. ohms | 1.2 max. | 1.5 max | 1.5 max. | 1.5 max. |
| Magnetic sensitivity, $V_H$ (1) (4) | mV/kG | .55 to 1.1 | .55 to 1.1 | .55 to 1.1 | .55 to 1.1 | .55 to 1.1 | .55 to 1.1 |
| Max. resistive residual voltage, $V_M$ @ B=0 (1) (4) | µV | 75 | 75 | 75 | 75 | 75 | 75 |
| Max. control current @ 25°C, static air | mA | 300 | 300 | 300 | 300 | 300 | 300 |
| Nominal control current, $I_{cn}$ | mA | 100 | 100 | 100 | 100 | 100 | 100 |
| Max linearity error (-30 to +30 kG) (1) | ±% of RDG | 1 | 1 (2) | 1 | 1 | .25 | 1 |
| Max linearity error (-150 to +150 kG) (1) | ±% of RDG | 1.5 | – | 2 | 1.5 | – | 2 |
| Typical linearity resistance Rlin | ohms | 500 | 50 to 500 | 500 | 500 | 50 to 500 | 500 |
| Mean temperature coefficient of $V_H$ (-20°C to +80°C) (1) | PPM/ C | ±50 max. | ±50 max. | ±100 max. (3) | ±50 max. | ±50 max. | ±100 max. (3) |
| Mean temperature coefficient of resistance (-20°C to +80°C) (1) | +% /°C | 0.15 max. | 0.15 max. | 0.6 max. (3) | 0.15 max. | 0.15 max. | 0.6 max. (3) |
| Temperature dependence of resistive residual voltage (-20° C to +80° C) (1) | ±µV/°C | 0.1 max. | 0.1 max. | 0.1 max. (3) | 0.1 max. | 0.1 max. | 0.1 max. (3) |
| Operating temperature range | °C | -40 to +100 | -40 to +100 | -269 to +100 | -40 to +100 | -40 to +100 | -269 to +100 |

**Notes:** Due to continuous process improvement, specifications subject to change without notice.

(1) $I_C = I_{cn}$
(2) ±.1% linearity error (0-30 kG)
    ±.3% reversibility error
(3) Specification applies over operating temperature range (-269 to +100°C)
(4) T= 25°C

SYPRIS TEST & MEASUREMENT 6120 Hanging Moss Road • Orlando, Florida 32807
Phone (407) 678-9748 • Fax (407) 677-5765 • www.fwbell.com

F.W. BELL®

Rev. date 04/2003

Linearity Report printed at 06:36 Apr. 06, 2010

Lot No. / Shop Order: 65723 Tester: MYR Date: 04-05-2010
Item No: 177034 Linearizing Resistor,Rlin = 400 ohms
Hall Device Type: BHT921 Input Resistance, Rin = 0.88 ohms
Hall Device Serial No: 14667 Output Resistance,Rout = 0.75 ohms
Probe Serial No: Zero Offset, Vm = 0.0103 mV
Probe Model: Control Current, Ic = 100.00 mA
Maximum Absolute Error = 0.173% Reversibility Error = 0.222%
Loaded Sensitivity Constant at 3kG, Yb = 0.791 mV/kG
Unloaded Sensitivity Constant at 3kG, Yb = 0.793 mV/kG

| -Field (kG) | UUT Output (kG) | UUT Error (Gauss) | UUT Error (% reading) | +Field (kG) | UUT Output (kG) | UUT Error (Gauss) | UUT Error (% reading) |
|---|---|---|---|---|---|---|---|
| -30.175 | -30.158 | -16.831 | 0.056 | 0.000 | 0.000 | -0.001 | 0.000 |
| -29.016 | -29.003 | -12.749 | 0.044 | 0.990 | 0.992 | 1.712 | 0.173 |
| -27.768 | -27.756 | -11.933 | 0.043 | 2.014 | 2.016 | 1.322 | 0.066 |
| -26.614 | -26.608 | -6.042 | 0.023 | 3.012 | 3.014 | 1.739 | 0.058 |
| -25.730 | -25.728 | -1.907 | 0.007 | 3.999 | 4.002 | 2.310 | 0.058 |
| -25.049 | -25.056 | 7.425 | -0.030 | 4.989 | 4.991 | 2.218 | 0.044 |
| -23.782 | -23.779 | -2.793 | 0.012 | 5.994 | 5.996 | 1.795 | 0.030 |
| -23.171 | -23.171 | 0.113 | -0.000 | 6.997 | 7.000 | 2.484 | 0.035 |
| -22.289 | -22.282 | -6.359 | 0.029 | 7.993 | 7.995 | 1.651 | 0.021 |
| -21.170 | -21.160 | -9.301 | 0.044 | 8.988 | 8.990 | 1.711 | 0.019 |
| -20.140 | -20.131 | -8.387 | 0.042 | 10.000 | 10.001 | 0.736 | 0.007 |
| -19.115 | -19.108 | -7.890 | 0.041 | 11.017 | 11.017 | 0.257 | 0.002 |
| -18.083 | -18.078 | -5.099 | 0.028 | 12.021 | 12.020 | -1.285 | -0.011 |
| -17.080 | -17.076 | -4.156 | 0.024 | 13.024 | 13.022 | -2.252 | -0.017 |
| -16.072 | -16.069 | -3.241 | 0.020 | 14.039 | 14.037 | -2.584 | -0.018 |
| -15.047 | -15.044 | -3.056 | 0.020 | 15.044 | 15.039 | -4.672 | -0.031 |
| -14.042 | -14.040 | -1.892 | 0.013 | 16.055 | 16.049 | -6.190 | -0.039 |
| -13.026 | -13.024 | -2.100 | 0.016 | 17.076 | 17.069 | -6.907 | -0.040 |
| -12.023 | -12.022 | -1.305 | 0.011 | 18.077 | 18.069 | -8.486 | -0.047 |
| -11.016 | -11.016 | 0.079 | -0.001 | 19.110 | 19.098 | -11.712 | -0.061 |
| -10.004 | -10.003 | -0.545 | 0.005 | 20.122 | 20.109 | -12.316 | -0.061 |
| -9.002 | -9.003 | 0.918 | -0.010 | 21.162 | 21.147 | -15.141 | -0.072 |
| -8.007 | -8.006 | -0.427 | 0.005 | 22.282 | 22.265 | -16.827 | -0.076 |
| -6.999 | -6.999 | -0.566 | 0.008 | 23.170 | 23.154 | -15.618 | -0.067 |
| -6.004 | -6.004 | 0.139 | -0.002 | 23.773 | 23.756 | -16.983 | -0.071 |
| -5.001 | -5.001 | -0.454 | 0.009 | 25.050 | 25.029 | -21.735 | -0.087 |
| -4.012 | -4.012 | -0.703 | 0.018 | 25.730 | 25.700 | -29.367 | -0.114 |
| -3.012 | -3.012 | -0.394 | 0.013 | 26.614 | 26.579 | -35.878 | -0.135 |
| -1.987 | -1.987 | -0.245 | 0.012 | 27.765 | 27.724 | -40.918 | -0.147 |
| -0.989 | -0.989 | -0.487 | 0.049 | 29.015 | 28.969 | -46.237 | -0.159 |
| 0.000 | 0.000 | -0.001 | 0.000 | 30.173 | 30.121 | -52.131 | -0.173 |

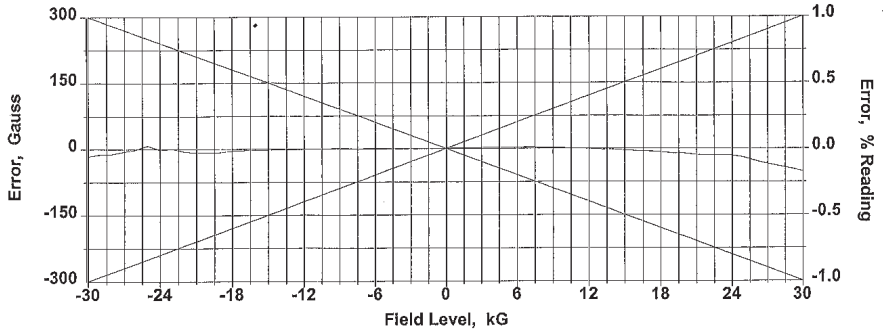


Figure 66: Data sheet and calibration table of the magnetic field sensor

# APPENDIX B

# PHOTOLITHOGRAPHY SETUP

To perform photolithography (PLT) on our samples, we designed and built a home-made setup. This was the first optical setup that I built in the lab. This setup consisted of a few optical elements mounted on an I-beam, which we mounted on one of the axis of our diamond-turning machine (DTM). The optical elements here are mounted on a 30 $mm$ cage system. The DTM was used for the precise movement of its hydraulically-levitated slides. On the other axis of the DTM we mounted a vacuum-chuck to hold down the samples. Using the relative movement of the two slides, and by programming the DTM computer, we were able to generate the desired patterns on our samples. The laser controller, diode and associated optics, and an optical shutter was mounted on a table behind the DTM, and an optical fiber was used to transmit the light to the DTM.

The table below lists the optical elements used for this setup. All the optical elements shown here are from Thorlabs, unless specified otherwise.

| S.N. | Component Description | Part Number |
|---|---|---|
| 1 | Laser Diode Mount | K6X |
| 2 | Laser Diode | GH04020B2A |
| 3 | Laser Diode Current Controller | LDC202C |
| 4 | Laser Diode and Lens tube | LT110-A [1] |
| 5 | Collimation Lens | C671TME-405 |
| 6 | Neutral Density Filter Wheel | FW1AND |
| 7 | Shutter | SH05 |
| 8 | Shutter Controller | SC10 |
| 9 | Collimation Lens into fiber | F671FC-405 [2] |
| 10 | XY and Tip-Tilt Stage | K6X |
| 11 | Optical fiber | P1-405A-FC-5 |
| 12 | Fiber to cage-plate adapter | SM1FC |
| 13 | XY Stage | CXY1 |
| 14 | Collimation Lens | AC127-019-A-ML |
| 15 | Z Stage to hold lens | SM1Z [3] |

| | | |
|---|---|---|
| 16 | Beam Splitter | CM1-BS013 [4] |
| 17 | Red LED array light source | LIU001 [5] |
| 18 | Camera | Industrial Vision Supply IV-BWCAM3 [6] |
| 19 | Lens for focusing onto camera | AC254-150-A [7] |
| 20 | Cap to reduce reflections | SM1CP2 [8] |
| 21 | Filter to reduce reflections | FES0450 [9] |
| 22 | Z-stage to hold objective | SM1Z |
| 23 | Objectives used to focus laser on sample | Mitutoyo [10] |
| 24 | Stage to mount cage system to I-beam | DT25 |
| 25 | Power sensor | S120C/S121C |
| 26 | Power meter | PM100A |

Table 13: List of optical components used for the PLT setup

The figure below shows the assembled optical setup, outside and inside the diamond-turning machine.

[1]Custom part - See attached quote - Held using AD15F
[2]Held using AD11F
[3]Lens is held in using SM1A6
[4]Using two - one for illumination, one for camera
[5]Clamped onto cage system using CP03; Required power supply: LIU-PS
[6]Mounted on lens tubes using SM1A9 and SM1T2 onto CP02T
[7]Used with Lens tubes SM1E60 and SM1V10
[8]On the camera beam splitter
[9]On the illumination beam splitter
[10]Different ones used depending on required resolution - Mounted using 55-743 from Edmund Optics and SM1A10

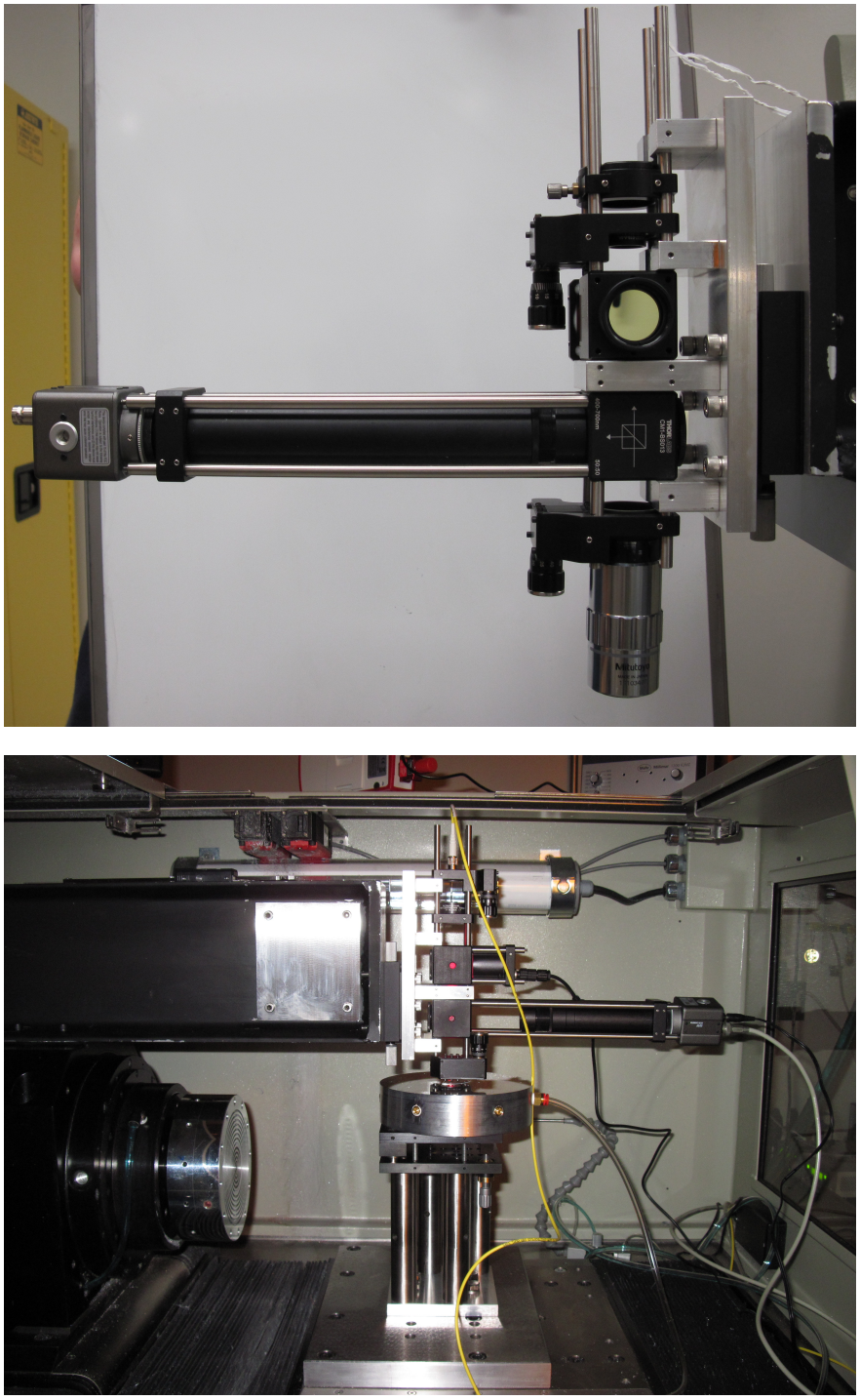

Figure 67: Photolithography (PLT) setup used for patterning devices out of thin films (a)Optical elements were mounted on an I-beam and (b)The I-beam was mounted on one slide of the DTM and the sample was held down by vacuum on the other slide. The relative motion of the two slides enabled patterning the sample.

**Thorlabs, Inc.**
435 Route 206
Newton, NJ 07860

Phone ...: 973-579-7227
Fax .....: 973-300-3600

# Quotation

***Bill to***

**University of Pittsburgh**
**100 Allen Hall**
**3941 OHara St**
**Pittsburgh, PA 15260**

***Ship to***

**University of Pittsburgh**
**100 Allen Hall**
**3941 OHara St**
**Pittsburgh, PA 15260**

**Attention: Shonali Dhingra**
**Telephone: 412-624-9600**

Number .....: TQ0016957-1
Created date .....: 11/30/2009
Date .....: 11/30/2009
Quotation Deadline .....: 1/29/2010
**Purchase order .....: DHINGRA/QUOTE**
Terms of payment .....: Net 30
Invoice Account .....: 197964
Sales order .....:
Sales Contact .....: Meredith Clark
Ship Via .....: UPS Ground
Terms of Delivery .....: FOB Shipping Point

Page .....: 1 of 1

| Item Number | Description | Quantity | Price Each | Disc. % | Disc. Price | Amount | | Ship date |
|---|---|---|---|---|---|---|---|---|
| LT110A | Laser Diode Collimation Tube 0.85" Lead Time: 1 Week | 1.00 | 40.00 | | 40.00 | 40.00 | USD | 11/30/2009 |

Thank you for your interest in Thorlabs products. All quotes are valid for 60 days. Any changes may affect your pricing. Shipping Charges are estimated. Freight charges for heavyweight items may not appear on this quotation and will be added upon receipt of order. Release fees & custom taxes are not included in the shipping fee. Please pay in US funds by check, credit card, or wire to Thorlabs, Inc Acct# 205000754, bank routing #021205376 C/O Lakeland Bank, 615 Rt. 206N., Newton NJ 07860 EIN:22-2873153

NOTE: TO ENSURE ACCURACY, PLEASE REFER TO YOUR QUOTE NUMBER WHEN PLACING YOUR ORDER

| | | |
|---|---|---|
| Subtotal: | 40.00 | |
| Total Discount: | 0.00 | |
| Shipping and Handling: | 6.35 | |
| Sales Tax : | 0.00 | |
| Grand Total: | 46.35 | USD |

Figure 68: Quote for custom collimating tube LT110-A

## BIBLIOGRAPHY


[1] Albert Messiah. *Quantum Mechanics - Two volumes bound as one*. Dover Publications, Inc., NY, 1999.

[2] Marvin Chester. *Primer of quantum mechanics*. Courier Dover Publications, 2012.

[3] Michael Roukes. Nanoelectromechanical systems face the future. *Phys. World*, 14(2):25–31, 2001.

[4] Michael Roukes. Plenty of room, indeed. *Scientific American*, 285(3):42–9, 2001.

[5] Keith C Schwab and Michael L Roukes. Putting mechanics into quantum mechanics. *Physics Today*, 58(7):36–42, 2005.

[6] X. M. H. Huang, C. A. Zorman, M. Mehregany, and M. L. Roukes. Nanoelectromechanical systems: Nanodevice motion at microwave frequencies. *Nature*, 421:496, 2003.

[7] C. M. Caves, K. S. Thorne, R. W. P. Drever, V. D. Sandberg, and M. Zimmermann. On the measurement of a weak classical force coupled to a quantum-mechanical oscillator. I. Issues of principle. *Rev. Mod. Phys*, 52:341, 1980.

[8] D. Rugar, R. Budakian, H. J. Mamin, and B. W. Chui. Single spin detection by magnetic resonance force microscopy. *Nature*, 430:329, 2004.

[9] K Jensen, Kwanpyo Kim, and A Zettl. An atomic-resolution nanomechanical mass sensor. *Nature nanotechnology*, 3(9):533–537, 2008.

[10] Julien Chaste, A Eichler, J Moser, G Ceballos, R Rurali, and A Bachtold. A nanomechanical mass sensor with yoctogram resolution. *Nature nanotechnology*, 7(5):301–304, 2012.

[11] Aaron D OConnell, M Hofheinz, M Ansmann, Radoslaw C Bialczak, M Lenander, Erik Lucero, M Neeley, D Sank, H Wang, M Weides, et al. Quantum ground state and single-phonon control of a mechanical resonator. *Nature*, 464(7289):697–703, 2010.

[12] I Wilson-Rae, P Zoller, and A Imamolu. Laser cooling of a nanomechanical resonator mode to its quantum ground state. *Physical review letters*, 92(7):075507, 2004.

[13] JD Teufel, Tobias Donner, Dale Li, JW Harlow, MS Allman, Katarina Cicak, AJ Sirois, Jed D Whittaker, KW Lehnert, and Raymond W Simmonds. Sideband cooling of micromechanical motion to the quantum ground state. *Nature*, 475(7356):359–363, 2011.

[14] Jasper Chan, TP Mayer Alegre, Amir H Safavi-Naeini, Jeff T Hill, Alex Krause, Simon Gröblacher, Markus Aspelmeyer, and Oskar Painter. Laser cooling of a nanomechanical oscillator into its quantum ground state. *Nature*, 478(7367):89–92, 2011.

[15] Mo Li, Hong X Tang, and Michael L Roukes. Ultra-sensitive nems-based cantilevers for sensing, scanned probe and very high-frequency applications. *Nature nanotechnology*, 2(2):114–120, 2007.

[16] Andrew N Cleland and Michael L Roukes. A nanometre-scale mechanical electrometer. *Nature*, 392(6672):160–162, 1998.

[17] Markus Aspelmeyer and Keith Schwab. Focus on mechanical systems at the quantum limit. *New Journal of Physics*, 10(9):095001, 2008.

[18] Philipp Treutlein, Claudiu Genes, Klemens Hammerer, Martino Poggio, and Peter Rabl. Hybrid mechanical systems. In *Cavity Optomechanics*, pages 327–351. Springer, 2014.

[19] Olivier Arcizet, Vincent Jacques, Alessandro Siria, Philippe Poncharal, Pascal Vincent, and Signe Seidelin. A single nitrogen-vacancy defect coupled to a nanomechanical oscillator. *Nature Physics*, 7(11):879–883, 2011.

[20] Stephan Camerer, Maria Korppi, Andreas Jöckel, David Hunger, Theodor W Hänsch, and Philipp Treutlein. Realization of an optomechanical interface between ultracold atoms and a membrane. *Physical review letters*, 107(22):223001, 2011.

[21] D. Bouwmeester, A. K. Ekert, and A. Zeilinger, editors. *The physics of quantum information: quantum cryptography, quantum teleportation, quantum computation*. Springer-Verlag, NY, 2000.

[22] D.P. DiVincenzo. Quantum computation. *Science*, 270:255, 1995.

[23] M. A. Nielsen and I. L. Chuang. *Quantum computation and quantum information*. Cambridge University Press, New York, 2000.

[24] Lilian Isabel Childress. *Coherent manipulation of single quantum systems in the solid state*. PhD thesis, Harvard University Cambridge, Massachusetts, 2007.

[25] N.B. Manson, J.P. Harrison, and M.J. Sellars. Nitrogen-vacancy center in diamond: Model of the electronic structure and associated dynamics. *Phys. Rev. B*, 74:104303, 2006.

[26] JoHoNo Loubser and JoA van Wyk. Electron spin resonance in the study of diamond. *Reports on Progress in Physics*, 41(8):1201, 1978.

[27] D. A. Redman, S. Brown, R. H. Sands, and S. C. Rand. Spin dynamics and electronic states of nv centers in diamond by epr and four-wave-mixing spectroscopy. *Phys. Rev. Lett.*, 67:3420, 1991.

[28] S. Takahashi, R. Hanson, J. van Tol, M. S. Sherwin, and D. D. Awschalom. Quenching spin decoherence in diamond through spin bath polarization. *Phys. Rev. Lett.*, 101:047601, 2008.

[29] G. Balasubramanian, P. Neumann, D. Twitchen, M. Markham, R. Kolesov, N. Mizuochi, J. Isoya, J. Achard, J. Beck, J. Tissler, V. Jacques, P. R. Hemmer, F. Jelezko, and J. Wrachtrup. Ultralong spin coherence time in isotopically engineered diamond. *Nature Materials*, 8:383, 2009.

[30] J. Wrachtrup and F. Jelezko. Quantum information processing in diamond. *J. Phys.: Condens. Matter*, 18:S807, 2006.

[31] F. Jelezko, T. Gaebel, I. Popa, A. Gruber, and J. Wrachtrup. Observation of coherent oscillations in a single electron spin. *Phys. Rev. Lett.*, 92:076401, 2004.

[32] G. D. Fuchs, V. V. Dobrovitski, D. M. Toyli, F. J. Heremans, and D. D. Awschalom. Gigahertz dynamics of a strongly driven single quantum spin. *Science*, 326:1520, 2009.

[33] L. Childress, M. V. G. Dutt, J. M. Taylor, A. S. Zibrov, F. Jelezko, J. Wrachtrup, P. R. Hemmer, and M. D. Lukin. Coherent dynamics of coupled electron and nuclear spin qubits in diamond. *Science*, 314:281, 2006.

[34] M. V. G. Dutt, L. Childress, L. Jiang, E. Togan, J. Maze, F. Jelezko, A. S. Zibrov, P. R. Hemmer, and M. D. Lukin. Quantum register based on individual electronic and nuclear spin qubits in diamond. *Science*, 316:1312, 2007.

[35] P. Neumann, N. Mizuochi, F. Rempp, P. Hemmer, H. Watanabe, S. Yamasaki, V. Jacques, T. Gaebel, F. Jelezko, and J. Wrachtrup. Multipartite entanglement among single spins in diamond. *Science*, 320:1326, 2008.

[36] J. R. Maze, P. L. Stanwix, J. S. Hodges, S. Hong, J. M. Taylor, P. Cappellaro, L. Jiang, M. V. G. Dutt, E. Togan, A. S. Zibrov, A. Yacoby, R. L. Walsworth, and M. D. Lukin. Nanoscale magnetic sensing with an individual electronic spin in diamond. *Nature*, 455:644, 2008.

[37] G. Balasubramanian, I. Y. Chan, R. Kolesov, M. Al-Hmoud, J. Tisler, C. Shin, C. Kim, A. Wojcik, P. R. Hemmer, A. Krueger, T. Hanke, A. Leitenstorfer, R. Bratschitsch, F. Jelezko, and J. Wrachtrup. Nanoscale imaging magnetometry with diamond spins under ambient conditions. *Nature*, 455:648, 2008.

[38] V. B. Braginsky, Y. I. Vorontsov, and K. S. Thorne. Quantum nondemolition measurements. *Science*, 209:547, 1980.

[39] P. Rabl, P. Cappellaro, M. V. G. Dutt, L. Jiang, J. R. Maze, and M. D. Lukin. Strong magnetic coupling between an electronic spin qubit and a mechanical resonator. *Phys. Rev. B*, 79:041302, 2009.

[40] L Jiang, JS Hodges, JR Maze, P Maurer, JM Taylor, DG Cory, PR Hemmer, RL Walsworth, A Yacoby, AS Zibrov, et al. Repetitive readout of a single electronic spin via quantum logic with nuclear spin ancillae. *Science*, 326(5950):267–272, 2009.

[41] M Steiner, P Neumann, J Beck, F Jelezko, and J Wrachtrup. Universal enhancement of the optical readout fidelity of single electron spins at nitrogen-vacancy centers in diamond. *Physical Review B*, 81(3):035205, 2010.

[42] B. D'Urso, MV Gurudev Dutt, S. Dhingra, and NM Nusran. Quantum measurements between a single spin and a torsional nanomechanical resonator. *New Journal of Physics*, 13:045002, 2011.

[43] Shonali Dhingra, Jen-Feng Hsu, Ivan Vlassiouk, and Brian DUrso. Chemical vapor deposition of graphene on large-domain ultra-flat copper. *Carbon*, 69:188–193, 2014.

[44] Andrew Kozbial, Zhiting Li, Caitlyn Conaway, Rebecca McGinley, Shonali Dhingra, Vahid Vahdat, Feng Zhou, Brian DUrso, Haitao Liu, and Lei Li. Study on the surface energy of graphene by contact angle measurements. *Langmuir*, 30(28):8598–8606, 2014.

[45] Amol Choudhary, Shonali Dhingra, Brian DUrso, Tina L Parsonage, Katherine A Sloyan, Robert W Eason, and David P Shepherd. Q-switched operation of a pulsed-laser-deposited yb: Y 2 o 3 waveguide using graphene as a saturable absorber. *Optics letters*, 39(15):4325–4328, 2014.

[46] Amol Choudhary, Shonali Dhingra, Brian D'Urso, Pradeesh Kannan, and D Shepherd. Graphene q-switched mode-locked and q-switched ion-exchanged waveguide lasers. *Photonics Technology Letters*, 27(6):646–649, 2015.

[47] Amol Choudhary, Shonali Beecher, Stephen J.and Dhingra, Brian DUrso, Tina L Parsonage, James A. Grant-Jacob, Ping Hua, Jacob I. Mackenzie, Robert W Eason, and David P Shepherd. 456 mw graphene q-switched yb:yttria waveguide laser by evanescent-field interaction. *Optics letters*, Accepted, 2015.

[48] Mengchen Huang, Giriraj Jnawali, Jen-Feng Hsu, Shonali Dhingra, Hyungwoo Lee, Sangwoo Ryu, Feng Bi, Fereshte Gharari, Jayakanth Ravichandran, Lu Chen, Philip Kim, Chang-Beom Eom, Brian DUrso, Patrick Irvin, and Jeremy Levy. Electric field effects in graphene/laalo3/srtio3 heterostructures and nanostructures. *APL Materials*, 3(6):062502, 2015.

[49] Jen-Feng Hsu, Shonali Dhingra, and Brian DUrso. Patterning, transferring and suspension of single-layer graphene by deep-ultraviolet lithography on poly(methyl methacrylate). *Journal of Vacuum Science and Technology B*, In Preparation, 2015.

[50] Shonali Dhingra and Brian DUrso. Nitrogen vacancy center in diamond as $\theta^2$ sensor. *Physical Review B (Rapid Communcations)*, In Preparation:ArXiv:quant–phys/1503.00151, 2015.

[51] E. Muñoz, J. Lu, and B. I. Yakobson. Ballistic thermal conductance of graphene ribbons. *Nano Lett.*, 10:1652, 2010.

[52] J. M. Taylor, P. Cappellaro, L. Childress, L. Jiang, D. Budker, P. R. Hemmer, A. Yacoby, R. Walsworth, and M. D. Lukin. High-sensitivity diamond magnetometer with nanoscale resolution. *Nature Physics*, 4:810, 2008.

[53] Hongzhe Zhang and Xuejun Zhang. Factors affecting surface quality in diamond turning of oxygen-free high-conductance copper. *Applied optics*, 33(10):2039–2042, 1994.

[54] HL Gerth and RE Hewgley. Diamond turning large optics. In *Proc. of the SPIE*, volume 93, pages 46–52, 1976.

[55] Ho-Sang Kim and Eui-Jung Kim. Feed-forward control of fast tool servo for real-time correction of spindle error in diamond turning of flat surfaces. *International Journal of Machine Tools and Manufacture*, 43(12):1177–1183, 2003.

[56] FZ Fang and VC Venkatesh. Diamond cutting of silicon with nanometric finish. *CIRP Annals-Manufacturing Technology*, 47(1):45–49, 1998.

[57] G. Hass and N.W. Scott. On the structure and properties of some metal and metal oxide films. 1950.

[58] Jen-Feng Hsu. *TBD*. PhD thesis, University of Pittsburgh, Pennsylvania, 2016.

[59] AH Castro Neto, F Guinea, NMR Peres, KS Novoselov, and AK Geim. The electronic properties of graphene. *Reviews of modern physics*, 81(1):109, 2009.

[60] Alexander A Balandin. Thermal properties of graphene and nanostructured carbon materials. *Nature materials*, 10(8):569–581, 2011.

[61] Robert A Barton, Jeevak Parpia, and Harold G Craighead. Fabrication and performance of graphene nanoelectromechanical systems. *Journal of Vacuum Science & Technology B: Microelectronics and Nanometer Structures*, 29(5):050801–050801, 2011.

[62] LA Falkovsky. Optical properties of graphene. In *Journal of Physics: Conference Series*, volume 129, page 012004. IOP Publishing, 2008.

[63] F Schedin, AK Geim, SV Morozov, EW Hill, P Blake, MI Katsnelson, and KS Novoselov. Detection of individual gas molecules adsorbed on graphene. *Nature materials*, 6(9):652–655, 2007.

[64] Mark P Levendorf, Carlos S Ruiz-Vargas, Shivank Garg, and Jiwoong Park. Transfer-free batch fabrication of single layer graphene transistors. *Nano letters*, 9(12):4479–4483, 2009.

[65] Y-M Lin, Christos Dimitrakopoulos, Keith A Jenkins, Damon B Farmer, H-Y Chiu, Alfred Grill, and Ph Avouris. 100-ghz transistors from wafer-scale epitaxial graphene. *Science*, 327(5966):662–662, 2010.

[66] KS Novoselov, Andre K Geim, SV Morozov, D Jiang, Y Zhang, SV Dubonos, IV Grigorieva, and AA Firsov. Electric field effect in atomically thin carbon films. *Science*, 306(5696):666–669, 2004.

[67] Sasha Stankovich, Dmitriy A Dikin, Richard D Piner, Kevin A Kohlhaas, Alfred Kleinhammes, Yuanyuan Jia, Yue Wu, SonBinh T Nguyen, and Rodney S Ruoff. Synthesis of graphene-based nanosheets via chemical reduction of exfoliated graphite oxide. *Carbon*, 45(7):1558–1565, 2007.

[68] Claire Berger, Zhimin Song, Tianbo Li, Xuebin Li, Asmerom Y Ogbazghi, Rui Feng, Zhenting Dai, Alexei N Marchenkov, Edward H Conrad, Phillip N First, et al. Ultrathin epitaxial graphite: 2d electron gas properties and a route toward graphene-based nanoelectronics. *The Journal of Physical Chemistry B*, 108(52):19912–19916, 2004.

[69] Cecilia Mattevi, Hokwon Kim, and Manish Chhowalla. A review of chemical vapour deposition of graphene on copper. *J. Mater. Chem.*, 21(10):3324–3334, 2010.

[70] J Hass, R Feng, JE Millan-Otoya, X Li, M Sprinkle, PN First, WA De Heer, EH Conrad, and C Berger. Structural properties of the multilayer graphene/4h-sic (0001 [over$^-$]) system as determined by surface x-ray diffraction. *Physical Review B*, 75(21):214109, 2007.

[71] C Riedl, C Coletti, and U Starke. Structural and electronic properties of epitaxial graphene on sic (0 0 0 1): a review of growth, characterization, transfer doping and hydrogen intercalation. *Journal of Physics D: Applied Physics*, 43(37):374009, 2010.

[72] X. Li, W. Cai, J. An, S. Kim, J. Nah, D. Yang, R. Piner, A. Velamakanni, I. Jung, E. Tutuc, S. K. Banerjee, L. Colombo, and R. S. Ruoff. Large-area synthesis of high-quality and uniform graphene films on copper foils. *Science*, 324:1312, 2009.

[73] Alfonso Reina, Xiaoting Jia, John Ho, Daniel Nezich, Hyungbin Son, Vladimir Bulovic, Mildred S Dresselhaus, and Jing Kong. Large area, few-layer graphene films on arbitrary substrates by chemical vapor deposition. *Nano letters*, 9(1):30–35, 2008.

[74] Qingkai Yu, Jie Lian, Sujitra Siriponglert, Hao Li, Yong P Chen, and Shin-Shem Pei. Graphene segregated on ni surfaces and transferred to insulators. *Applied Physics Letters*, 93(11):113103–113103, 2008.

[75] Keun Soo Kim, Yue Zhao, Houk Jang, Sang Yoon Lee, Jong Min Kim, Kwang S Kim, Jong-Hyun Ahn, Philip Kim, Jae-Young Choi, and Byung Hee Hong. Large-scale pattern growth of graphene films for stretchable transparent electrodes. *Nature*, 457(7230):706–710, 2009.

[76] Xuesong Li, Carl W Magnuson, Archana Venugopal, Jinho An, Ji Won Suk, Boyang Han, Mark Borysiak, Weiwei Cai, Aruna Velamakanni, Yanwu Zhu, et al. Graphene films with large domain size by a two-step chemical vapor deposition process. *arXiv preprint arXiv:1010.4731*, 2010.

[77] Youngbin Lee, Sukang Bae, Houk Jang, Sukjae Jang, Shou-En Zhu, Sung Hyun Sim, Young Il Song, Byung Hee Hong, and Jong-Hyun Ahn. Wafer-scale synthesis and transfer of graphene films. *Nano letters*, 10(2):490–493, 2010.

[78] Sukang Bae, Hyeongkeun Kim, Youngbin Lee, Xiangfan Xu, Jae-Sung Park, Yi Zheng, Jayakumar Balakrishnan, Tian Lei, Hye Ri Kim, Young Il Song, et al. Roll-to-roll production of 30-inch graphene films for transparent electrodes. *Nature nanotechnology*, 5(8):574–578, 2010.

[79] Ivan Vlassiouk, Murari Regmi, Pasquale Fulvio, Sheng Dai, Panos Datskos, Gyula Eres, and Sergei Smirnov. Role of hydrogen in chemical vapor deposition growth of large single-crystal graphene. *ACS nano*, 5(7):6069–6076, 2011.

[80] Nicolas Reckinger, Alexandre Felten, Cristiane N Santos, Benoît Hackens, and Jean-François Colomer. The influence of residual oxidizing impurities on the synthesis of graphene by atmospheric pressure chemical vapor deposition. *Carbon*, 2013.

[81] Ye Xiao, HoKwon Kim, Cecilia Mattevi, Manish Chhowalla, Robert C Maher, and Lesley F Cohen. Influence of cu substrate topography on the growth morphology of chemical vapour deposited graphene. *Carbon*, 2013.

[82] Gyula Eres, Murari Regmi, Christopher M Rouleau, Jihua Chen, Ilia N Ivanov, Alexander A Puretzky, and David B Geohegan. Cooperative island growth of large-area single-crystal graphene on copper using chemical vapor deposition. *ACS nano*, 8(6):5657–5669, 2014.

[83] Jannik C Meyer, AK Geim, MI Katsnelson, KS Novoselov, TJ Booth, and S Roth. The structure of suspended graphene sheets. *Nature*, 446(7131):60–63, 2007.

[84] A Fasolino, JH Los, and MI Katsnelson. Intrinsic ripples in graphene. *Nature Materials*, 6(11):858–861, 2007.

[85] Zhengtang Luo, Ye Lu, Daniel W Singer, Matthew E Berck, Luke A Somers, Brett R Goldsmith, and AT Charlie Johnson. Effect of substrate roughness and feedstock concentration on growth of wafer-scale graphene at atmospheric pressure. *Chemistry of Materials*, 23(6):1441–1447, 2011.

[86] Gang Hee Han, Fethullah Gunes, Jung Jun Bae, Eun Sung Kim, Seung Jin Chae, Hyeon-Jin Shin, Jae-Young Choi, Didier Pribat, and Young Hee Lee. Influence of copper morphology in forming nucleation seeds for graphene growth. *Nano letters*, 11(10):4144–4148, 2011.

[87] Xuesong Li, Yanwu Zhu, Weiwei Cai, Mark Borysiak, Boyang Han, David Chen, Richard D Piner, Luigi Colombo, and Rodney S Ruoff. Transfer of large-area graphene films for high-performance transparent conductive electrodes. *Nano letters*, 9(12):4359–4363, 2009.

[88] Dae Woo Kim, Yun Ho Kim, Hyeon Su Jeong, and Hee-Tae Jung. Direct visualization of large-area graphene domains and boundaries by optical birefringency. *Nature Nanotechnology*, 2011.

[89] Hong Wang, Guanzhong Wang, Pengfei Bao, Shaolin Yang, Wei Zhu, Xing Xie, and Wen-Jun Zhang. Controllable synthesis of submillimeter single-crystal monolayer graphene domains on copper foils by suppressing nucleation. *Journal of the American Chemical Society*, 134(8):3627–3630, 2012.

[90] Joseph M Wofford, Shu Nie, Kevin F McCarty, Norman C Bartelt, and Oscar D Dubon. Graphene islands on cu foils: the interplay between shape, orientation, and defects. *Nano letters*, 10(12):4890–4896, 2010.

[91] Yufeng Hao, MS Bharathi, Lei Wang, Yuanyue Liu, Hua Chen, Shu Nie, Xiaohan Wang, Harry Chou, Cheng Tan, Babak Fallahazad, et al. The role of surface oxygen in the growth of large single-crystal graphene on copper. *Science*, 342(6159):720–723, 2013.

[92] Robert Michael Jacobberger and Michael Scott Arnold. Graphene growth dynamics on epitaxial copper thin films. *Chemistry of Materials*.

[93] Li Tao, Jongho Lee, Harry Chou, Milo Holt, Rodney S Ruoff, and Deji Akinwande. Synthesis of high quality monolayer graphene at reduced temperature on hydrogen-enriched evaporated copper (111) films. *ACS nano*, 6(3):2319–2325, 2012.

[94] Yimin A Wu, Ye Fan, Susannah Speller, Graham L Creeth, Jerzy T Sadowski, Kuang He, Alex W Robertson, Christopher S Allen, and Jamie H Warner. Large single crystals of graphene on melted copper using chemical vapor deposition. *ACS nano*, 6(6):5010–5017, 2012.

[95] Wenzhong Bao, Feng Miao, Zhen Chen, Hang Zhang, Wanyoung Jang, Chris Dames, and Chun Ning Lau. Controlled ripple texturing of suspended graphene and ultrathin graphite membranes. *Nature nanotechnology*, 4(9):562–566, 2009.

[96] G Nandamuri, S Roumimov, and R Solanki. Chemical vapor deposition of graphene films. *Nanotechnology*, 21(14):145604, 2010.

[97] Ivan Vlassiouk, Pasquale Fulvio, Harry Meyer, Nick Lavrik, Sheng Dai, Panos Datskos, and Sergei Smirnov. Large scale atmospheric pressure chemical vapor deposition of graphene. *Carbon*, 2013.

[98] AC Ferrari, JC Meyer, V Scardaci, C Casiraghi, Michele Lazzeri, Francesco Mauri, S Piscanec, Da Jiang, KS Novoselov, S Roth, et al. Raman spectrum of graphene and graphene layers. *Physical review letters*, 97(18):187401, 2006.

[99] AC Ferrari, JC Meyer, V Scardaci, C Casiraghi, Michele Lazzeri, Francesco Mauri, S Piscanec, Da Jiang, KS Novoselov, S Roth, et al. The raman fingerprint of graphene. *arXiv preprint cond-mat/0606284*, 2006.

[100] F Molitor, D Graf, C Stampfer, T Ihn, and K Ensslin. Raman imaging and electronic properties of graphene. In *Advances in Solid State Physics*, pages 171–176. Springer, 2008.

[101] Zheng Yan, Zhiwei Peng, and James M Tour. Chemical vapor deposition of graphene single crystals. *Accounts of chemical research*, 47(4):1327–1337, 2014.

[102] Tianru Wu, Guqiao Ding, Honglie Shen, Haomin Wang, Lei Sun, Da Jiang, Xiaoming Xie, and Mianheng Jiang. Triggering the continuous growth of graphene toward millimeter-sized grains. *Advanced Functional Materials*, 2012.

[103] Lin Gan and Zhengtang Luo. Turning off hydrogen to realize seeded growth of subcentimeter single-crystal graphene grains on copper. *ACS nano*, 7(10):9480–9488, 2013.

[104] Hailong Zhou, Woo Jong Yu, Lixin Liu, Rui Cheng, Yu Chen, Xiaoqing Huang, Yuan Liu, Yang Wang, Yu Huang, and Xiangfeng Duan. Chemical vapour deposition growth of large single crystals of monolayer and bilayer graphene. *Nature communications*, 4, 2013.

[105] Y.C. Lin, C.C. Lu, C.H. Yeh, C. Jin, K. Suenaga, and P.W. Chiu. Graphene annealing: how clean can it be? *Nano letters*, 12(1):414–419, 2011.

[106] R. W. Johnstone. *Self-Sacrificial Surface-Micromachining using Poly (methyl methacrylate*. PhD thesis, Simon Fraser University, 2008.

[107] AM Affoune, BLV Prasad, Hirohiko Sato, and Toshiaki Enoki. Electrophoretic deposition of nanosized diamond particles. *Langmuir*, 17(2):547–551, 2001.

[108] P Blake, EW Hill, AH Castro Neto, KS Novoselov, D Jiang, R Yang, TJ Booth, and AK Geim. Making graphene visible. *Applied Physics Letters*, 91:063124, 2007.

[109] S Scott Courts and Philip R Swinehart. Review of cernox(zirconium oxy-nitride) thin-film resistance temperature sensors. In *TEMPERATURE: Its Measurement and Control in Science and Industry; Volume VII; Eighth Temperature Symposium*, volume 684, pages 393–398. AIP Publishing, 2003.

[110] Marcus W Doherty, Neil B Manson, Paul Delaney, Fedor Jelezko, Jörg Wrachtrup, and Lloyd CL Hollenberg. The nitrogen-vacancy colour centre in diamond. *Physics Reports*, 528(1):1–45, 2013.

[111] J Scott Bunch, Arend M Van Der Zande, Scott S Verbridge, Ian W Frank, David M Tanenbaum, Jeevak M Parpia, Harold G Craighead, and Paul L McEuen. Electromechanical resonators from graphene sheets. *Science*, 315(5811):490–493, 2007.

[112] Changyao Chen, Sami Rosenblatt, Kirill I Bolotin, William Kalb, Philip Kim, Ioannis Kymissis, Horst L Stormer, Tony F Heinz, and James Hone. Performance of monolayer graphene nanomechanical resonators with electrical readout. *Nature nanotechnology*, 4(12):861–867, 2009.

[113] Arend M van der Zande, Robert A Barton, Jonathan S Alden, Carlos S Ruiz-Vargas, William S Whitney, Phi HQ Pham, Jiwoong Park, Jeevak M Parpia, Harold G Craighead, and Paul L McEuen. Large-scale arrays of single-layer graphene resonators. *Nano letters*, 10(12):4869–4873, 2010.

[114] R.A. Barton, B. Ilic, A.M. van der Zande, W.S. Whitney, P.L. McEuen, J.M. Parpia, and H.G. Craighead. High, size-dependent quality factor in an array of graphene mechanical resonators. *Nano letters*, 11(3):1232, 2011.

[115] A Eichler, Joel Moser, J Chaste, M Zdrojek, I Wilson-Rae, and Adrian Bachtold. Nonlinear damping in mechanical resonators made from carbon nanotubes and graphene. *Nature nanotechnology*, 6(6):339–342, 2011.

[116] C. L. Degen. Scanning magnetic field microscope with a diamond single-spin sensor. *arxiv:cond-mat/0805.1215*, 2008.

[117] Steffen Steinert, Florian Dolde, Philipp Neumann, Andrew Aird, Boris Naydenov, Gopalakrishnan Balasubramanian, Fedor Jelezko, and Joerg Wrachtrup. High sensitivity magnetic imaging using an array of spins in diamond. *Review of scientific instruments*, 81(4):043705, 2010.

[118] Liam T Hall, Jared H Cole, Charles D Hill, and Lloyd CL Hollenberg. Sensing of fluctuating nanoscale magnetic fields using nitrogen-vacancy centers in diamond. *Physical review letters*, 103(22):220802, 2009.

[119] A Brillet, T Damour, and Ph Tourrenc. Introduction to gravitational wave research. In *Annales de Physique*, volume 10, pages 201–218. Les Editions de Physique, 1985.

[120] M. F. Bocko and R. Onofrio. On the measurement of a weak classical force coupled to a harmonic oscillator: experimental progress. *Rev. Mod. Phys.*, 68:755, 1996.

[121] Philippe Grangier, Juan Ariel Levenson, and Jean-Philippe Poizat. Quantum non-demolition measurements in optics. *Nature*, 396(6711):537–542, 1998.

[122] A. Gruber, A. Drabenstedt, C. Tietz, L. Fleury, J. Wrachtrup, and C. von Borczyskowski. Scanning confocal optical microscopy and magnetic resonance on single defect centers. *Science*, 276:2012, 1997.